

Master's thesis

2019

Anja Mærte

NTNU
Norwegian University of
Science and Technology
Faculty of Engineering
Department of Energy and Process Engineering

Master's thesis

Anja Mærte

PIV measurements in the vaneless space of a Francis turbine

June 2019



Norwegian University of
Science and Technology

PIV measurements in the vaneless space of a Francis turbine

Anja Mærle

Energy and Environmental Engineering

Submission date: June 2019

Supervisor: Pål-Tore Storli

Co-supervisor: Kristian Sagmo

Norwegian University of Science and Technology
Department of Energy and Process Engineering

MASTER THESIS

for

student Anja Mærleie

Spring 2019

PIV measurements in the vaneless space of a Francis turbine

PIV-målinger i omdreiningshulrommet på en Francisturbin

Background

Detailed measurements of the flow inside pumps and turbines are highly interesting for understanding the phenomena that occurs inside such machines. However, it is very difficult to obtain measurements that are highly resolved in time and space inside such machines. One place where optical access is possible is in the vaneless space in Francis turbines and Reversible Pump Turbines (RPTs). The Francis test rig at the Waterpower laboratory has recently been modified for Particle Image Velocimetry (PIV) measurements in the vaneless space. The overall intention is to measure the flow field in the vaneless space of both a Francis turbine runner and a RPT runner in both turbine and pump mode. Open measurements of this type are very rare in the research community and will be highly interesting on a global scale.

Objective

The candidate should prepare for and execute PIV measurements in the Francis test rig at the Waterpower laboratory of a Francis runner

The following tasks are to be considered:

1. Literature search on PIV measurement technique theory and the flow characteristics in the vaneless space of Francis turbines
2. Perform a measurement campaign for PIV measurements in the vaneless space of a Francis turbine, measuring on
 - Steady state; part load, best efficiency and full load operating points
 - If time allows; transients going from one operation point to another operating point
3. Document the measurements and the postprocessing of image data for determination of the velocity field, and compare with previous measurements

-- “ --

The master thesis comprises 30 ECTS credits.

The work shall be edited as a scientific report, including a table of contents, a summary in Norwegian, conclusion, an index of literature etc. When writing the report, the candidate must emphasise a clearly arranged and well-written text. To facilitate the reading of the report, it is important that references for corresponding text, tables and figures are clearly stated both places.

By the evaluation of the work the following will be greatly emphasised: The results should be thoroughly treated, presented in clearly arranged tables and/or graphics and discussed in detail.

The candidate is responsible for keeping contact with the subject teacher and teaching supervisors.

Risk assessment of the candidate's work shall be carried out according to the department's procedures. The risk assessment must be documented and included as part of the final report. Events related to the candidate's work adversely affecting the health, safety or security, must be documented and included as part of the final report. If the documentation on risk assessment represents a large number of pages, the full version is to be submitted electronically to the supervisor and an excerpt is included in the report.

According to “Utfyllende regler til studieforskriften for teknologistudiet/sivilingeniørstudiet ved NTNU” § 20, the Department of Energy and Process Engineering reserves all rights to use the results and data for lectures, research and future publications.

Submission deadline: 11 june 2019

- Work to be done in lab (Water power lab, Fluids engineering lab, Thermal engineering lab)
 Field work

Department for Energy and Process Engineering, 14/1 2019

Pål-Tore Storli
Supervisor

Co-Supervisor(s): Kristian Sagmo

Abstract

Two-dimensional particle image velocimetry measurements have been conducted in the vaneless space in the Francis turbine at the Waterpower Laboratory at the Norwegian University of Science and Technology. Measurements have been carried out at five different steady state operating points; two at part load, one at best efficiency point and two at high load. The present master thesis investigates the flow separation, wake, vortex shedding from the guide vane and rotor-stator interaction (RSI).

Time-averaged velocity fields have been computed from samples with a duration of 22 seconds, corresponding to 3600 runner blade passings. The exact positions of the separation points were not possible to determine from these velocity fields, but the width of the wake indicated a boundary layer separation upstream of the trailing edge tip at the suction side. The velocity deficit downstream of the guide vane decreased with an increasing distance from the trailing edge, and the wake path was dependent on the guide vane opening. The wake had a larger velocity deficit at the runner inlet at higher guide vane angles due to the shorter distance between the guide vane trailing edge and the runner interaction point.

Frequency analysis was performed on samples that lasted for 1.8 seconds, with a sample rate of 4166 Hz. To capture the RSI and vortex shedding frequency, power spectra were computed from the vertical velocity component at points near the runner inlet and in the wake. The dominant frequency at a point near the runner inlet was equal to the runner blade passing frequency. Irregular vortices of opposite rotation appeared behind the trailing edge of the guide vane as a result of boundary layer separation at the pressure and suction side. The vortex shedding frequency increased with a decreasing guide vane opening and was in the range of 1803-1977 Hz. By using the absolute velocity behind the guide vane as the free stream velocity in the empirical formula of Brekke, the estimated vortex shedding frequencies from the empirical formula were in strong agreement with the measured vortex shedding frequencies.

Keywords: Francis turbine, vaneless space, particle image velocimetry, rotor-stator interaction, vortex shedding

Sammendrag

Todimensjonale particle image velocimetry målinger er blitt utført i omdreiningshulrommet inne i francisturbinen på Vannkraftlaboratoriet på Norges teknisk-naturvitenskapelige universitet. Målingene er utført ved fem stasjonære driftspunkter; henholdsvis to på lav last, ett i bestpunkt og to på høy last. Denne masteroppgaven undersøker strømningsseparasjonen, vaken, virvelavløsninger fra bakkanten av ledeskovlene og interaksjonen mellom rotor- og statorside (RSI).

Gjennomsnittlige hastighetsfelt ble beregnet fra 22 sekunders lange opptak, som tilsvarer 3600 turbinbladpasseringer. Den nøyaktige posisjonen til strømningsseparasjonen var ikke mulig å bestemme ut fra hastighetsfeltene, men bredden til vaken indikerte at separasjonen av grensesjiktet oppstod oppstrøms for bakkanten av ledeskovlen på sugesiden. Hastighetstapet var størst rett bak ledeskovlen og ble redusert etter hvert som væsken beveget seg vekk fra ledeskovlen. Vakens retning endret seg etter ledeskovlens vinkling. Vaken hadde et større hastighetstap ved rotorinngangen for høyere ledeskovlvinkler siden interaksjonspunktet i rotorinngangen og bakkanten av ledeskovlen var nærmere hverandre for disse vinklene.

Frekvensanalyse av samplinger med en varighet på 1,8 sekunder og en samplingsrate på 4166 Hz ble utført. Effektspektre fra vertikale hastighetskomponenter i punkter nær rotorinngangen og i vaken ble beregnet for å fange opp RSI- og virvelavløsningsfrekvensen. Den dominerende frekvensen i punktet nært rotoren sammenfalte med bladpasseringsfrekvensen på 166,5 Hz. På grunn av grensesjiktseparasjonen ved trykk- og sugeside av skovlen oppstod uregelmessige virvler med ulik rotasjon. Virvelavløsningsfrekvensen var mellom 1803 og 1977 Hz, og jo lavere ledeskovlvinkel, desto høyere var frekvensen. Ved å benytte den absolutte hastigheten bak ledeskovlen som fristrømhastigheten i den empiriske formelen til Brekke, stemte de estimerte virvelavløsningsfrekvensene godt overens med de målte frekvensene.

Nøkkelord: francisturbin, omdreiningshulrom, particle image velocimetry, rotor-stator interaksjon, virvelavløsning

Acknowledgement

The work presented in this master thesis has been performed at the Waterpower Laboratory, Department of Energy and Process Engineering at the Norwegian University of Science and Technology.

During the work with this master thesis, a number of people have contributed with advice and support. I would first like to thank my supervisor Pål-Tore Storli for making this study possible, and for his invaluable guidance throughout the last year. It has been intriguing to work with such state-of-the-art, high-end equipment. Special thanks to Magne Tveit Bolstad for teaching me the PIV equipment and for always devoting his time for discussions and my questions. I also wish to give a big thanks to my co-supervisor Kristian Sagmo. His knowledge and experience regarding PIV were extremely useful for this master thesis. Johannes Kverno, Einar Agnalt and Trygve Opland are greatly appreciated for their assistance in the laboratory.

The last year I have been privileged to work at the Waterpower Laboratory in a warm and fun environment. Many thanks to all my student colleagues and academic staff at the Waterpower Laboratory for making this year great.



Anja Mærle

Trondheim, 06 2019

Contents

Abstract	i
Sammendrag	iii
Acknowledgement	v
List of Figures	vii
List of Tables	x
Abbreviations	xi
Nomenclature	xii
1 Introduction	1
1.1 Background	1
1.2 Objective	2
1.3 Previous work	3
2 Theory	5
2.1 Francis turbine	5
2.2 Flow characteristics in the vaneless space	8
2.2.1 Reynolds number and boundary layer	8
2.2.2 Separation and wake flow around a foil	9
2.2.3 Vortex shedding	13
2.2.4 Vortex shedding frequency	15
2.2.5 Lock-in	18
2.2.6 Rotor-stator interactions	19
2.3 Particle image velocimetry	22
2.3.1 Seeding	23
2.3.2 Light source and camera	25
2.3.3 Calibration	27
2.3.4 Interrogation area	28
2.3.5 Evaluation	29
2.3.6 Post-processing	32
2.3.7 Power spectrum	34
2.3.8 Quantifying uncertainty of PIV measurements	35
3 Methodology	38
3.1 Test rig	38
3.2 Turbine operating parameters	40
3.3 PIV equipment	42

3.4	Experimental PIV set-up	43
3.5	PIV calibration	45
3.6	PIV recording parameters	48
3.7	PIV measurement uncertainty	53
4	Results and discussion	55
4.1	Time-averaged velocity fields	55
4.2	Time-averaged velocity profiles	58
4.3	RSI	60
4.4	Vortex shedding	62
5	Conclusion	66
6	Further work	67
Appendices		
A Coordinate systems		
B Laser subsystem, laser overlap test and PTU synchronization test		
C Sensor uncertainty		
D Power spectra for different operating points		
E Risk Assessment Report and Attachment to Risk Assessment Report		

List of Figures

1.1	Velocity distribution in guide vane cascade and vaneless space. Reproduced from [10].	4
2.1	Francis turbine components. Reproduced and modified from [12].	6
2.2	Volute, stay and guide vanes and runner blades of a Francis turbine. Reproduced from [12].	6
2.3	Hill diagram for Francis runner at NTNU. Reproduced from [16].	7
2.4	Boundary layer development over a flat plate at zero incidence.	9
2.5	Common terms related to foils.	9
2.6	Boundary layer separation due to adverse pressure gradients.	10
2.7	Wake behind a body. Reproduced from [19].	11
2.8	Separation points, wake flow and velocity profiles downstream of a body. Reproduced from [21].	11
2.9	Separation point and wake for different angles of attack. Reproduced and modified from a PowerPoint presentation [22].	12
2.10	Flow around a cylinder for different Reynolds numbers. Reproduced from [24].	13
2.11	Visualization of the von Kármán vortex street behind a circular cylinder in air flow. Reproduced from [27].	14
2.12	Strouhal number as a function of Reynolds number for a circular cylinder. Reproduced from [29]	15
2.13	Geometry constants for different trailing edges. Reproduced from [33].	17
2.14	Vortex shedding frequency and natural frequency for increasing flow velocity.	18
2.15	Different rotor-stator interactions. Reproduced from [42].	19
2.16	The effects of runner blades and guide vanes on the flow field. Reproduced from [44].	20
2.17	The viscous wake interaction point with the runner for different guide vane angles. Reproduced from [45].	20
2.18	Experimental arrangement for PIV. Reproduced from [48, p. 8].	22
2.19	Light scattered by a 10 μm glass particle in water according to Mie theory. Reproduced from [48, p. 33-51].	23
2.20	Three modes of tracer particle image density: a low (PTV), b medium (PIV), and c high image density (LSV). Reproduced from [48, p. 8-15].	24
2.21	An example of aliasing as a result of under-sampling.	26
2.22	Time delay between pulses and image rate.	26
2.23	Timing diagram for dual-frame image capture with a sCMOS image sensor showing synchronization with double cavity pulsed Nd:YAG laser. Reproduced from [48, p. 120-122].	27
2.24	FOV divided into IAs. Reproduced from [58].	28
2.25	PIV images with varying seeding densities and the corresponding correlation functions. Reproduced from [48, p. 203-229].	29

2.26	Two consecutive samples and their cross-correlation plane. Reproduced from [48, p. 145-171].	30
2.27	Analysis of double frame recordings using the digital cross-correlation method. Reproduced from [48, p. 145-171].	31
2.28	PIV images with varying background noise level and the corresponding correlation functions. Reproduced from [48, p. 203-229].	31
2.29	An area with a large number of incorrect velocity vectors. Reproduced from [48, pp. 243-256].	32
2.30	Sketch of data grid points with vector notations.	33
2.31	Input function (red) approximated by six sinusoidal functions (blue). Single shot of an animation by LucasVB [63].	34
2.32	Resulting peaks in the frequency domain of the function. Single shot of an animation by LucasVB [63].	34
2.33	The concept of accuracy and precision illustrated. A modified version from [48, p. 203-229].	35
2.34	Histograms of the estimated displacement. Left: a particle image diameter of 1 pixel illustrating peak locking. Right: a particle image diameter of 3 pixels. Reproduced from [48, p. 203-229].	36
3.1	Closed loop configuration with arrows indicating fluid trajectory. Reproduced from [8].	38
3.2	Test section with arrows indicating flow inlet and outlet.	39
3.3	Geometry of guide vanes in model turbine. Reproduced and modified from [21].	39
3.4	Test section with main PIV components. Reproduced and modified from [8].	43
3.5	Integrated plexiglass windows.	43
3.6	Close-up of measurement set-up. Reproduced and modified from [8].	44
3.7	Calibration target.	45
3.8	Laser boxes mounted on the camera and laser sheet optics. Reproduced and modified from [8].	46
3.9	Coordinate system shown on the calibration target. The solid and dashed rectangles are the two different FOV sizes of 1280 x 1024 pixels and 1280 x 600 pixels, respectively.	46
3.10	Calibration target with a 1280 x 1024 pixels resolution FOV.	47
3.11	The 1280 x 1024 pixels FOV and 1280 x 600 pixels FOV in the measurement plane with the 50 mm objective.	49
3.12	Images before and after applied time filter.	50
3.13	Illustration of two consecutive frames and final IAs of size 24 x 24 pixels.	50
3.14	Average velocity field at BEP for final IA of size, a: 48 x 48 pixels, b: 32 x 32 pixels, c: 24 x 24 pixels, d: 16 x 16 pixels.	51
3.15	Histogram representation of the probability density function of an instantaneous velocity field.	53

3.16	Cross correlation uncertainty of the absolute velocity for an instantaneous velocity field.	54
4.1	Time-averaged absolute velocity fields.	56
4.2	Uncertainty of the time-averaged absolute velocity field at BEP.	57
4.3	x-positions of velocity profiles indicated by dashed black lines.	58
4.4	Velocity profiles along four lines in the wake for a ramp up measurement at BEP.	58
4.5	Velocity profiles along two lines in the wake for two ramp up measurements at BEP.	59
4.6	Pos. 1 indicated in the 1280 x 600 FOV.	60
4.7	Power spectrum obtained for cross flow velocity component at Pos. 1 at BEP.	60
4.8	Instantaneous vector field coloured according to vorticity at BEP.	62
4.9	Power spectrum obtained from cross flow velocity component at position (15, 0) at BEP.	63
A.1	An overview of the local coordinate system of the FOV and the global coordinate system of the turbine.	
D.1	Power spectrum obtained from cross flow velocity component at position (15, 3) for a guide vane opening of 6.7 degrees.	
D.2	Power spectrum obtained from cross flow velocity component at position (15, -2) for a guide vane opening of 12.4 degrees.	
D.3	Power spectrum obtained from cross flow velocity component at position (15, -4) for a guide vane opening of 14 degrees.	

List of Tables

3.1	Operating points.	40
3.2	Arithmetic mean and relative standard deviation of operating parameters.	41
3.3	PIV components.	42
3.4	PIV recording parameters.	48
4.1	FOV average absolute velocity for each operating point.	57
4.2	Mean vortex shedding frequency for different operating points.	64
4.3	Estimated vortex shedding frequency.	64
A.1	Local coordinates that bound the 1280 x 1024 FOV converted into to global coordinates.	
C.1	Combined relative uncertainties at different operating points.	

Abbreviations

Symbol	Description
BEP	Best Efficiency Point
FFT	Fast Fourier Transform
FL	Full Load
FOV	Field of View
HL	High Load
IA	Interrogation Area
LSV	Laser Speckle Velocimetry
LTS	Laser Timing Stabilizer
NTNU	Norwegian University of Science and Technology
PIV	Particle Image Velocimetry
PL	Part Load
PTU	Programmable Timing Unit
PTV	Particle Tracking Velocimetry
RSI	Rotor-Stator Interaction
TE	Trailing edge

Nomenclature

Symbol	Description	Unit
B	Trailing edge geometry constant	[-]
c	Chord length	[m]
D_o	Runner outlet diameter	[m]
f	Specified factor	[-]
f_{gv}	Guide vane passing frequency	[Hz]
f_n	Natural frequency	[Hz]
f_{rb}	Runner blade passing frequency	[Hz]
f_s	Vortex shedding frequency	[Hz]
g	Gravitational constant	[m/s ²]
H	Net head	[m]
I	First sample frame	[-]
I'	Second sample frame	[-]
L	Characteristic length	[m]
N	Number of samples	[-]
N_{eff}	Effective number of samples	[-]
n	Runner rotational speed	[rpm]
n_{ED}	Speed factor	[-]
P	Pressure	[Pa]
Q	Discharge	[m ³ /s]
Q_{ED}	Discharge factor	[-]
R_{II}	Cross-correlation function	[-]
Re	Reynolds number	[-]
Re_c	Chord based Reynolds number	[-]
s	Experimental standard deviation	[]
St	Strouhal's number	[-]
t	Trailing edge thickness	[mm]
Δt	Time delay between pulses	[s]
u	Characteristic velocity	[m/s]
U_{ds}	Absolute velocity downstream of guide vane	[m/s]
U	x-component of velocity	[m/s]
V	y-component of velocity	[m/s]
$ V $	Absolute velocity	[m/s]
$\Delta V $	Uncertainty of time-averaged absolute velocity	[m]
v_x	x-component of velocity	[m/s]
v_y	y-component of velocity	[m/s]
Z_{gv}	Number of guide vanes	[-]
Z_{rb}	Number of runner blades	[-]

Greek letters

Symbol	Description	Unit
α	Angle of attack	[°]
α_{GV}	Guide vane angle	[°]
δ	Boundary layer thickness	[m]
δ_v	Virtual boundary layer thickness	[m]
μ	Dynamic viscosity	[kg/ms]
ν	Kinematic viscosity	[m ² /s]
ρ	Density of fluid	[kg/m ³]
ρ_p	Density of tracer particle	[kg/m ³]
$\sigma_{ V }$	Standard deviation of $ V $	[m/s]
ω	Vorticity	[1/s]

1 Introduction

This section starts off by presenting the background of the master thesis, followed by a description of the main objective. Finally, some previous experimental measurements and numerical simulations in the vaneless space are presented.

1.1 Background

Climate change is one of the greatest challenges of the 21st century, and the general consensus is that human activity is the main driver of change. EU's goal of a climate neutral economy by 2050 necessitates a significantly increased deployment of renewables into the energy system [1]. Renewable energy sources have large potential to mitigate climate change by replacing fossil fuels. Over the past years, renewable and intermittent energy sources such as solar and wind power, have become increasingly widespread [2].

The increased penetration of intermittent energy sources into the grid network has raised concern for grid stability [3, 4]. Hydropower benefits the power system as it offers energy storage, and enables power to quickly be produced at times when the generation of electricity is lower than the demand. Unlike solar and wind power, hydropower is not strictly dependent on the weather conditions, and is the most flexible power technology with among the best conversion efficiencies of all energy sources [5].

The Francis turbine is the most common hydraulic turbine in use today [6, 7]. To maintain the stability of the grid, the hydraulic turbines are required to operate at off-design conditions more frequently. Consequently, the hydraulic turbines have to be able to operate properly over a wider range of operating conditions than they traditionally have been designed for [3]. This causes the need for a thorough understanding of the fluid flow inside a Francis turbine at different operating conditions.

It is hypothesized that several of the undesirable phenomena in the Francis turbines are related to the flow characteristics in the vaneless space. The vaneless space is located between the outlet of the guide vanes and the inlet of the runner blades. The Francis test rig at the Waterpower Laboratory at NTNU has been modified to allow for particle image velocimetry (PIV) measurements in the vaneless space. PIV is a measurement technique that enables capturing the detailed flow field, and makes it possible to investigate the flow phenomena occurring in this region at different operating conditions. The Francis turbine, on which the measurements have been carried out, has a geometry that is open to the public. As a result, the measurements can serve as a comparison basis for flow simulations of the same Francis turbine.

1.2 Objective

The ultimate objective of this work is to obtain an increased understanding of the flow characteristics in the vaneless space in a Francis turbine. To achieve this, PIV measurements have been planned, conducted and documented for five different operating points in steady operation; at part load, best efficiency point, and high load. The results obtained from the PIV measurements are discussed with emphasis on the flow separation, wake, RSI and vortex shedding occurring in the vaneless space.

As the flow in the vaneless space is affected by flow separation, wakes, vortex shedding and RSI, a literature study on these flow phenomena has been carried out. Several aspects have to be taken into account when planning and performing a PIV measurement. An extensive literature study regarding this measurement technique has been conducted.

Due to time constraints and limited access to the laboratory, transient measurements have not been performed. Recordings with both 50 mm and 100 mm objective lenses were executed. Due to time limitations, only the measurements with the 100 mm objective lens were processed and will be presented in this thesis.

A project thesis has been written by the author prior to this master thesis, and the following parts in the theory are partly reused and modified versions from the project thesis: 2.2.3, 2.2.5, 2.2.6, 2.3.1, 2.3.5.

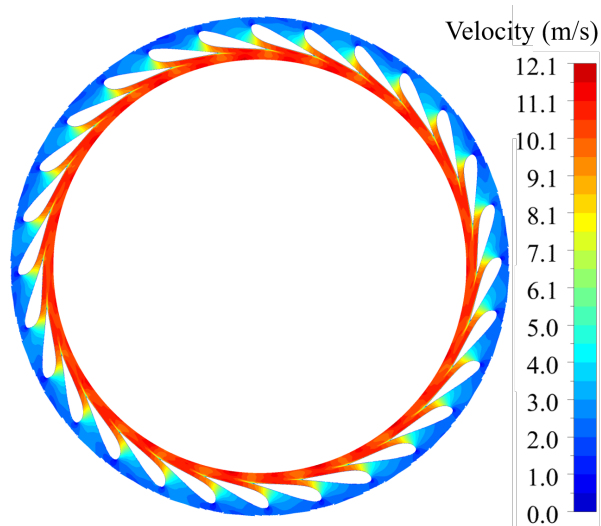
1.3 Previous work

Similar measurements to those conducted in this thesis, have previously been carried out in the same Francis turbine and are described in the following subsection. Numerical simulations have also been performed for the Francis turbine at the Waterpower Laboratory at NTNU, and will be presented as well.

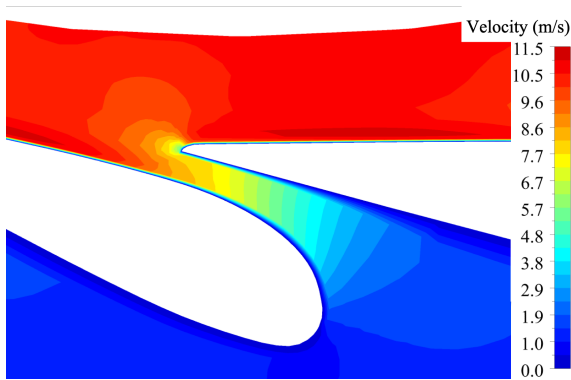
PIV measurements in the vaneless space of a Francis turbine have previously been performed at the Waterpower Laboratory at NTNU by Straume [8]. The measurements were conducted at best efficiency point (BEP) corresponding to a guide vane opening of 10 degrees. Straume investigated the velocity field, RSI frequency and vortex shedding frequency. Velocity profiles at different x-positions indicated that the wake behind the guide vanes gradually weakened with an increasing distance from the trailing edge. Power spectra were computed for the vertical velocity component at several points located near the runner inlet and in the wake. The RSI frequency was dominating near the runner inlet, and decayed with distance from the runner inlet. The power spectrum computed from a point near the runner inlet showed a dominant peak coinciding with the blade passing frequency of 166.6 Hz, and a second peak matching the second harmonic frequency of about 333 Hz. The vortex shedding frequency was investigated for different points located in the wake, and it was found to be in range of 1800 - 2000 Hz. As several peaks were present in the power spectra, a definite vortex shedding frequency was not determined. Brekke's formula yielded in a vortex shedding frequency range of 1044 - 1656 Hz, and hence underpredicted the vortex shedding frequency.

In an in-house measurement report of Sagmo [9], PIV measurements in the vaneless space of a Francis turbine at BEP have been documented and discussed. A vortex shedding frequency of 1850 Hz was estimated from a power spectra computed of the cross stream velocity component from a point in the wake. The resulting power spectra showed several frequency peaks, and the shedding frequency was determined from the mean of the dominant peaks in each measurement series. The Strouhal relation underpredicted the shedding frequency.

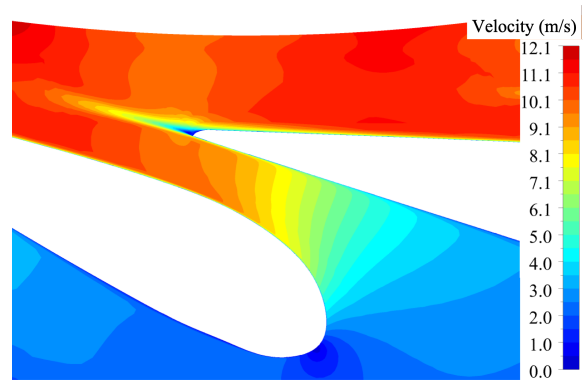
Trivedi et al. [10] have carried out numerical simulations of the Francis turbine at the Waterpower Laboratory. Four different operating conditions have been studied; two at part load, at BEP and at high load. The resulting velocity distribution in the guide vane cascade and in the vaneless space is shown in Fig. 1.1. Fig. 1.1a shows that the flow accelerates through the guide vane passages. From Fig. 1.1b-1.1e, the flow velocity around the guide vane trailing edge is observed to generally increase with lower guide vane openings. The separation of the boundary layer occurs slightly upstream of the tip on the suction side of the guide vane. For a guide vane opening of 6.7° , the separation occurs more upstream than for the other openings.



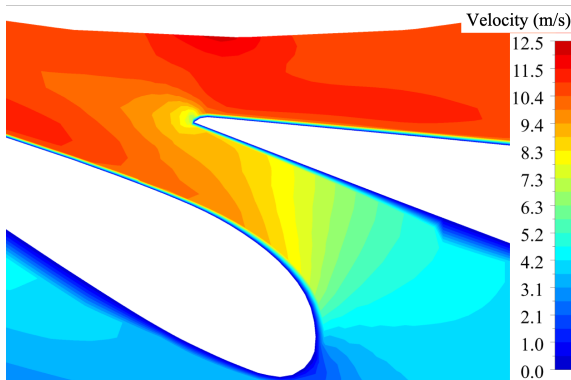
(a) Guide vane angle of 6.7° , full view.



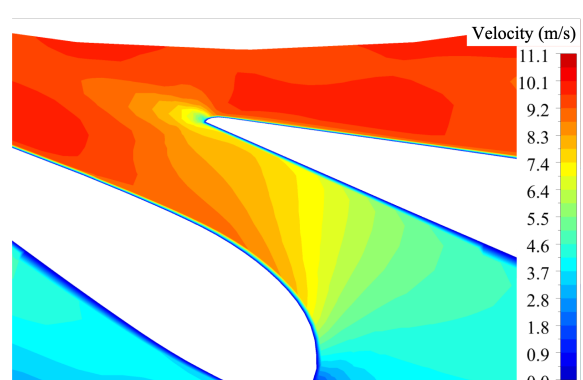
(b) Guide vane angle of 4° .



(c) Guide vane angle of 6.7° .



(d) Guide vane angle of 10° .



(e) Guide vane angle of 12.4° .

Figure 1.1: Velocity distribution in guide vane cascade and vaneless space. Reproduced from [10].

2 Theory

The theory section is divided into three parts, the first about the Francis turbine, the second about the flow characteristics in the vaneless space and the third about the PIV measurement technique. In the first part, basic theory regarding the Francis turbine and its components will be presented. Furthermore, the location of the vaneless space and different operational conditions are defined. As the flow in the vaneless space is affected by flow separation, wake, vortex shedding and the interaction between static and rotating parts of the turbine, the second theory part contains a literature study on these flow phenomena. In the third part each subsystem in a PIV measurement will be described thoroughly. As it is a relatively complicated measurement technique, an extensive literature study has been carried out for this topic.

The following sub-subsections are partly reproduced and modified from the author's project thesis: 2.2.3, 2.2.5, 2.2.6, 2.3.1, 2.3.5

2.1 Francis turbine

In hydropower plants the most commonly used type of turbine is the Francis turbine, responsible for approximately 60% of the generated hydropower worldwide [7]. In the following subsection important definitions regarding hydropower plants and Francis turbines will be introduced.

In hydropower plants there are typically two reservoirs located at two different vertical altitudes. The gross head or hydraulic head is equivalent to the height difference between the lower and higher water level. The effective head or net head takes the losses caused by pipe friction into account [11]. Accordingly its value will be reduced compared to the hydraulic head. From here on the net head will be referred to as only head and denoted by H .

With the help of a dam, the water is accumulated in the reservoir at high elevation. Via a penstock, the water flows from the reservoir to a spiral casing that surrounds the runner, called a volute. An illustration of a Francis turbine with its components is shown in Fig. 2.1. The spiral casing has a decreasing cross-sectional area along the flow path [13]. The purpose of this design is to obtain a uniform velocity distribution in the circumferential direction at the outlet of the volute [14]. Before the flow enters the runner, it first passes a set of fixed vanes called stay vanes, and then passes adjustable vanes called guide vanes. The main function of the stay vanes is to support the pressure loads in the volute and turbine head cover [14]. Their second purpose is to steer the flow with an optimal incidence angle towards the guide vanes. To control the discharge through the runner, the guide vane angles can be adjusted [15, p. 837-838]. A change of the guide vane angle, also referred to as guide vane opening, is equivalent to a change of the load on the turbine.

The vaneless space in a Francis turbine refers to the gap between the outlet of the guide vanes and the inlet of the runner blades. In Fig. 2.2, R1 illustrates the location of the vaneless space.

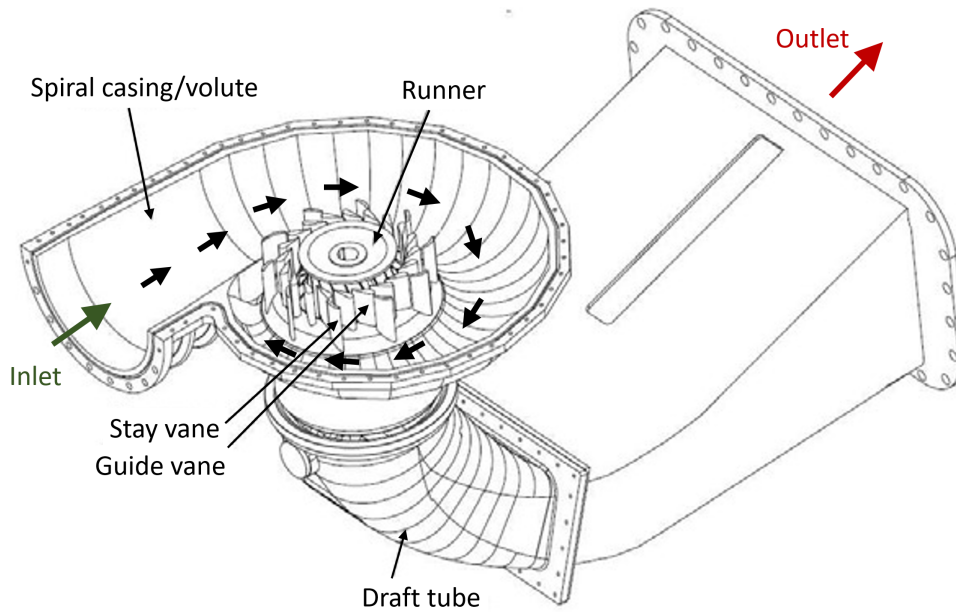


Figure 2.1: Francis turbine components. Reproduced and modified from [12].

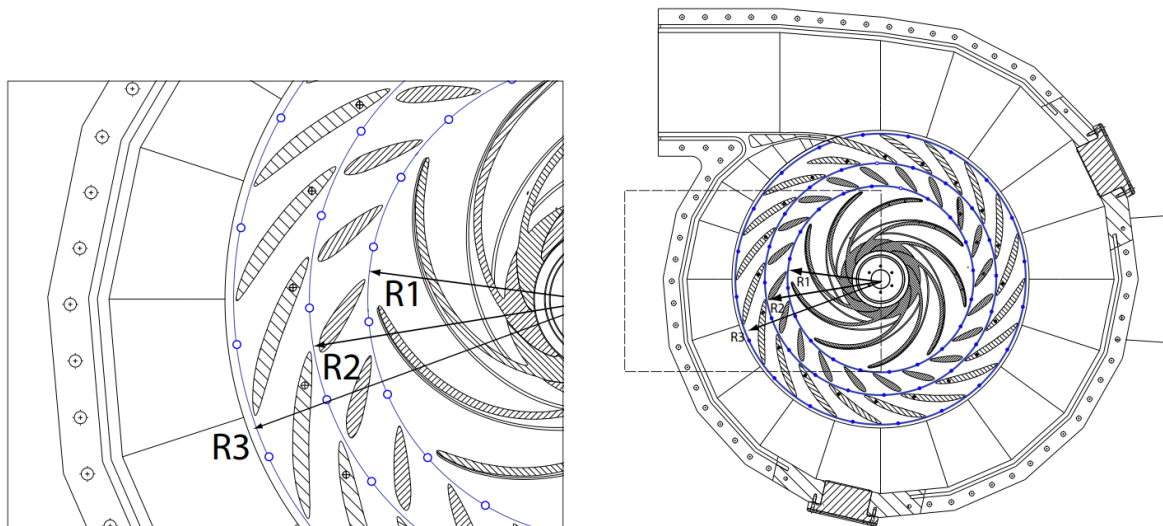


Figure 2.2: Volute, stay and guide vanes and runner blades of a Francis turbine. Reproduced from [12].

The vaneless space narrows with an increasing guide vane angle. The runner is located downstream of the vaneless space, and is fitted with a set of runner blades. As water flows through the runner and makes it rotate clockwise, momentum of the flow is exchanged between the fluid and the runner and the pressure drops significantly [15, p. 837-838]. At design condition, flow enters the runner radially, and leaves axially. The draft tube is located at the exit side of the runner [13].

A Hill diagram, also commonly referred to as a characteristic diagram, provides an overview of the efficiency at different operating points for a turbine. All Francis turbines have their unique

characteristic diagram. The efficiency is a function of the runner rotational speed, discharge and guide vane angle denoted by n , Q and α_{GV} , respectively. The best efficiency point is at which the efficiency of the turbine is at its optimum. The operating points with smaller guide vane openings that for one at BEP, is referred to as part load (PL), while high load (HL) and full load (FL) correspond to larger guide vane openings than for one at BEP.

In Fig. 2.3, a hill chart for the Francis runner at the Waterpower Laboratory at NTNU is shown [16]. The runaway curve or no-load curve, for which the torque is equal to zero, is presented in the figure. Based on the efficiency curves, it can be observed that the guide vane angle at BEP is approximately 10° .

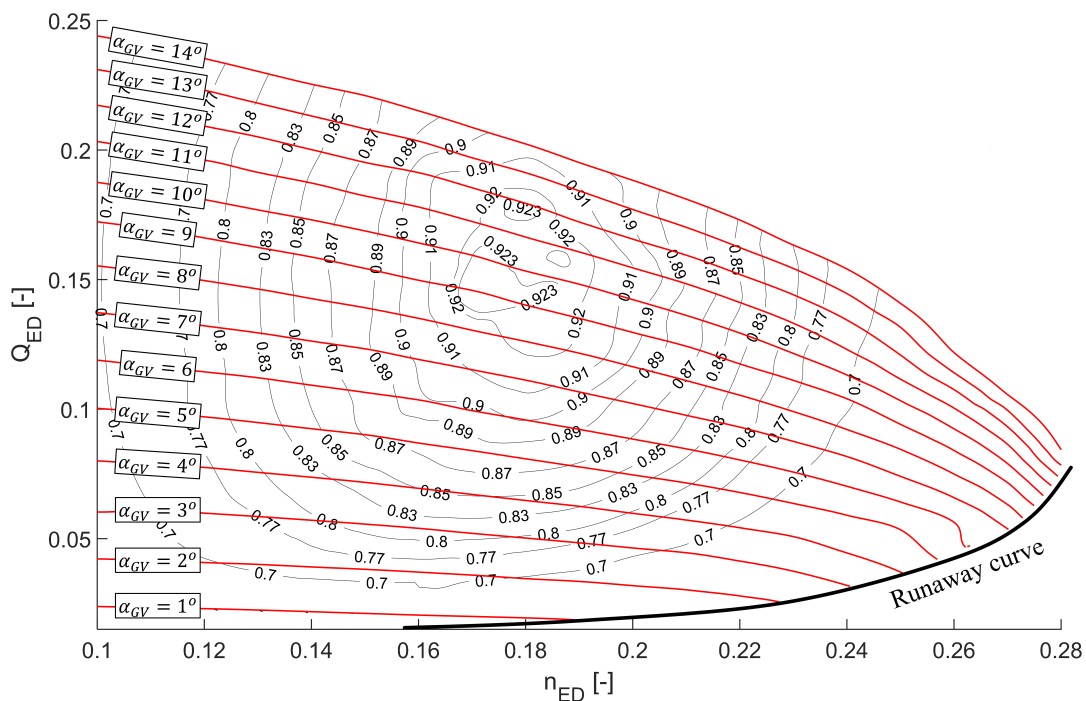


Figure 2.3: Hill diagram for Francis runner at NTNU. Reproduced from [16].

In the figure above, the rotational speed and discharge are converted into dimensionless parameters. In the Hill diagram for the Francis runner at the Waterpower laboratory, the dimensionless parameters are calculated as shown below. The dimensionless speed factor, n_{ED} , is calculated:

$$n_{ED} = \frac{nD_o}{\sqrt{gH}} \quad (2.1)$$

where D_o is the runner outlet diameter, g is the gravitational constant and H denotes the head. The dimensionless discharge factor, Q_{ED} can be computed as follows:

$$Q_{ED} = \frac{Q}{D_o^2 \sqrt{gH}} \quad (2.2)$$

2.2 Flow characteristics in the vaneless space

Flow characteristics in the vaneless space will be highly affected by the flow phenomena occurring around the guide vanes. The guide vanes are shaped as hydrofoils, hence general foil theory can be applied to guide vanes. The following subsection covers the commonly used terms, definitions, and concepts concerning flow around foils, as well as the rotor-stator interaction.

2.2.1 Reynolds number and boundary layer

The following sub-subsection explains the concepts of laminar and turbulent flows, and boundary layers. This will serve as a foundation for understanding the later presented flow phenomena. The Reynolds number is a dimensionless parameter that describes the ratio of inertial forces to viscous forces in Newtonian fluids. Water is considered to be a Newtonian fluid [15, p. 52]. The Reynolds number, Re , is defined in (2.3).

$$Re = \frac{\textit{inertial forces}}{\textit{viscous forces}} = \frac{\rho u L}{\mu} = \frac{u L}{\nu} \quad (2.3)$$

Where ρ denotes the density of the fluid, u is the characteristic velocity, L presents the characteristic length, μ is the dynamic viscosity of the fluid, and ν is the kinematic viscosity of the fluid. For foils, the chord length is typically used as the characteristic length [17].

Low Reynolds numbers correspond to laminar flows because viscous forces are dominant, while high Reynolds numbers correspond to turbulent flows and are dominated by inertial forces. Laminar flow is characterized by smooth layers of fluid with different velocity without substantial exchange of fluid particles perpendicular to the flow direction. Contrary, turbulent flow is characterized by irregular, random, fluctuating motion. The critical Reynolds number refers to the Reynolds number at which a laminar-turbulent transition occurs. The intermediate range between laminar and turbulent state is defined as the transitional range. For instance, the critical Reynolds number is found to be $5 \cdot 10^5$ for a flow over a flat plate at zero incidence [17].

Prandtl introduced the boundary layer theory, suggesting that all fluid flows moving past a solid surface can be divided up into two regions, an outer and an inner region. The outer flow region is considered inviscid, meaning that the viscosity can be neglected. In the inner region, the viscosity must be taken into account to satisfy the no-slip condition at the wall. This region is referred to as the boundary layer, and is the thin layer of viscous fluid in immediate vicinity of a solid surface [17].

All objects in contact with a moving stream will have boundary layers formed adjacent to the solid surface [17]. The boundary layer thickness, δ , is typically measured from the solid surface to the point at which the viscous flow velocity approaches the free stream velocity [15, p. 554-583]. Within the boundary layer the flow can be both laminar and turbulent. For flow over a flat plate at zero incidence, the flow within the boundary layer will undergo a laminar-turbulent

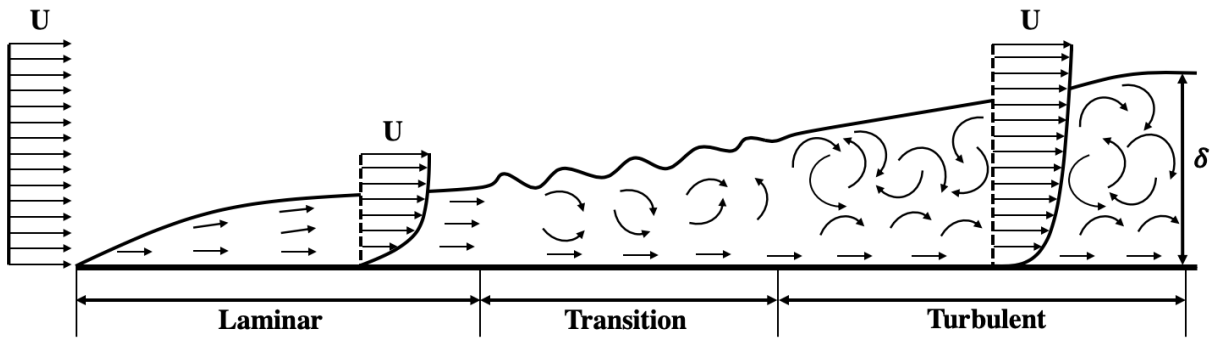


Figure 2.4: Boundary layer development over a flat plate at zero incidence.

transition [17], which is illustrated in Fig. 2.4. The increasing thickness of the boundary layer along the plate is also observable.

2.2.2 Separation and wake flow around a foil

In Fig. 2.5, some common foil terms are presented. As shown in this figure, the foil has a leading edge upstream and a trailing edge (TE) downstream. On one side, shown as the upper side in the figure, the static pressures are considerably lower than on the opposite side [18]. Hence the upper surface is referred to as the suction side, while the lower surface is referred to as the pressure side. α denotes the angle of incidence or angle of attack, and is the angle the incoming fluid stream makes with chord line [15, p. 610-643].

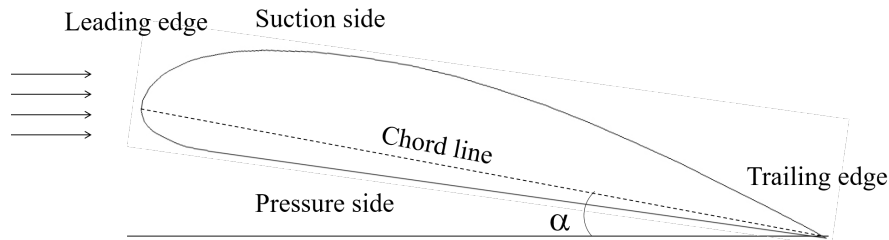


Figure 2.5: Common terms related to foils.

As with the flat plate, a laminar boundary layer starts to develop at the leading edge of a foil. In a similar fashion, a laminar-turbulent transition occurs after a certain distance along the contour of the foil. The position of this transition strongly depends on the pressure distribution imposed by the outer flow [17].

Along the curved surface of a foil there will be various pressure gradients, $\frac{\delta P}{\delta x}$, as shown in Fig. 2.6. Immediately downstream the leading edge of the foil, the inviscid outer flow accelerates, which indicates that the pressure is decreasing while the velocity increases. In this case, the boundary layer thickness is typically thin and hugs closely to the wall due to the accelerating flow. Therefore the boundary layer is not likely to separate from the wall, causing what is called

a favourable pressure gradient [15, p. 554-583].

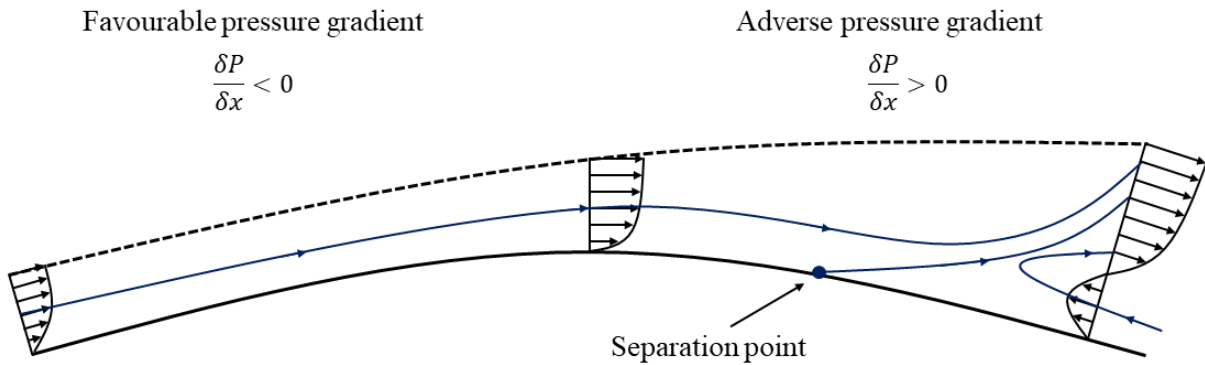


Figure 2.6: Boundary layer separation due to adverse pressure gradients.

As the flow moves closer to the trailing edge of the foil, the inviscid outer flow decelerates, meaning that the pressure is increasing and the velocity decreases. This leads to an adverse pressure gradient where the pressure is pushing in the opposite direction to the bulk fluid motion. The thickness of the boundary layer tends to increase, and the boundary layer does not hug as closely to the wall anymore. Given that the adverse pressure gradient is strong enough, it will eventually cause the flow to reverse close to the wall as shown in the figure. This phenomenon is called backflow. The separation point is located at which the velocity of the boundary layer relative to the body is close to zero. This happens when the boundary layer moves far enough against an adverse pressure gradient. As a result, the fluid flow detaches itself from the surface of the foil, and vortices begin to form from the backflow [15, p. 554-583].

Flow separation occurs when the fluid detaches itself from the surface of the body. The location of the separation point is dependent on several factors such as Reynolds number, the surface roughness and the level of fluctuations in the free stream. It is usually difficult to predict exactly where the separation will occur on the foil. The pressure is low downstream of the separation point, and recirculating flow and backflow occur [15, p. 610-643]. When the boundary layer has separated and left the body, so-called free shear layers are developed further downstream, and forms a viscous wake [17].

The wake is defined as the friction-dominated region of disturbed flow downstream of a body, where the effects of the body are felt on velocity. The viscous wake will create a velocity defect on the flow, affecting the velocity distribution [19]. Wakes are characterized by high shear with the lowest velocities in the centre of the wake and highest velocities at the edges. The wake extends downstream of the body until the fluid regains its velocity and the velocity profile is nearly uniform again [15, p. 610-643]. Fig. 2.7 shows a wake behind a foil and velocity profiles at different x-positions. Δu denotes the velocity deficit in the wake, and b is the width of the wake.

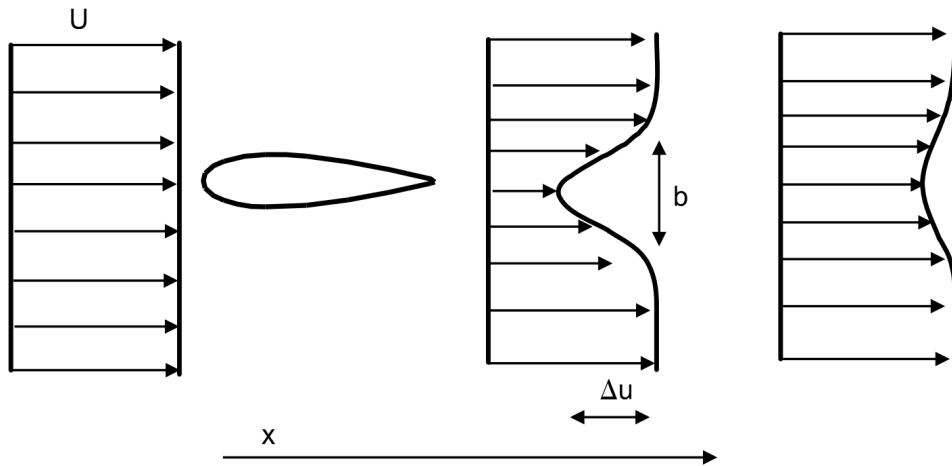


Figure 2.7: Wake behind a body. Reproduced from [19].

Generally, wake flow can be divided up into three zones [17, 19, 20], as visualized in Fig. 2.8. Close to the trailing edge there will be a near-wake or dead water zone, followed by a mixing zone before the far-wake or pure wake is developed. The flow in the dead water zone is characterized by circulation of fluid from the upper and lower shear layers. At a distance L_f from the trailing edge, the mixing zone starts and momentum is transferred between the wake flow and the free stream. In this zone, the upper and lower shear layers interact which may initiate vortex shedding. This flow phenomenon is represented by the blue lines in the figure and will be described in further detail in the next subsection. When pure wake flow is obtained, the wake width has increased and the velocity profile will have a self preserving shape [19].

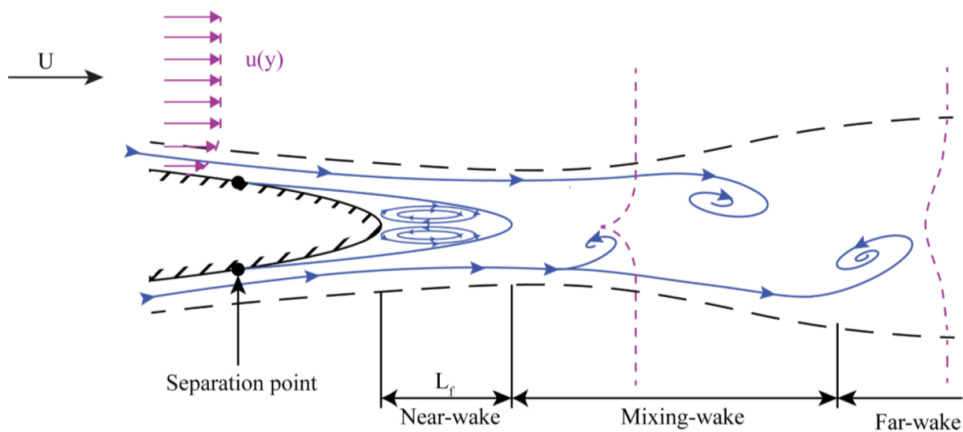


Figure 2.8: Separation points, wake flow and velocity profiles downstream of a body. Reproduced from [21].

As shown in Fig. 2.9, the angle of attack on bodies such as hydrofoils affects the location of the separation point and the wake size. For large angles of attack, the separation point tends to move upstream towards the leading edge on the upper surface of the foil, the suction side. The

width of the wake increases with an increasing angle of attack. Stall occurs if the critical angle of attack is exceeded, and the separation bubble covers almost the entire upper surface of a foil [15, p. 610-643]. Since the guide vanes are adjustable, the angle of attack will correspond to the turbine operating at different loads.

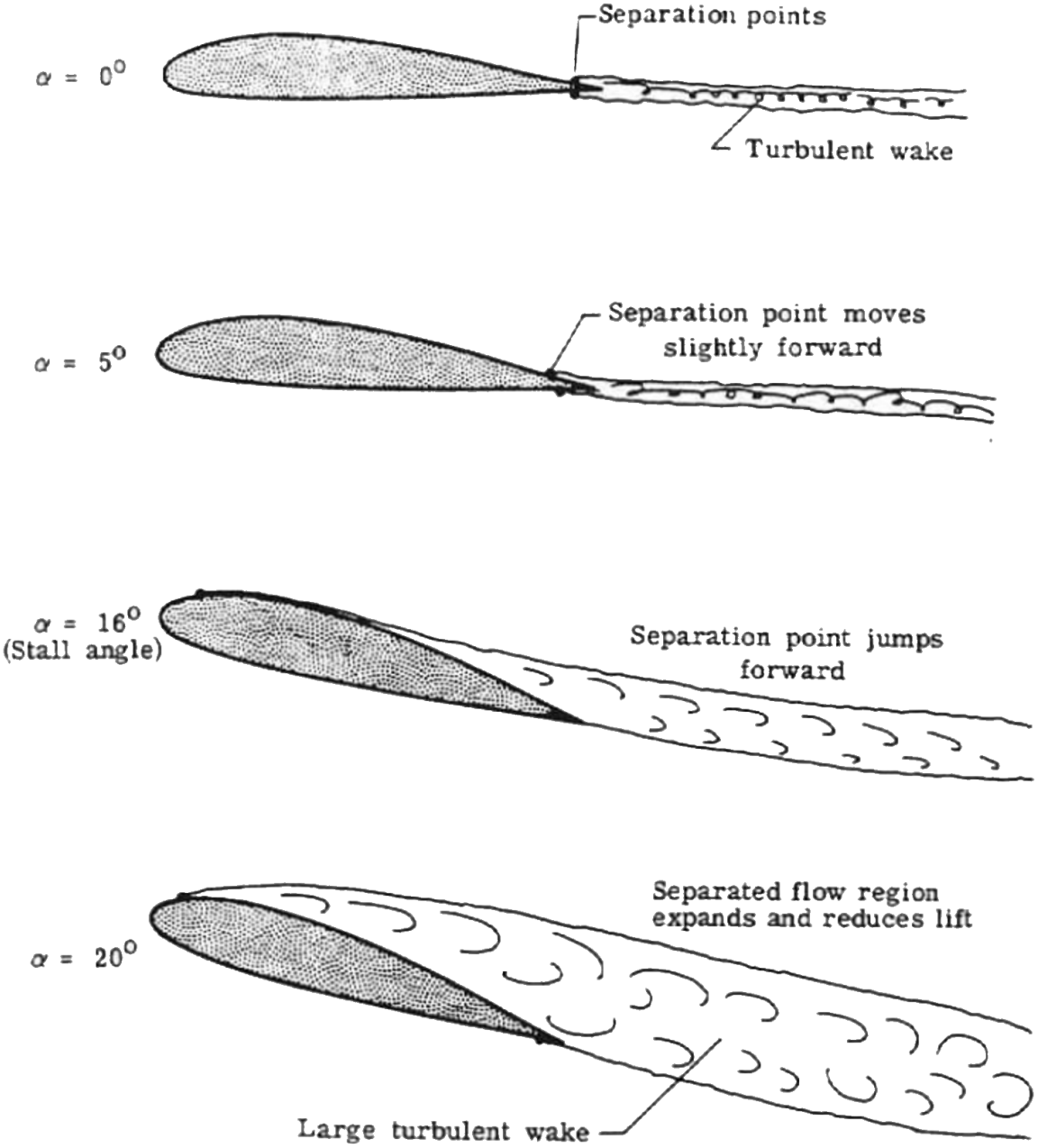


Figure 2.9: Separation point and wake for different angles of attack. Reproduced and modified from a PowerPoint presentation [22].

2.2.3 Vortex shedding

Vortex formation behind bluff bodies was first observed in experiments by Strouhal in 1878 [23]. A vortex is associated with the rotating motion of fluid around a centre line, and is the formation and shedding of a circulating fluid structure [15, p. 156-157].

Vorticity can be produced by different mechanisms. As previously explained, there will be boundary layers adjacent to the upper and lower surfaces of a foil that is subjected to a moving stream. In the thin boundary layer the velocity will increase from being zero at the surface because of the no-slip boundary condition, to being close to the free stream velocity. Hence, the v_x -velocity varies greatly with y , while the v_y -velocity gradients are small in this layer. From the definition of vorticity in (2.4), the vorticity in the boundary layer will be as shown in (2.5) [15, p. 156-157].

$$\vec{\omega} = \nabla \times \vec{v} \quad (2.4)$$

$$\vec{\omega} = \left(\frac{\partial v_y}{\partial x} - \frac{\partial v_x}{\partial y} \right) \vec{z} \approx -\frac{\partial v_x}{\partial y} \vec{z} \quad (2.5)$$

Here v_y denotes the y -component of the velocity, while v_x denotes the x -component of the velocity. Vortices with a negative value of vorticity will rotate clockwise, which can be demonstrated in the following example. Downstream of the separation point shown in Fig. 2.6, the vortices formed from the backflow will have a clockwise rotation seen from a physical perspective. The same figure shows that the partial derivative of the streamwise velocity with respect to the perpendicular variable to the streamwise velocity yields a positive value. From (2.5), the vorticity will consequently have a negative value. With the same reasoning, vortices with positive values correspond to anticlockwise rotating.

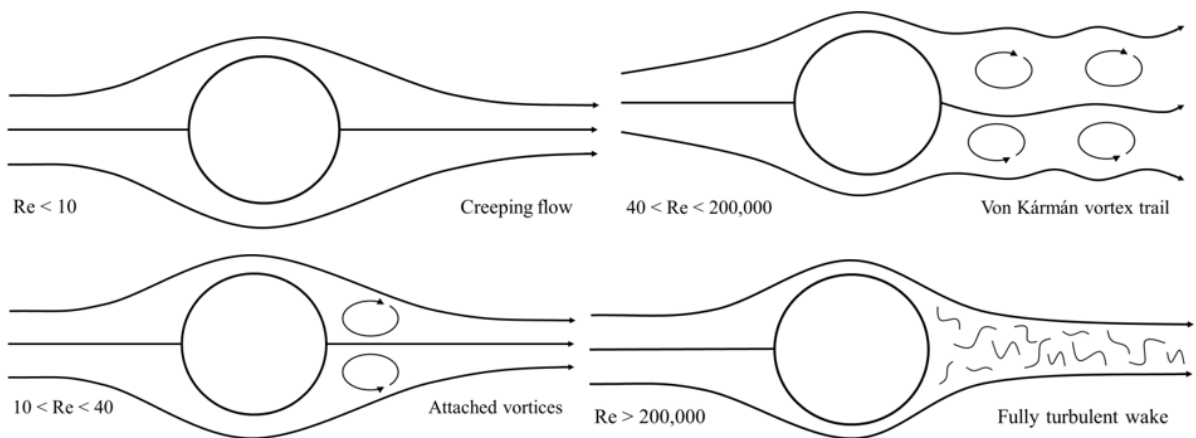


Figure 2.10: Flow around a cylinder for different Reynolds numbers. Reproduced from [24].

Vortex shedding is a flow phenomenon that occurs, under certain conditions, when a structure is subjected to a moving stream. Low-pressure vortices start forming and shedding in the wake region as a consequence of boundary layer separation. Separation of the boundary layer occurs both on the upper and lower surfaces. As a result, two shear layers are developed downstream of the body. The velocity gradients in the shear layers initiate the generation of vortices. Initially, a pair of vortices are formed in the separated region because of the velocity difference between the innermost and the outermost portions of the shear layer. One of the vortices will always break away first and move downstream in the wake, while another will begin growing in its place. Later, the second mature vortex will break away [25]. Hence, a process is started whereby vortices are shaped and shed in an alternating manner from the two separation points at a frequency as shown in Fig. 2.10 up to the right.

Vortex shedding is dependent on the Reynolds number of that fluid flow. Fig. 2.10 shows how the flow around a cylinder evolves for different Reynolds numbers [24]. The figure shows that attached vortices are formed at Reynolds numbers between 10 and 40, and von Kármán vortex street appears for Reynolds numbers in the range from 40 to 200 000 [24, 26]. The figure also shows an upper row of clockwise rotating vortices and a lower row of anticlockwise rotating vortices.

Von Kármán vortex street is defined as the periodic generation of vortices caused by vortex shedding. This phenomenon occurs downstream of the trailing edge of a body. In hydraulic turbomachinery, von Kármán vortex street can be found downstream of the trailing edges of stay vanes, guide vanes and runner blades [26]. In Fig. 2.11, a von Kármán vortex street behind a circular cylinder is illustrated.

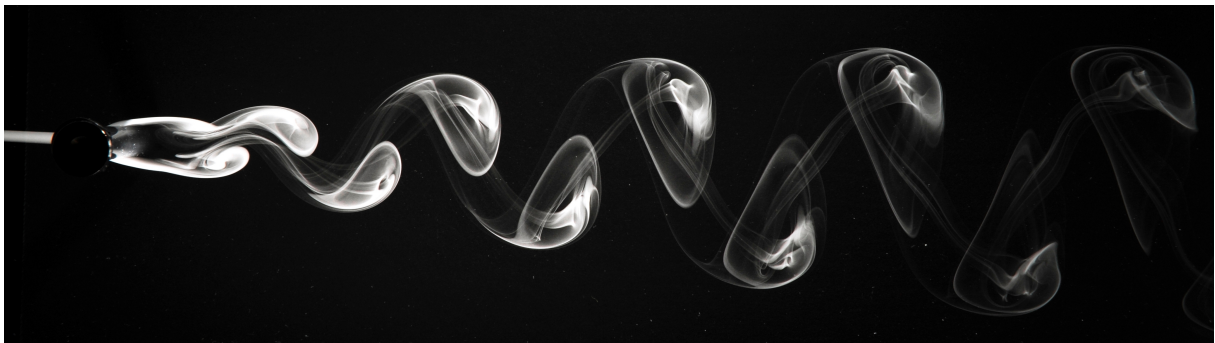


Figure 2.11: Visualization of the von Kármán vortex street behind a circular cylinder in air flow. Reproduced from [27].

The alternating vortex shedding in the wake of the body induces periodic pressure variations on the structure. For each formed vortex, both transverse and parallel forces to the free stream are employed on the body. The direction of the transverse force switches with the alternating shedding vortices [28].

2.2.4 Vortex shedding frequency

A lot of research has been dedicated to estimate the vortex shedding frequency. In this subsection some different empirical formulas for calculating the shedding frequency and previous experiments will be presented.

The vortex shedding frequency for circular cylinders has been found to follow the Strouhal relation. Strouhal's number is defined in (2.6) [29].

$$St = \frac{f_s L}{U} \quad (2.6)$$

where f_s is the frequency of the vortex shedding, L is the characteristic length of the body under consideration, and U is the free stream velocity.

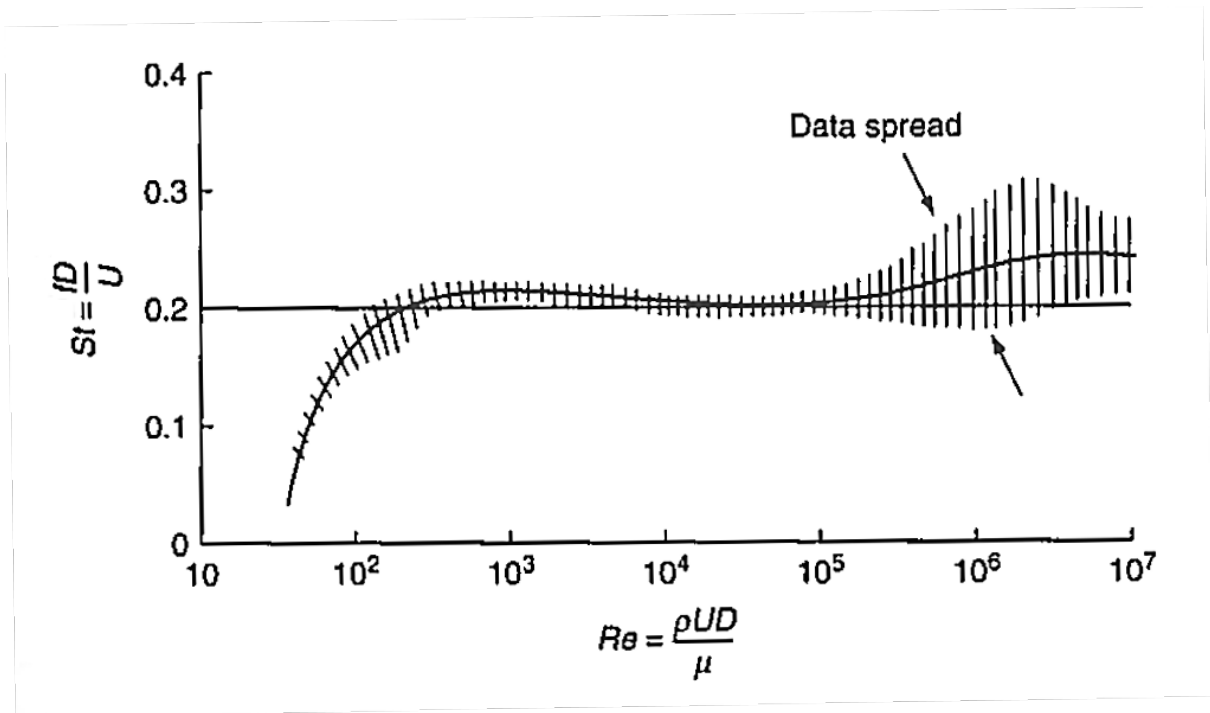


Figure 2.12: Strouhal number as a function of Reynolds number for a circular cylinder. Reproduced from [29]

The Strouhal number has been found to be a function of the Reynolds number for a given cross-section. In Fig. 2.12, the Strouhal number is plotted as a function of the Reynolds number for a circular cylinder. As can be observed, for circular cylinders the Strouhal number is approximately at 0.2 for a wide range of Reynolds numbers [29, 30]. By assuming a Strouhal number of 0.2, reorganizing of (2.6) gives the vortex shedding frequency:

$$f_s = St \frac{U}{L} = 0.2 \frac{U}{L} \quad (2.7)$$

Although the Strouhal relation proved to be a good estimate of the vortex shedding frequency behind cylinders, Gongwer [31], Donaldson [32] and Heskestad/Olberts [28] modified the Strouhal formula to make it suitable for runner blades.

Gongwer [31] suggested to take into account the trailing edge thickness, t , and virtual boundary layer thickness, δ_v , in the calculations of the vortex shedding frequency:

$$f_s = St \frac{U}{t + \delta_v} \quad (2.8)$$

It is important to note that the trailing edge thickness, t , is in unit millimetres. Empirically, the virtual boundary layer thickness can be estimated as [31]:

$$\delta_v = 0.0293 \frac{c}{(Re_c)^{\frac{1}{5}}} \quad (2.9)$$

Where c is the chord length of the blade, and Re_c is the chord based Reynolds number. Furthermore, Gongwer [31] found that a Strouhal number of 0.19 is more appropriate when using the sum of δ_v and c as characteristic length.

Based on the work of Gongwer, additional experiments on other trailing edge geometries were conducted by Heskestad and Olberts [28]. As opposed to Gongwer and Donaldson, a correlation between the vortex shedding frequency and the trailing edge geometry was found. Hence, the formula was modified in order to take into account the trailing edge geometry as follows:

$$f_s = St \frac{B}{100} \frac{U}{t + \delta_v} \quad (2.10)$$

Here, B , is a constant related to the geometry of the trailing edge. Its value for different trailing edge geometries can be found in Fig. 2.13.

In the work of Brekke [33, 34] it is presented a simplified formula, (2.11), which assumes a constant virtual boundary layer thickness of 0.56 mm and a Strouhal number of 0.19. The relative amplitude of the von Kármán vortex street is also found to be dependent on the trailing edge geometry, and is denoted by A in Fig. 2.13 [33, 34].

$$f_s = 190 \frac{B}{100} \frac{U}{t + 0.56} \quad (2.11)$$

It is important to note that all the aforementioned estimates of the vortex shedding frequency come from measurements of rectangular geometries upstream of the trailing edge, with parallel upper and lower surfaces. This is a simplification, and is usually not the case for actual vanes and blades in hydraulic turbomachinery. In addition, neither of the estimates take into account

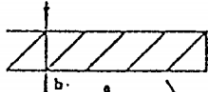
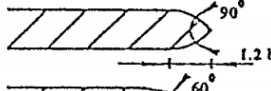
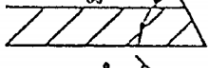
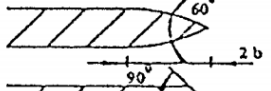
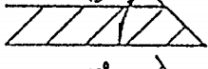
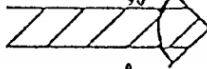
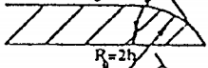
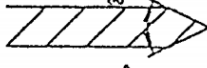
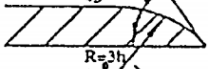
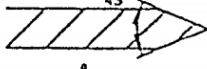
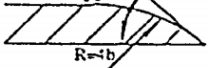
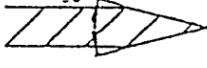
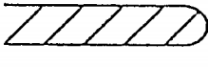
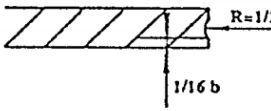
	A	B		A	B
	100 (100)	100		(0)	
	(45)			(0)	
	38 (20)	112		190 (230)	96
	3 (0)	131		380 (360)	93
	0	149		43	117
	0	181		0	159
	(260)			31 (43)	103

Figure 2.13: Geometry constants for different trailing edges. Reproduced from [33].

different angles of attack, and all formulas are based on measurements of isolated foils [28, 31, 33, 34]. Therefore the presented formulas are not necessarily applicable for guide vanes operating at different angles in a cascade.

Experimentally, the vortex shedding frequency can be investigated by spectral analysis. In a turbulent flow regime, the vortex shedding has been found to have frequencies appearing randomly about the nominal vortex shedding frequency [35–37]. As several frequencies coexist in turbulent vortex shedding regimes, the determination of the vortex shedding frequency is a matter of determining the most dominant frequency of the prominent frequencies. In the work of Sagmo et al. [38] the obtained frequency spectra for an isolated foil displayed a broad range of peaks resembling a Gaussian distribution about the vortex shedding frequency. An exception is when the shedding frequency is in proximity to the natural frequency of the structure, which will be explained in the next sub-subsection.

2.2.5 Lock-in

Natural frequency, f_n , is an inherent property of an object, and is the frequency at which a structure tends to oscillate in the absence of an outside force. If the shedding frequency approaches the natural frequency of the structure, a lock-in may occur. In this case the vortex shedding frequency will latch onto the natural frequency if in proximity, and stay equal to it over a range of flow velocities [39]. Lock-in is usually an unwanted effect, as it may lead to premature failure of a system due to a significant increase of the vibration amplitude [40].

The lock-in region is defined as the region at which the shedding frequency is close enough to the natural frequency, and the vortex shedding frequency may be locked-in at the natural frequency as illustrated in Fig. 2.14. The interaction between the fluid and the structure imposes a self-reinforced process that forces the vortex shedding frequency to be constant for a range of velocities [41]. It follows from the figure that the Strouhal's law is not valid for the lock-in region.

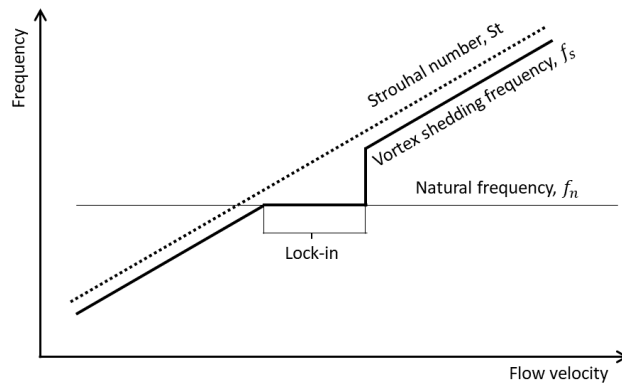


Figure 2.14: Vortex shedding frequency and natural frequency for increasing flow velocity.

According to Antonsen [19], the vortex shedding from the guide vanes will usually have high frequencies and low amplitude due to their typically slim profile and thin trailing edge. If resonance frequencies are avoided, the vortex shedding from the guide vanes will rarely results in severe problems. A central influence from the guide vanes is the viscous wake, and the creation of a non-uniform flow field in which the runner blades will rotate [19]. This is described in further detail in the next sub-subsection.

2.2.6 Rotor-stator interactions

A Francis turbine contains a supporting structure called a stator, and a rotating structure called a rotor. The stator consists of stationary vanes such as stay vanes and guide vanes, and the rotor consists of rotating runner blades. The interaction between the rotating and stationary blades that causes flow unsteadiness, is referred to as rotor-stator interaction (RSI). Even though the rotating runner blades are downstream of the vaneless space in a turbine frame of reference, some effects of the RSI propagate upstream, and hence influence the flow characteristics in the vaneless space [42].

Rotor-stator interaction in hydraulic turbomachinery can be classified into two different interactions; potential interactions, and wake interactions. [42]. Fig. 2.15 shows an overview of the different classifications of RSI. The shock interactions only apply if the fluid is compressible, and is not relevant to water flow applications.

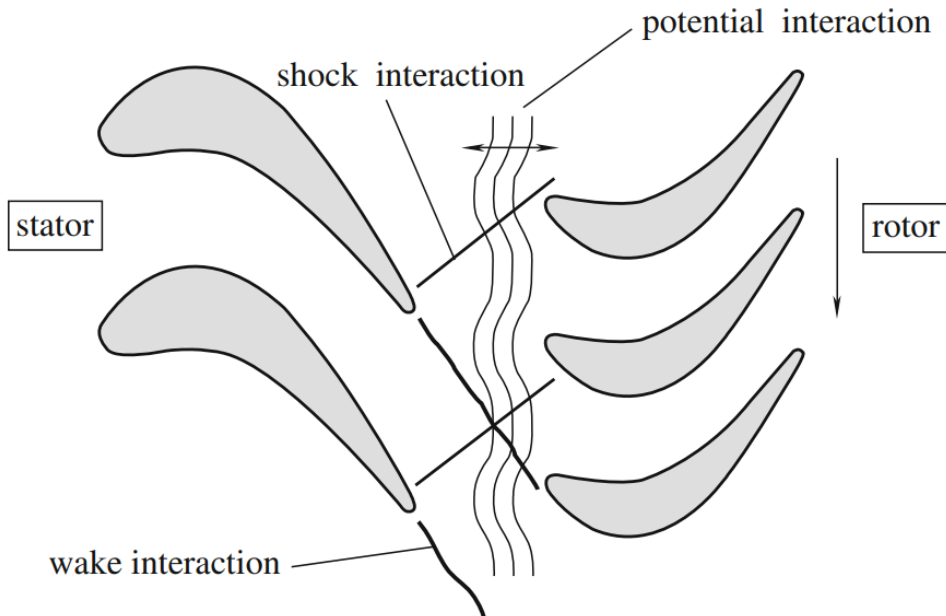


Figure 2.15: Different rotor-stator interactions. Reproduced from [42].

Flow unsteadiness caused by pressure waves is defined as potential interaction. The rotating runner blades cause periodical perturbations that propagate to the flow in the vaneless space. Flow field distortion in the vaneless space due to the pressure field caused by the runner is visualized to the left in Fig. 2.16. As observed from this figure, the velocity upstream of the leading edge of a runner blade is relatively low due to stagnation. The intensity of the potential interaction part of RSI is highly dependent on the size of the vaneless space. The most important potential interaction will arise in cases where the clearance gap between the guide vanes and the runner blades is small [42, 43]. This corresponds to larger guide vane openings in which one of the runner blades is in the closest position to a guide vane trailing edge.

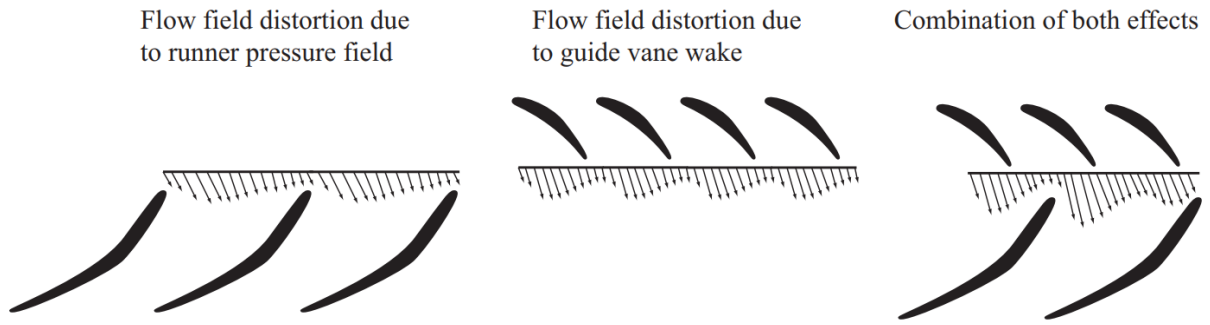


Figure 2.16: The effects of runner blades and guide vanes on the flow field. Reproduced from [44].

Wake interactions refer to the flow unsteadiness caused by viscous wakes from the upstream blade row, which in a turbine is the cascade of the guide vanes. Fig. 2.16 shows the reduced velocity in these wakes [43, 44]. Since the wake follows the slipstream of the guide vanes, the wake path varies with the guide vane angle. Fig. 2.17 illustrates how the interaction point moves for different guide vane angles due to the changes in wake paths. The effects on the flow caused by a wake are expected to reduce as the distance increases. A larger guide vane angle decreases the distance between the trailing edge of the guide vane and the interaction point. The wake is directed more towards the runner for larger guide vane openings, hence the viscous wake interaction in the vaneless space is expected to be the most visible at these guide vane angles [45].

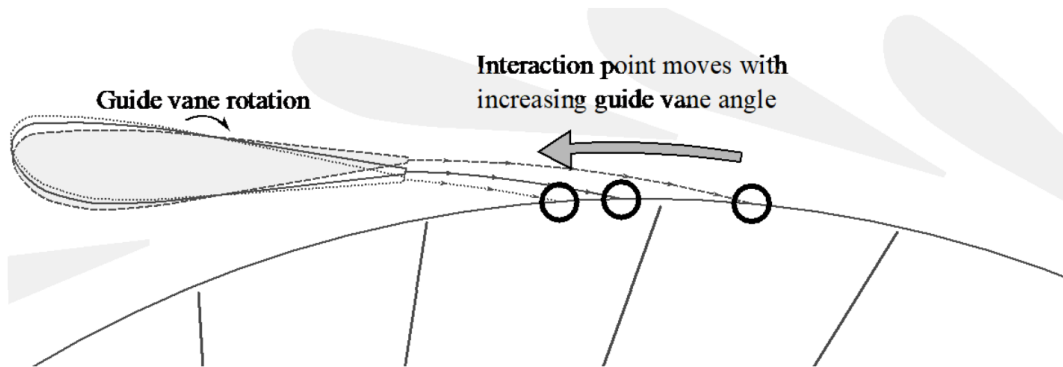


Figure 2.17: The viscous wake interaction point with the runner for different guide vane angles. Reproduced from [45].

There are two different frames of reference in a system consisting of both a rotating and a stationary part. In a stationary frame of reference, for instance in the vaneless space or at the guide vanes, the main frequency due to RSI is the runner blade passing frequency, f_{rb} [Hz], shown in (2.12) [46].

$$f_{rb} = \frac{nZ_{rb}}{60} \quad (2.12)$$

Where the rotational speed of the runner is denoted by n in rpm, and Z_{rb} is the number of runner blades. This blade passing frequency is found in the work of Su et al. [47] to coincide with the periodic changes of flow and pressure fluctuations at the runner inlet.

In a rotating frame of reference, for example at the runner blades, the main frequency due to RSI is the guide vane passing frequency shown in (2.12) [46]. The guide vane passing frequency, f_{gv} [Hz], can be computed according to (2.13) .

$$f_{gv} = \frac{nZ_{gv}}{60} \quad (2.13)$$

Where Z_{gv} is the number of guide vanes. In the work of Su et al. [47] the periodic cycle of the flow separation at the runner blade was found to correspond to the guide vane passing frequency. Performance and effective life of Francis turbines are highly influenced by the flow phenomena caused by RSI. Frequencies stemming from RSI can create, under certain conditions, severe pressure pulsations throughout the turbine. This can lead to fatigue, which may cause cracks in the turbomachinery [42].

2.3 Particle image velocimetry

In the following subsection the different subsystems of the PIV measurement technique will be discussed. At first, the PIC concept is presented, followed by an introduction to the particle seeding, light source and camera, calibration, interrogation area, evaluation, post-processing, power spectrum and uncertainty quantification of PIV in more detail.

PIV is a measurement technique that was developed in the 1980s [48, p. v], which makes it a relatively new measurement technique. This optical measurement technique enables the capturing of the entire velocity field of a flow. The flow field is measured indirectly by recording images of tracer particles in the flow at successive instants in time, and then calculating the flow's velocity based on the movement of the tracer particles within this time interval [49]. It is a non-intrusive measurement technique as it allows the sensors to be placed outside the flow. Both planar and volumetric velocity fields can be found through PIV measurements. However in this thesis, only two-dimensional PIV measurements will be examined.

The experimental set-up of a PIV system consists of the following subsystems: seeding, illumination, recording, calibration, evaluation, and post-processing. Fig. 2.18 visualizes an experimental arrangement for two-dimensional PIV [48, p. 8].

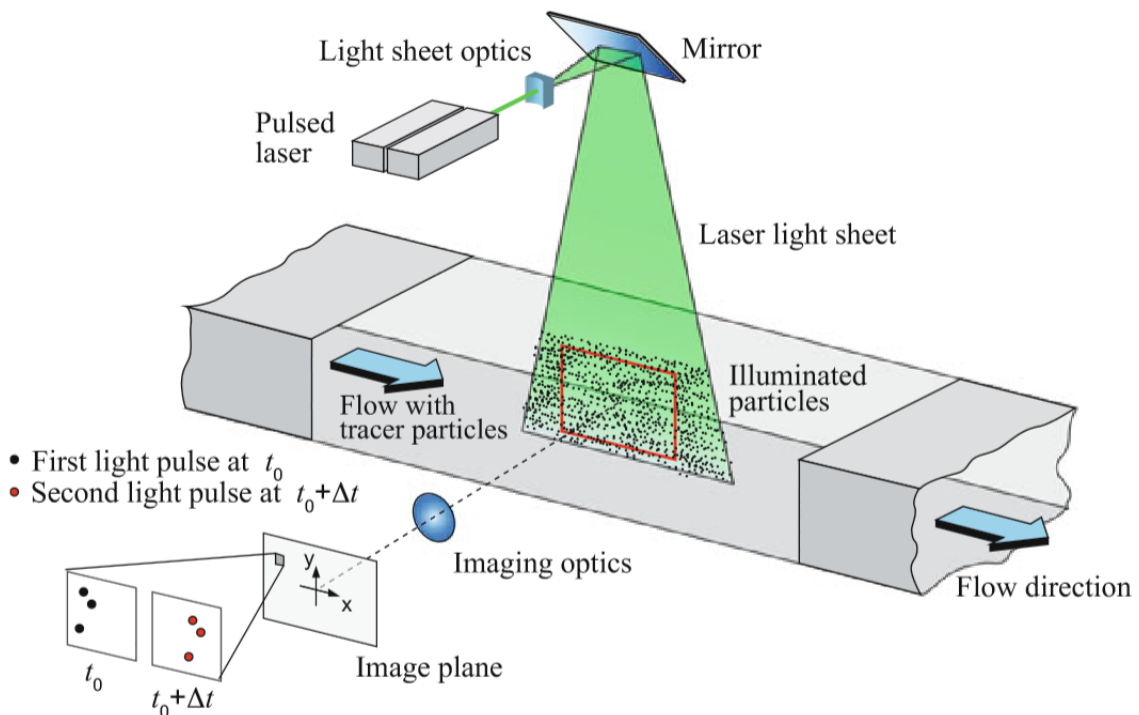


Figure 2.18: Experimental arrangement for PIV. Reproduced from [48, p. 8].

Prior to the measurement, tracer particles are added to the flow. The plane of interest within the flow, which will be referred to as the field of view (FOV), is illuminated twice by means of

a laser light sheet. Depending on the flow velocity, the time delay between the two laser pulses is selected. A camera located perpendicular to the laser sheet records the light scattered by the tracer particles on two separate frames that together make up one image. In order to evaluate the digital PIV recordings, the FOV is divided into small subareas called interrogation areas (IA). Local displacement vectors are computed with cross-correlation between the two frames for each IA. Hence, each IA results in one displacement vector. The velocity field can then be determined by taking into account the displacement vectors and the time delay between the laser illuminations [48, p. 8-15]. Processing of the PIV recordings is performed in a PIV software, and in this thesis DaVis 8.4 Software is used.

2.3.1 Seeding

A PIV measurement requires that the flow is seeded with particles acting like fluid tracers. The tracer particles need to follow the motion of the flow faithfully without interfering with the flow or the fluid properties. In addition, the scattering properties of the tracer particles need to be taken into account when determining which kind of tracer particles to use [48, p. 33-51].

In order to obtain neutral buoyancy condition, the density of the fluid, ρ , must be equal to the density of the tracer particles, ρ_p . If the neutral buoyancy condition is obtained, there will be no error due to gravitational forces. This condition is easier to achieve in water flows because of the high viscosity and typically lower speed compared to air flows. Therefore, larger tracer particles can be employed while still maintaining a good tracing fidelity [48, p. 33-51].

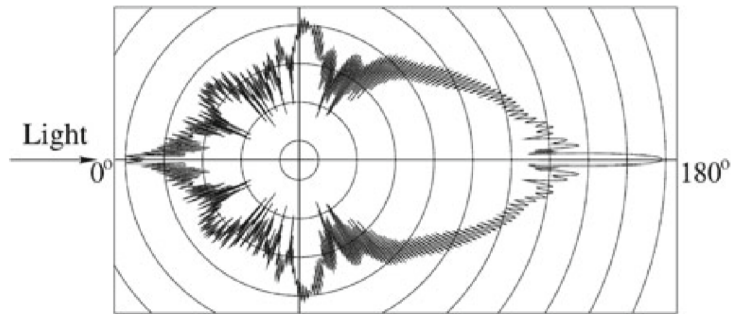


Figure 2.19: Light scattered by a 10 μm glass particle in water according to Mie theory. Reproduced from [48, p. 33-51].

The light scattered by the tracer particles is a function of the size, shape, and orientation of the particle, and the ratio of the refractive indices of the particles and the surrounding medium. There is a clear tendency that a larger particle size increases the scattered light intensity. However, the particles need to be small enough to act as good flow tracers and reduce the background noise. Mie scattering refers primarily to the elastic scattering of light from a particle for which the diameter is larger than the wavelength of the incident light. The Mie scattering diagram in Fig. 2.19, shows that the light is not blocked by the particles, but disperses in all directions.

Hence, the light captured by the recording lens is not only due to direct illumination, but also due to portions of light scattered by many particles. Consequently, a large particle density contributes to a scattering efficiency enhancement [48, p. 33-51].

The appropriate size of the tracer particles depends on the optical set-up and the magnitude of the flow phenomenon measured. According to Raffel et al. [48, p. 33-51], tracer particles used for PIV experiments in water typically have diameters in the range between 10 μm and 30 μm . Goyal, Gandhi and Cervantes [46] reviewed ten different PIV measurements executed in hydraulic turbines. The presented measurements used particle diameters in the range from 10 μm to 55 μm , where seven out of ten experiments used tracer particle with diameters between 10 μm and 20 μm . Even though these experiments can be useful suggestions, the tracer particle size should be seen in relation to the calibration of the imaging system, laser characteristics and camera resolution in order to avoid peak locking effects. Peak locking will be described further in detail in sub-subsection 2.3.8.

Regarding tracer particle material, hollow, coated glass spherical particles have proved to offer good scattering characteristics and good tracking capability for multiple water flow applications [50, 51]. The majority of the PIV measurements reviewed by Goyal, Gandhi and Cervantes used spherical glass particles [46].

Fig. 2.20 illustrates three different states of tracer particle image density, where the middle picture illustrates the density appropriate for PIV evaluation. The low and high particle image densities are appropriate in Particle Tracking Velocimetry (PTV) and Laser Speckle Velocimetry (LSV), respectively.

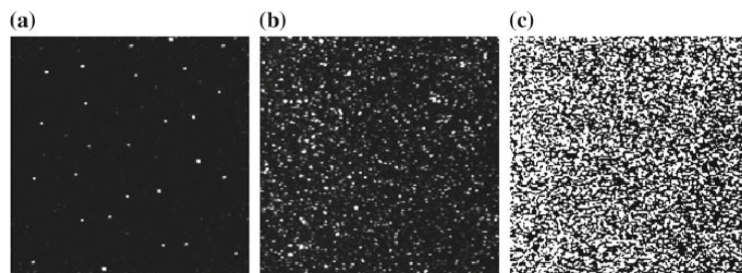


Figure 2.20: Three modes of tracer particle image density: **a** low (PTV), **b** medium (PIV), and **c** high image density (LSV). Reproduced from [48, p. 8-15].

2.3.2 Light source and camera

In PIV measurements, a laser is used as light source to illuminate the area of interest. The laser fires short pulses of light at a high repetition rate. In order to accommodate the low time delay between the pulses typically needed in PIV applications, the laser typically must operate in dual cavity mode. In this mode the two consecutive laser pulses originate from two separate laser cavities. As a consequence, a higher repetition rate is obtainable in this case than for a single laser cavity [48, p. 8-15]. Since the successive pulses are fired from different sources, it is important to ensure that the beams overlap. The beam overlap should be inspected both near field (0.2 - 0.8 m) and far field (3 - 5 m), and carefully adjusted for in accordance with the Product-Manual of Laser Guiding Arm [52].

A final laser beam overlap test should also be performed by recording a frame pair of a nearly still fluid injected with particles. By having a very small time delay between the pulses, Δt , one can examine whether the laser pulses illuminate the exact same area. Numerically this can be performed by checking the global normalized correlation values of all pixel intensities from first to second frame. DaVis 8.4 offers this function, the so-called beam-overlap value. A correlation value equal to 1 indicates identical particle patterns and hence a good beam overlap, while a value of 0 indicates that the beams are misaligned [53].

The laser beam is reshaped into a thin light sheet by means of a multiple-lens configuration. The lens configuration consists of cylindrical and spherical lenses in order to expand the beam in one axis and obtain the desired thickness, respectively [48, p. 60-80]. In 2D PIV, the velocity field is supposed to be measured only in two dimensions, hence a sufficiently thin laser sheet is desirable. As a rule of thumb, the fastest particle should not travel more than 1/4 of the light sheet thickness [46]. This is to avoid out-of-plane motion that refers to particles moving in and out of the light sheet. In multiple hydraulic machinery measurements, sufficient light sheet thickness is found to be between 0.5 to 5 mm to keep out-of-plane displacement of seeding particles low [46, 47, 54, 55].

The time delay, Δt , between the pulses is dependent on the flow velocity, and represents the time between the two frames of one image. It must be short enough to prevent too many particles with an out-of-plane velocity component to leave the light sheet. However, Δt needs to be long enough in order to determine the displacement of the tracer particles with sufficient resolution [48, p. 8-15]. The one-quarter rule is a common guideline for the maximum displacement and serves as an upper bound for the displacement between the two frames. This rule states that the maximum displacement of the particle images both in-plane and out-of-plane should be equal to or less than one quarter of the IA size in xy-direction and z-direction, respectively. A particle displacement of 5 to 10 pixels between the first and second frame is commonly suggested in literature to minimize the relative uncertainty [48, p. 203-229].

The image rate of a recording is the reciprocal of the time between each frame pair, and becomes

the frequency of the obtained images or vector fields. If a certain frequency in the velocity field is of interest to capture, the image rate has to be selected according to the Nyquist sampling theorem to avoid aliasing. The Nyquist sampling theorem states that the sampling rate has to be at least twice as large as the highest frequency in the signal that is to be sampled [56]. If this criterion is not met, the signal might be incorrectly reproduced. This distortion or artifact of a signal is known as aliasing. Fig. 2.21 shows the concept of aliasing. The black curve is the actual signal, while the blue curve is the sampled signal reproduced from the blue points indicating the sampling rate.

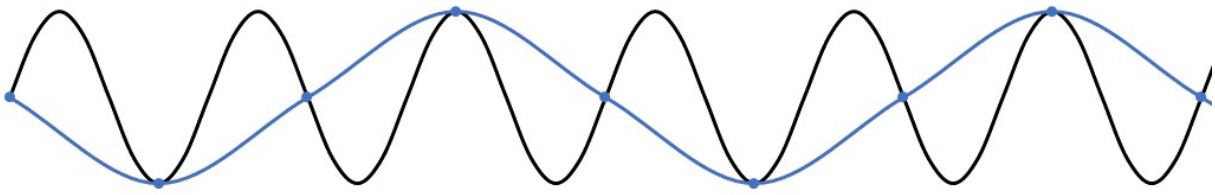


Figure 2.21: An example of aliasing as a result of under-sampling.

The distinction between Δt and image rate is illustrated in Fig. 2.22. In addition, the difference between frame and image is shown. The maximum image rate for a recording is determined by the spatial resolution of the camera. Hence, a lower resolution of the camera enables a higher image rate.

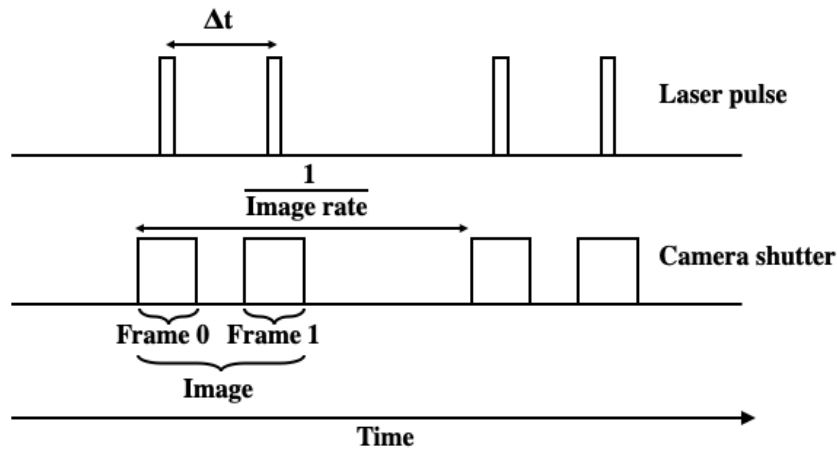


Figure 2.22: Time delay between pulses and image rate.

The recording subsystem consists of a digital camera that records the FOV synchronous with each illumination. In the recordings, each pair of successive exposures are grouped as two frames of one image. Electronic equipment is used for the matter of synchronizing the laser pulsing with the camera's frame rate timing sequence. In Fig. 2.23, the synchronization of a sCMOS image sensor with double pulsed laser system of type Nd:YAG for PIV is shown. Note that the time

delay between the pulses, Δt , is denoted by τ in the figure. As shown in the figure, the first frame associated with the first laser pulse, is exposed for a very short time while the second frame is exposed for an extended period of time. This corresponds to the readout time of the first recording from the sensor [48, p. 120-122]. A data acquisition system is used to record sequential images from the camera. The recordings are then transferred to the memory of a computer [48, p. 8-15].

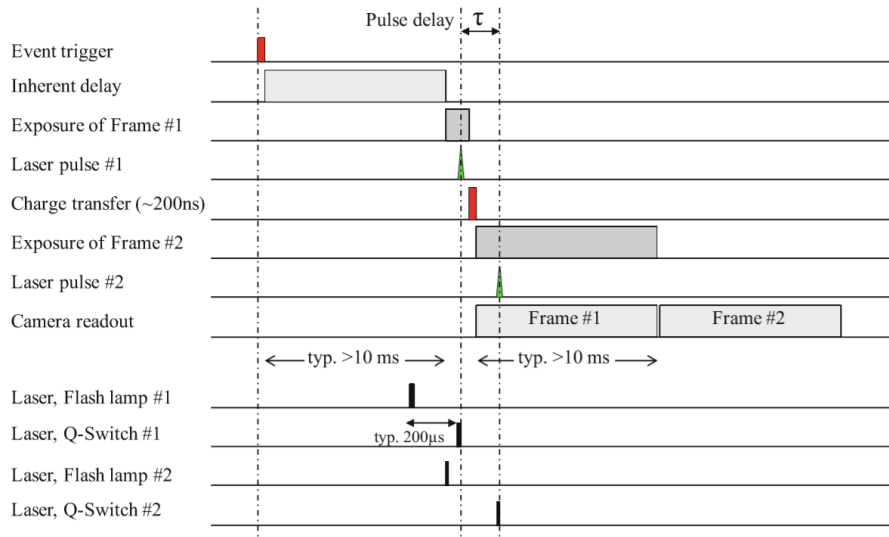


Figure 2.23: Timing diagram for dual-frame image capture with a sCMOS image sensor showing synchronization with double cavity pulsed Nd:YAG laser. Reproduced from [48, p. 120-122].

2.3.3 Calibration

In order to obtain results in scaled units that represent the true dimensions, a calibration of the measurement area is required. The actual spatial dimension can be related to the pixel size in the recording plane by means of a calibration target or calibration plate. Typically, the calibration target is covered by multiple equally spaced marks with known spatial dimensions, and is located to align with the centre of the light sheet plane. Usually, 20-30 identified marks on the calibration target in the FOV is sufficient [57].

In order to scale inter pixel distance, a fit mapping function can be applied to the marks found in the image. 3rd order polynomial functions or pinhole functions can be computed by DaVis 8.4 to create a grid defining the spatial dimensions. The average deviation of the dewarped mark positions to the grid is calculated by the software and presented as root mean square (RMS) of fit, in pixels. This value quantifies the precision of the calibration, and a low value indicates a high precision. The RMS of fit should be seen in relation to the camera resolution and the interrogation area used for evaluation. For a 2 megapixel camera a value lower than 1 pixel is considered good cause it is small in comparison, while a value higher than 2 pixel is considered

questionable [57].

From the calibration a scale factor can be obtained. The scale factor is determined by estimating the number of pixels covered by a known dimension in the imaging plane [55]. Its value is in pixels per millimetre and hence converts pixels to millimetres.

2.3.4 Interrogation area

Prior to the evaluation of images via correlation, the complete FOV is divided into IAs as illustrated in Fig 2.24. The evaluation will yield one velocity vector for each IA. The correlation can either be done in a single step or iteratively via multi-pass evaluation. Besides choosing between the single-pass and multi-pass interrogation schemes, DaVis 8.4 requires the user to decide the IA size(s) and the IA overlap percentage.

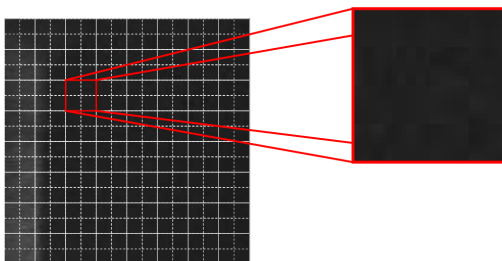


Figure 2.24: FOV divided into IAs. Reproduced from [58].

There are two types of pass interrogation schemes, single-pass and multi-pass evaluation technique. Single pass evaluation does not involve window shifting of the IA and the IA size is constant. Each vector calculation is done in one pass, therefore this is a relatively fast method [53].

In multi-pass evaluation the vector field can be calculated by an arbitrary number of iterations on the same image with either a constant or decreasingly smaller IA size. In the first pass a reference vector for each IA is computed and used as a best-choice window shift in the next pass. In this manner the window shift is adaptively improved to calculate the vectors in the following steps more accurately. Multi-pass interrogation schemes enhance the signal-to-noise ratio of the correlation peak, but compromises the processing time [53]. If a decreasingly smaller IA size scheme is used, both an initial and final IA size must be defined by the user. As the final IA size can be chosen smaller than the initial one, the spatial resolution of the vector field is improved by this scheme compared to a multi-pass evaluation with constant IA size.

As every IA produces one velocity vector, the resolution of the velocity field increases with smaller IA sizes and overlapping IAs. However, seeding density, laser thickness and flow velocity in the measurement area have to be taken into account when choosing the appropriate size of the IAs. Literature commonly suggests that each interrogation area should have a seeding density of

at least 10 particle images [49, 55, 59, 60], and the particle image displacement between frames should be less than one quarter of the IA in xy-direction and z-direction [60, 61]. However, in the case of multi-pass evaluation with a decreasing IA size, these criteria only apply for the initial IA. The final IA size only needs a particle image density of at least 5 [48, p. 203-229]. To increase spatial resolution, the IAs can partially overlap with their neighbours. A higher percentage overlap increases the processing time.

Fig. 2.25 shows the different correlation functions corresponding to different seeding densities N_{ppp} within a 32×32 pixel IA. An increased seeding density causes the signal strength of the correlation peak to increase with respect to correlation noise. This will lead to a reduced uncertainty of the shift vector [48, p. 203-229].

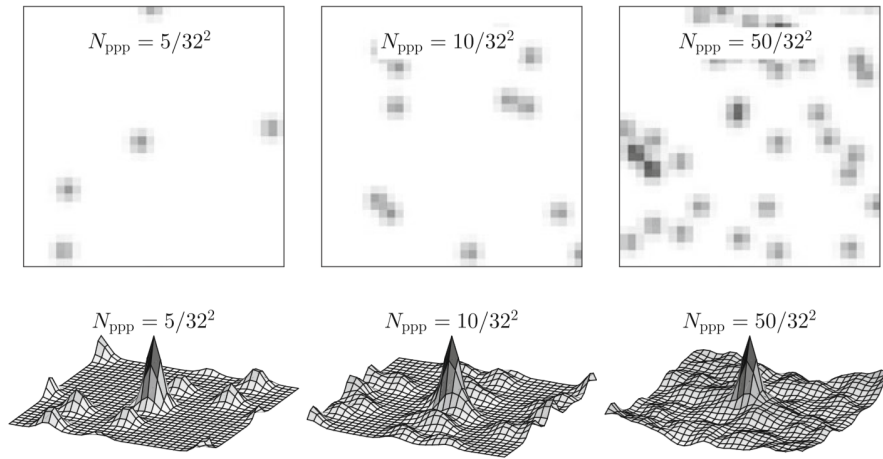


Figure 2.25: PIV images with varying seeding densities and the corresponding correlation functions. Reproduced from [48, p. 203-229].

2.3.5 Evaluation

Cross-correlation is the statistical evaluation method used to obtain a local displacement vector from each pair of IAs. By taking into account the known time delay between frames for which the displacement vector is made, local velocity vectors can be computed. All vectors are then combined to yield a complete 2D vector field of the image. The velocity fields present the opportunity of deriving several other flow parameters.

Each particle image in the first frame can be matched with a number of different particles in the second frame. Therefore the displacement vector is determined statistically from the movement of the ensemble of particles. The cross-correlation function statistically measures the degree of match between the two samples for a given image shift. The highest value in the cross-correlation plane, also called the peak, can then be used as a direct estimate of the particle image displacement [48, p. 145-171]. For further explanation of the cross-correlation technique, the reader is

referred to Raffel et al. [48, p. 145-171].

In Fig. 2.26, the cross-correlation function is computed for the two samples. The first frame or sample, is denoted I , while the second frame is denoted I' . Within I' the white rectangle indicates the best match of I , and illustrates the image shift for the given case. The cross-correlation plane indicates that the mean shift of the particle images is approximately 12 pixels to the right. [48, p. 145-171].

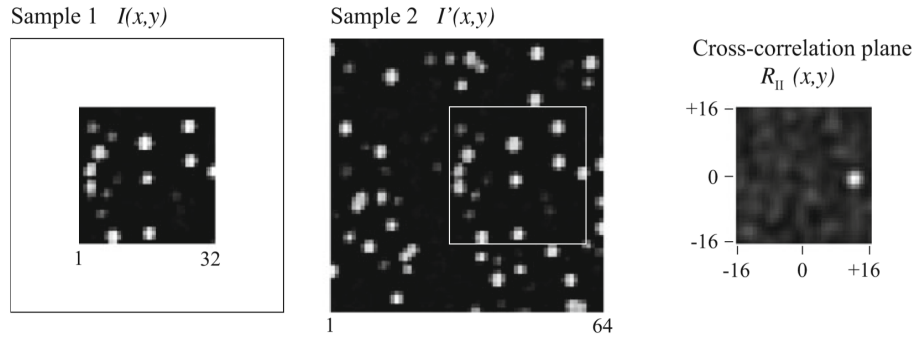


Figure 2.26: Two consecutive samples and their cross-correlation plane. Reproduced from [48, p. 145-171].

The cross-correlation plane is computed from the cross-correlation function, R_{II} . For each choice of image shift, (x, y) , the sum of the products of all overlapping pixel intensities produces one cross correlation value, defined in (2.14) [48, p. 145-171].

$$R_{II}(x, y) = \sum_{i=-K}^K \sum_{j=-L}^L I(i, j)I(i + x, j + y) \quad (2.14)$$

Fast Fourier transform (FFT) is commonly used in PIV software to calculate the cross-correlation for the purpose of decreasing computational operations. FFT uses the correlation theorem showed in (2.15), that states that the cross correlation of two functions is equivalent to a complex conjugate multiplication of their Fourier transforms [48, p. 145-171].

$$R_{II} \iff \hat{I} \cdot \hat{I}'^* \quad (2.15)$$

\hat{I} and \hat{I}' are the Fourier transforms of the functions I and I' . The term on the right hand side is inversely Fourier transformed in order to compute the cross-correlation plane [48, p. 145-171]. This procedure is illustrated in Fig. 2.27.

It is often advantageous to perform image pre-processing prior to cross-correlation because it may result in enhanced correlation signals. The correlation signal is strongly affected by the image intensity, and the brighter particle images will have a dominating influence on the correlation peaks compared to the weaker particle images. Background noise in the images causes the

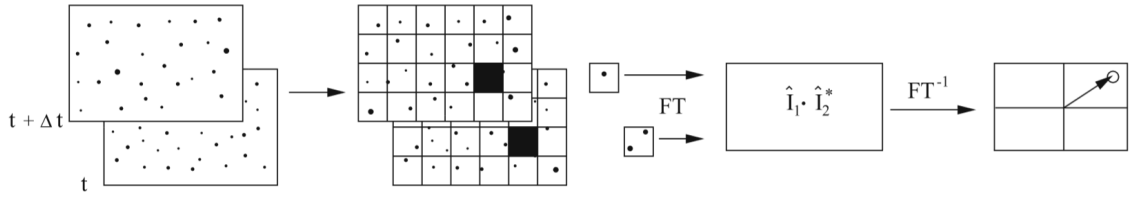


Figure 2.27: Analysis of double frame recordings using the digital cross-correlation method. Reproduced from [48, p. 145-171].

shift vector uncertainty to increase and results in a loss-of-correlation. Fig. 2.28 shows how the correlation functions change with different background noise levels σ_n/I_0 . This figure illustrates the effect of loss-of-correlation due to image noise [48, p. 203-229].

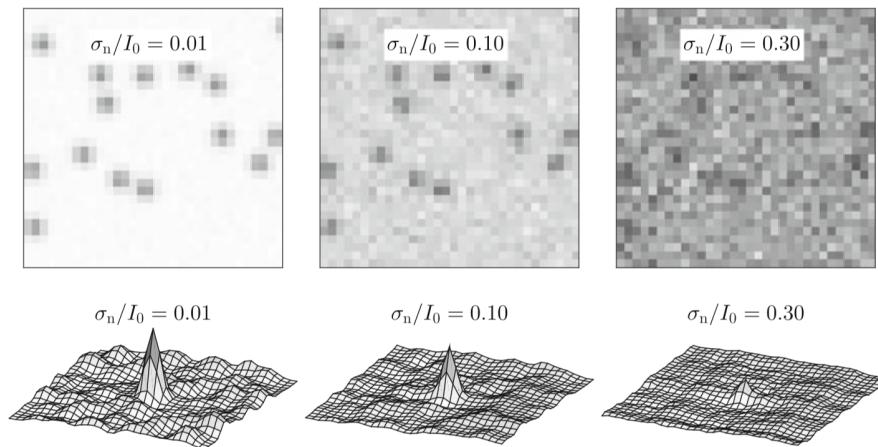


Figure 2.28: PIV images with varying background noise level and the corresponding correlation functions. Reproduced from [48, p. 203-229].

There are many image enhancement methods such as background subtraction, high-pass filters, image binarization, low-pass filters and range clipping, but only the first two methods will be explained as these have been applied to the results later presented. Background subtraction from the PIV recordings decreases the effects of laser flare and other stationary image features. The background subtraction can either be performed by a recording of the FOV without seeding, or by recording of a sufficiently large number of raw images that can make up a basis for an average or minimum intensity image of the background. A high-pass filter can remove the background variations with low spatial frequency. This way, the large intensity fluctuations in the background may be filtered out while the small intensity fluctuations of the particle signal will pass through [53, 61].

2.3.6 Post-processing

Spurious vectors in the velocity field contribute to error in velocity results. This brings up the need for a proper validation scheme for spurious vectors, which in PIV is referred to as post-processing. A typical feature of spurious velocity vectors, frequently called incorrect velocity vectors, is that their magnitude and direction significantly deviate from the surrounding neighbours. They may appear as isolated spurious vectors or clustered in groups [48, pp. 243-256]. In Fig. 2.29, both isolated and clustered spurious vectors can be observed. The amount of spurious vectors usually arises with poor seeding, low light levels, strong out-of-plane motion or a high degree of small-scale turbulent components in the flow [53].

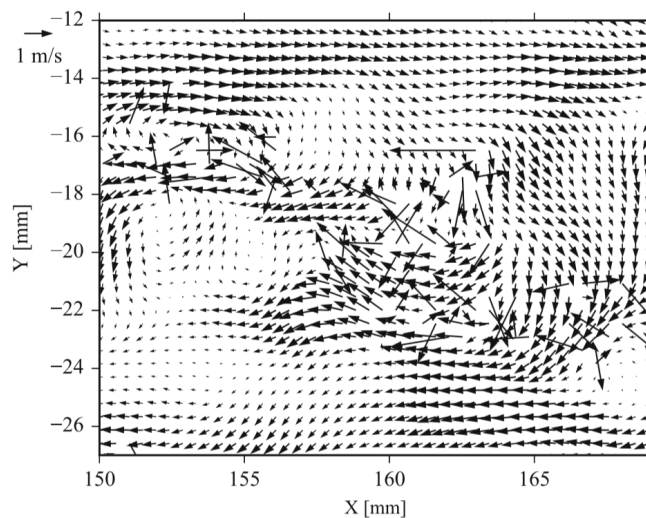


Figure 2.29: An area with a large number of incorrect velocity vectors. Reproduced from [48, pp. 243-256].

Human perception is very efficient in detecting spurious vectors. However, since PIV measurements often involves great amounts of data, visual detection of spurious vectors is not viable. This promotes the need for a purely statistical approach for the post-processing of the PIV data. Several different validation algorithms for PIV can be found in literature, and the reader is referred to Raffel et al. [48, pp. 243-256] for an extensive overview. Westerweel [62] proposes a validation scheme for spurious velocity vectors by means of a median filter. The validation method used in the post-processing in DaVis 8.4 is based on this validation scheme [53] and will be explained in more detail. In order to explain this detection scheme, some notations are important to define. Fig. 2.30 shows eight neighbouring grid points for one spurious velocity vector in two dimensions, $U(i, j)$ and $V(i, j)$.

The median of the velocity vectors is computed by arranging up to eight neighbour velocity vectors according to their magnitude. Each velocity component, U and V , is separately arranged. If eight neighbour vectors exist, the average of the fourth and fifth value in the sorted list is defined as the median value, U_{med} and V_{med} . This procedure prevents big outliers at either end

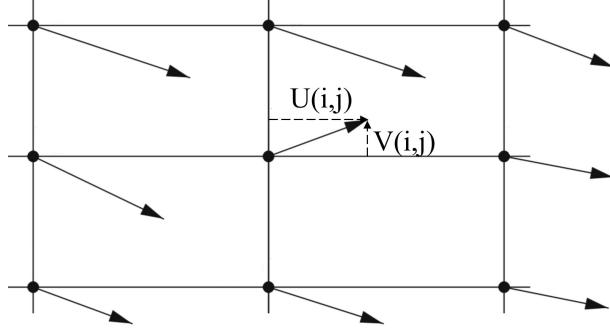


Figure 2.30: Sketch of data grid points with vector notations.

of the sorted list to affect the median value [53]. Next, the standard deviation is calculated for both velocity components, yielding U_{rms} and V_{rms} . The median test is shown in (2.16) and (2.17), for U- and V-component respectively [53].

$$U_{median} - f \cdot U_{rms} \leq U(i, j) \leq U_{median} + f \cdot U_{rms} \quad (2.16)$$

$$V_{median} - f \cdot V_{rms} \leq V(i, j) \leq V_{median} + f \cdot V_{rms} \quad (2.17)$$

Here, f is a user-specified factor [53]. The velocity vector under inspection is considered valid if both these criteria hold. If not valid, the velocity vector will be regarded as a bad vector and removed from the vector field.

If a velocity vector has been identified as false, the 2nd, 3rd and 4th highest correlation peaks are checked whether they meet the given criteria for replacement. The replacement criteria may be the same as the ones given above, but a lower user-specified factor may be implemented to obtain a stricter replacement criterion [53].

2.3.7 Power spectrum

From a velocity field, a power spectrum analysis can be carried out. In DaVis 8.4 the computation of the power spectrum is based on discrete-time Fourier transform of the velocity development over time at a specific point or in an area. The Fourier transform decomposes a time-domain signal into a frequency-domain signal, and the concept will be described as follows.

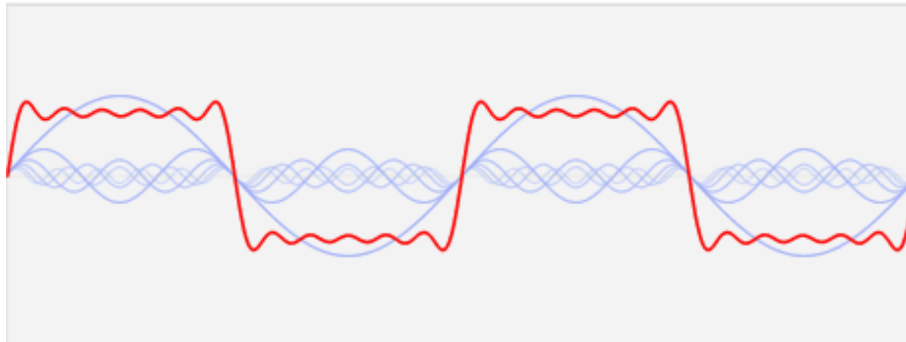


Figure 2.31: Input function (red) approximated by six sinusoidal functions (blue). Single shot of an animation by LucasVB [63].

Fourier proved that any signal can be represented or approximated by a number of sine and cosine functions [56]. The summation of these sine and cosine functions is called a Fourier series. An illustration of this concept is shown in Fig. 2.31, where the red input function is decomposed into six blue sinusoidal functions. Each sine and cosine function will have a respective frequency and amplitude [56]. Hence, a frequency domain of the function can be created from the Fourier series shown to the right in Fig. 2.32. In the frequency domain, the x-axis represents the frequency and the y-axis represents the peak amplitude of the sinusoidal functions.

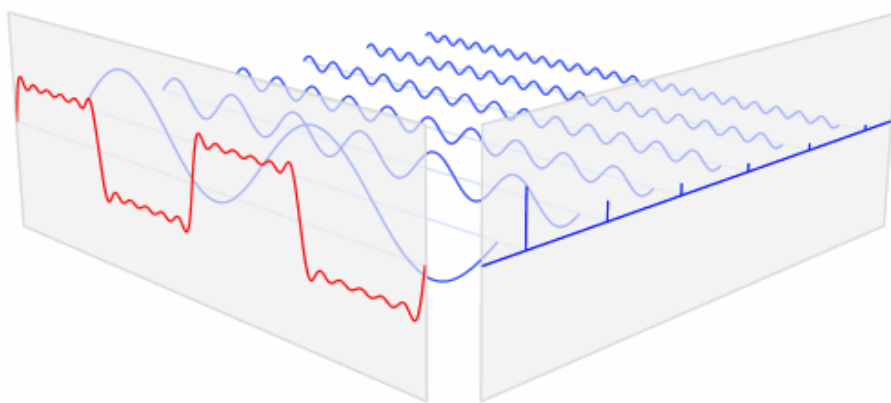


Figure 2.32: Resulting peaks in the frequency domain of the function. Single shot of an animation by LucasVB [63].

This way, periodical fluctuations in the velocity over time at a certain point or in an area can be transformed into Fourier series with respective coefficients.

2.3.8 Quantifying uncertainty of PIV measurements

Any experimental measurement will contain some level of error. Error is the deviation of a measurement from its true value. As the true value is rarely known, the term uncertainty is commonly used. The uncertainty describes the possible error or range of error which may exist in a measurement. According to GUM [64], accuracy is defined as the degree of conformance of a measured value to its standard or known value. Precision refers to how well two or more observations agree with each other. High accuracy requires both high trueness and high precision [64]. Fig. 2.33 shows the difference between accuracy and precision.

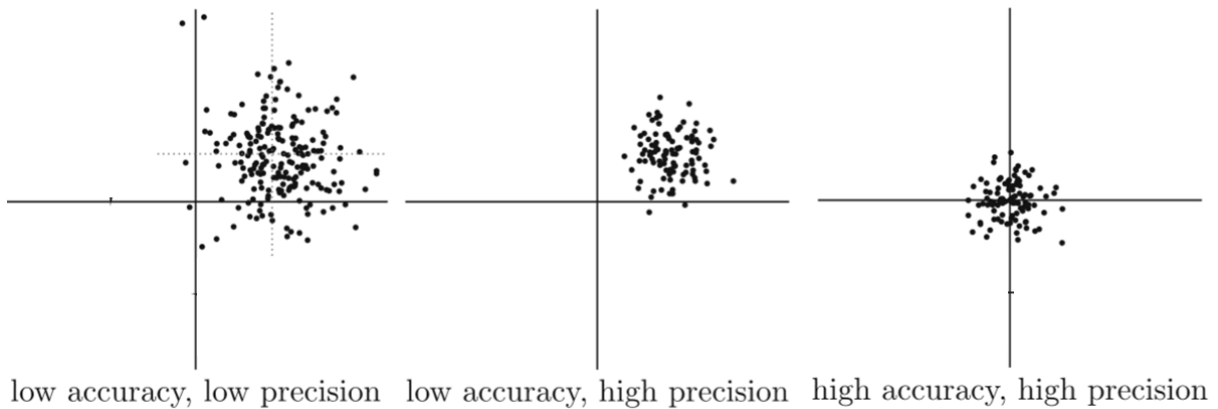


Figure 2.33: The concept of accuracy and precision illustrated. A modified version from [48, p. 203-229].

Errors and uncertainties can be classified into three types, spurious, systematic and random. Spurious errors are due to human and instrumental failure typically caused by accident. Repeated measurements do not provide information on spurious errors, unless the introduction of the error occurs during the repetitions. Good supervision, maintenance, inspection, and training can minimize the chance of spurious errors [65].

Systematic errors are errors that persist and cannot be considered random. They usually cause persistent error on one side of the true value. These kind of errors are due to deviations from standard device dimensions, abnormalities to the installation and potential bias in the calibration. Repeated measurements cannot remove or detect systematic errors [65].

The random error of a measurement is typically non-predictable. Its magnitude and sign may vary for each single measurement. The experimental standard deviation characterizes the dispersion about the mean of the observed values. Hence, it is a measure of the uncertainty of the mean due to random effects [64]. The arithmetic mean value of x , \bar{x} , can be calculated:

$$\bar{x} = \frac{1}{N} \sum_{k=1}^n x_k \quad (2.18)$$

where N is the sample size. The experimental standard deviation or sample standard deviation,

$s(x_k)$, can then be computed as follows

$$s(x_k) = \left[\frac{1}{N-1} \sum_{j=1}^n (x_j - \bar{x})^2 \right]^{\frac{1}{2}} \quad (2.19)$$

A PIV measurement involves multiple variables and instruments which makes quantifying the uncertainty far more complex than most measurement techniques. However, DaVis 8.4 Software do provide some methods to quantify the error of a PIV measurement. In the results presented later the systematic error source caused by peak locking, random errors from cross-correlation and uncertainty of the average vector field have been investigated. For that reason, these methods will be presented as follows.

Peak locking is a significant systematic error source in PIV. Peak locking occurs when the particle image size becomes too small and its continuous intensity distribution is insufficiently sampled by the discretized digital camera sensor. If the particle image is represented by one pixel with maximum intensity while the adjacent pixels have low intensities in same order as the image noise level, the sub-pixel positions is lost and cannot be recreated [48, p. 203-229]. In this case the centre of the particle image will be estimated to the middle of the pixel by the software, and its measured location and displacement will tend to be biased towards integer values.

A displacement histogram such as shown in Fig. 2.34, is a way of displaying the degree of peak locking effects. In the figure, large peak locking effects are illustrated in the left histogram where there are large peaks in each integer. Such a distorted histogram may indicate that the systematic errors are larger than the random noise in the displacement estimates. Peak locking can also be observable in the velocity field when the variation of the measured velocities is small and vortices are present in the flow. In this case the vortices become more rectangular in shape instead of circular. Systematic errors due to peak locking can be prevented by having particle image diameters of at least two pixels [48, p. 203-229].

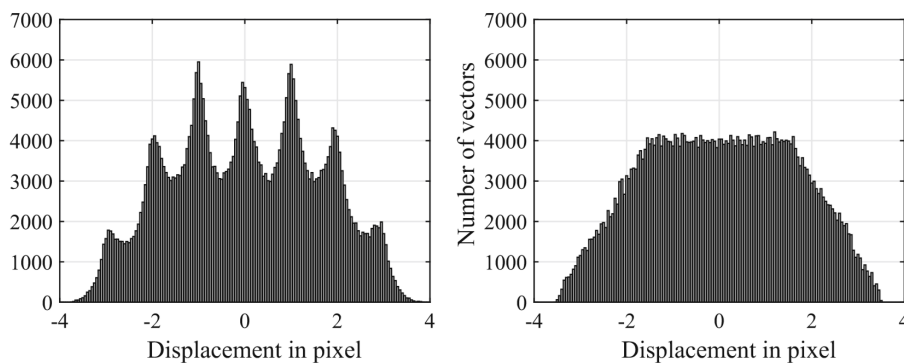


Figure 2.34: Histograms of the estimated displacement. **Left:** a particle image diameter of 1 pixel illustrating peak locking. **Right:** a particle image diameter of 3 pixels. Reproduced from [48, p. 203-229].

DaVis 8.4 Software computes a histogram of the decimal places of the velocity components for each vector field. From the centre of mass of the histogram, a peak lock value is calculated. According to the manual for DaVis 8.4 Software [66] a peak lock value below 0.1 indicates a satisfactory degree of peak locking, while a value of 1 indicates strong peak locking effects.

A method for quantifying the uncertainty from correlation statistics is introduced by Wieneke [67]. This method involves mapping the second image frame from the PIV evaluation onto the first image frame by using the computed displacement vector. The uncertainty of each displacement vector is derived by using a statistical analysis of how each pixel contributes to the cross-correlation peak shape. A detailed presentation of this method can be found in [53, 67]. This method is tested with synthetic data for varying random Gaussian noise, particle image size and density, in-plane and out-of-plane motion, and is shown to provide an accurate estimate of the true random error [67]. Davis 8.4 Software offers the user to calculate the uncertainty from correlation statistics for each vector in the instantaneous vector fields.

The uncertainty of the time-averaged absolute velocity field, $\Delta|V|$, can be calculated in DaVis 8.4 by the relation shown in (2.20) [66].

$$\Delta|V| = \sigma_{|V|} \sqrt{\frac{1}{N_{eff}}} \quad (2.20)$$

Here, $\sigma_{|V|}$ denotes the standard deviation in $|V|$ across all samples during a measurement series, and N_{eff} is the effective number of the independent samples of $|V|$. N_{eff} takes into account the correlation between the absolute velocity vectors in the samples, and will approach the total number of samples in a signal if all samples of $|V|$ are completely independent.

3 Methodology

In this section, test rig specifications will first be presented followed by an overview of the operational conditions under which the measurements have been conducted. Then the PIV equipment, experimental PIV set-up and PIV specifications will be thoroughly discussed.

3.1 Test rig

All measurements were conducted at the Waterpower Laboratory at NTNU in a reduced scale (1:5.1) model of a prototype Francis turbine operating at Tokke power plant in Norway. The test rig was operated in a closed loop configuration, which can be viewed in Fig. 3.1. The green arrows indicate the fluid trajectory from the pump to the test section, while the red arrows show its return route to the pump. This configuration made it possible to keep the density of tracer particles constant during the different measurements.

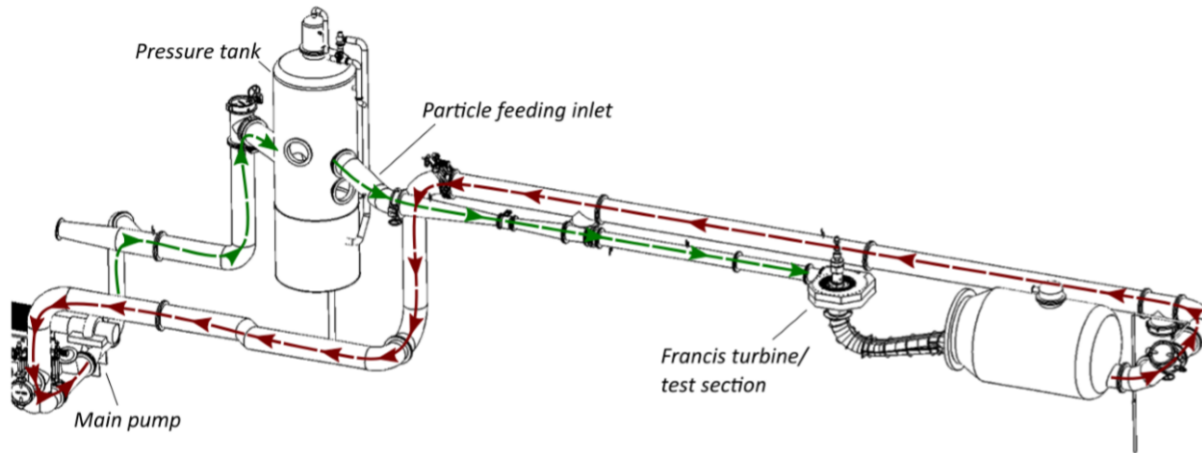


Figure 3.1: Closed loop configuration with arrows indicating fluid trajectory. Reproduced from [8].

A closer look at the test section is presented in Fig. 3.2, where the flow inlet and outlet is indicated by green and red arrows. The Francis turbine is equipped with 14 stay vanes in the volute, 28 guide vanes in the wicket gate and 30 runner blades, of which 15 are splitter blades. The guide vanes have an opening range from 0° to 14° , and the runner inlet and outlet diameters are 0.631 m and 0.349 m, respectively.

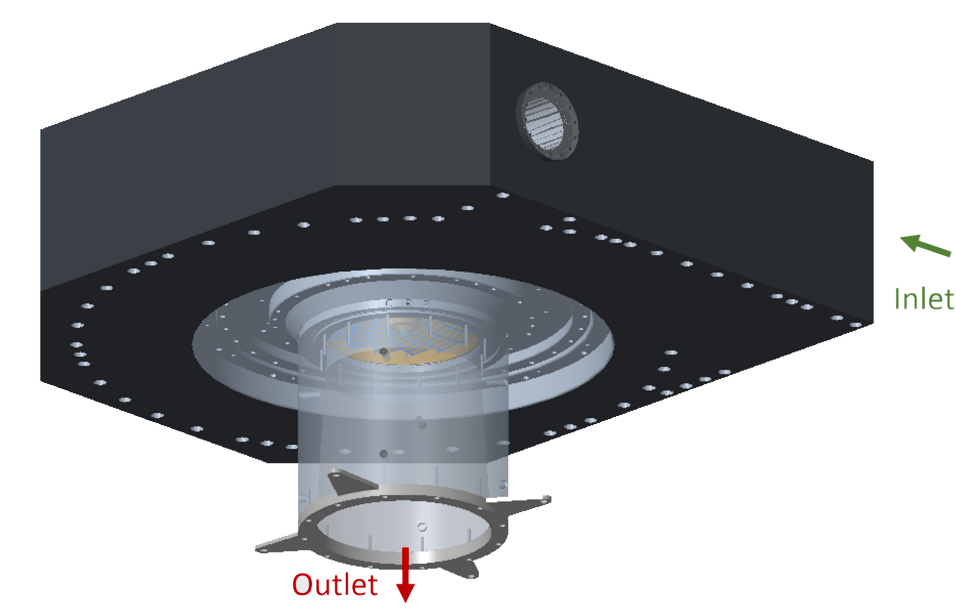


Figure 3.2: Test section with arrows indicating flow inlet and outlet.

The geometry of the guide vanes in the model turbine is shown in Fig 3.3. The chord length of the guide vane is 105 mm, the vertical height of the guide vane is 58.6 mm, and the trailing edge thickness at the indicated location is 0.64 mm. It can be observed that the guide vane is asymmetric, and the trailing edge is oblique.

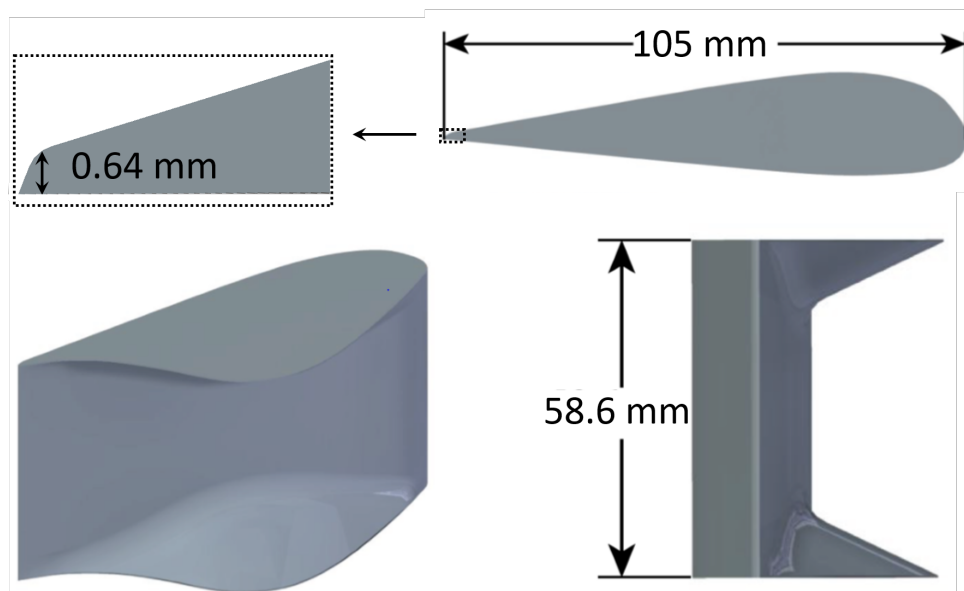


Figure 3.3: Geometry of guide vanes in model turbine. Reproduced and modified from [21].

3.2 Turbine operating parameters

Prior to the measurements, calibrations of the flow meter and of both inlet and differential pressure cells were performed. All the calibrations were executed in accordance with the Waterpower Laboratory calibration procedures [68, 69]. The flow meter was calibrated with a weighing tank, and the pressure cells were calibrated with dead weights. The combined relative uncertainty of the turbine parameters obtained from calibration can be found in Appendix C.

The measurements were executed at different operating conditions at PL, BEP, HL and FL, and are listed in Table 3.1 with corresponding names. The governing operating parameters are the guide vane angle, rotational speed of the runner and head value. Measurements were conducted with a constant rotational speed of the runner at 333 rpm, giving $n_{ED} = 0.18$, for a head of 12 m, and with five different guide vane angles, α_{GV} .

Table 3.1: Operating points.

Operating point	α_{GV}	\bar{Q}	Q_{ED}
PL1	4°	0.09 m ³ /s	0.07 [-]
PL2	6.7°	0.14 m ³ /s	0.11 [-]
BEP	10°	0.20 m ³ /s	0.15 [-]
HL	12.4°	0.24 m ³ /s	0.18 [-]
FL	14°	0.27 m ³ /s	0.20 [-]

The measurements were conducted in the following order:

14° → 12.4° → 10° → 6.7° → 4°

4° → 6.7° → 10° → 12.4° → 14°

14° → 12.4° → 10° → 6.7° → 4°

4° → 6.7° → 10° → 12.4° → 14°

The first and third line will from now on be referred to as ramp down measurements, while the second and fourth line will be referred to as ramp up measurements. As the procedure shows, two ramp down measurements and two ramp up measurements have been carried out for each guide vane opening. After each change of operating conditions, the test rig ran between 5-15 minutes to ensure that the system was stable before a measurement could be performed.

The head value, rotational speed, guide vane angle and flow rate were sampled and logged throughout the measurements. The arithmetic mean and relative standard deviation (RSD) of the logged turbine parameters have been calculated according to (2.18) and (2.19). The RSD is presented relative to the mean. Table 3.2 shows the arithmetic mean and RSD of the operating parameters for each operating point.

Table 3.2: Arithmetic mean and relative standard deviation of operating parameters.

(a) PL1			(b) PL2		
Parameter	Mean	RSD	Parameter	Mean	RSD
Guide vane angle	4.00°		Guide vane angle	6.72°	
Head	12.00 m	0.23 %	Head	12.00 m	0.18 %
Rotational speed	332.47 rpm	0.07 %	Rotational speed	333.16 rpm	0.16 %
Discharge	0.09 m ³ /s	0.15 %	Discharge	0.14 m ³ /s	0.13 %

(c) BEP			(d) OL		
Parameter	Mean	RSD	Parameter	Mean	RSD
Guide vane angle	10.02°		Guide vane angle	12.39°	
Head	11.97 m	0.37 %	Head	11.96 m	0.33 %
Rotational speed	333.30 rpm	0.16 %	Rotational speed	333.26 rpm	0.17 %
Discharge	0.20 m ³ /s	0.25 %	Discharge	0.24 m ³ /s	0.22 %

(e) FL		
Parameter	Mean	RSD
Guide vane angle	13.98°	
Head	11.95 m	0.33 %
Rotational speed	333.25 rpm	0.19 %
Discharge	0.27 m ³ /s	0.18 %

3.3 PIV equipment

The PIV equipment used in the measurements is listed in Table 3.3.

Table 3.3: PIV components.

Component	Name
Camera	Photron, FASTCAM Mini UX100
Lens	Tokina, AT-X Pro 100 mm, f/2.8
Laser	Litron, LDY300 PIV
Synchronization unit	LaVision PTU X
Timing stabilizer	LaVision LTS
Software	Davis 8.4, CW, Diode client PIV 1.0

The high-speed camera has a CMOS image sensor with a sensor resolution of 1280 x 1024 pixels. It is possible to attain an image rate of 2166 Hz at maximum resolution. The resolution can be reduced in order to allow for a higher frame rate. A lower resolution results in a smaller FOV.

The images were captured with a 100 mm macro lens with an f-number of f/2.8. The f-number is written as a fraction. A large aperture size, corresponding to a large f-number, captures more light than a smaller one. The aperture size also controls the depth of field. A larger aperture results in a shallow depth of field. Since the measurements are supposed to be in two dimensions, large f-numbers were preferred for a shallow plane depth.

The laser light is generated by the Litron LDY300 PIV dual cavity laser head which emits the laser light in an angle set by a series of mirrors and lenses. The light then goes through a mounting block and guiding arm, and gets transformed into a laser sheet by means of sheet optics. The laser head is connected to a laser power supply that has several functions. It controls the laser emission settings, delivers the required power to the laser head, and contains a laser cooling section that cools the laser diodes and the laser rods during operation. To mitigate the systematic timing errors of the lasers and to ensure a precise time separation between the two laser pulses, a LaVision laser timing stabilizer (LTS) is connected to the laser head. The LaVision programmable timing unit (PTU) serves the purpose of synchronizing the laser and the camera according to parameters set in the system software, and is connected to the LTS, camera and computer.

CW Diode Client 1.0 was used to remotely control the laser power supply, the diode current percentage, and the laser shutter. The calibration, recordings, and processing of the results were performed in DaVis 8.4 Software.

3.4 Experimental PIV set-up

A risk assessment was performed prior to the measurements, and the full report can be found in Appendix E. An overview of the experimental PIV set-up and components is shown in Fig. 3.4. Since the Litron LDY300 is a class 4 laser, and therefore hazardous to both eyes and skin, a black fabric tent surrounded the entire test section during measurements. The set-up including the tent is illustrated in Attachment A in Appendix E.

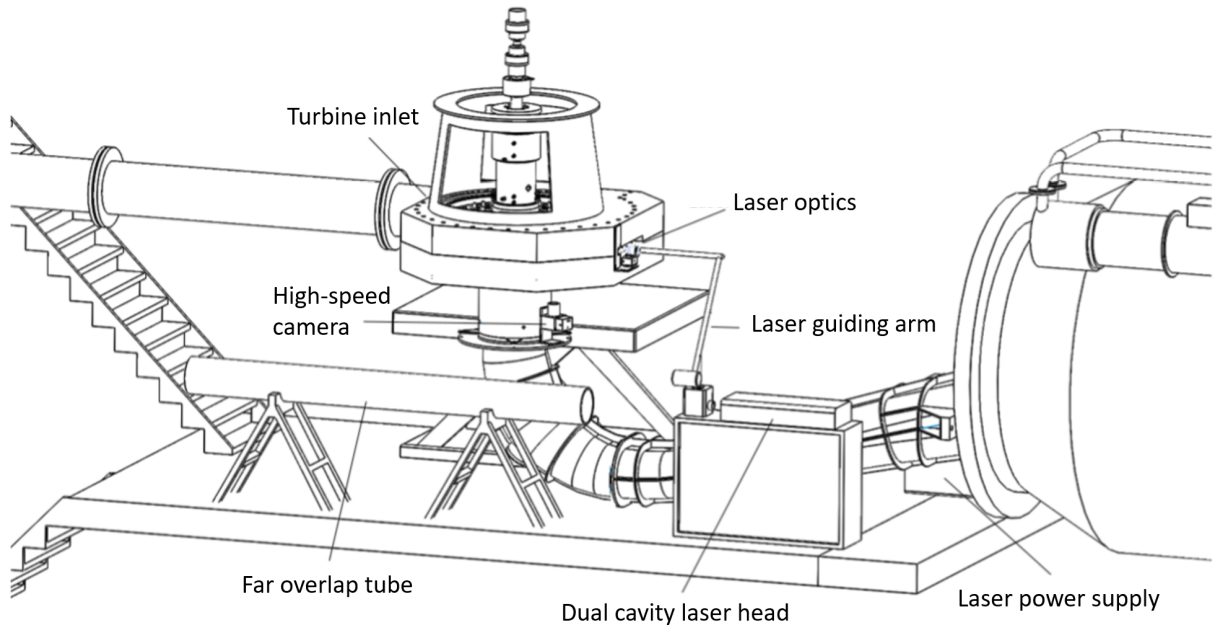
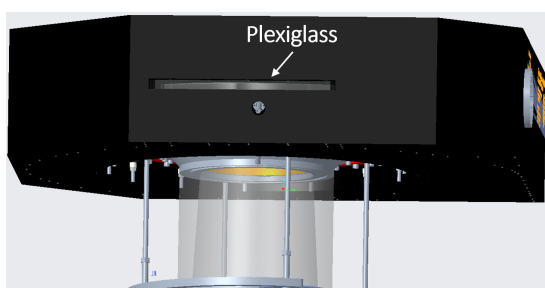
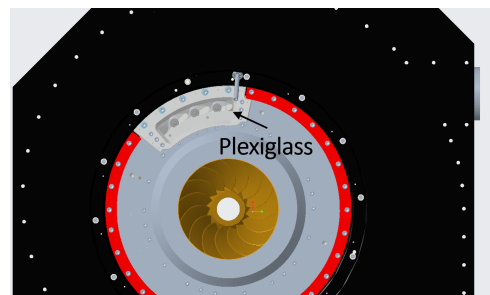


Figure 3.4: Test section with main PIV components. Reproduced and modified from [8].

Prior to the measurements, two tests were performed. One laser beam overlap test and one laser and camera synchronization test. The beam overlap was inspected both near field and far field by the use of the tube shown in Fig. 3.4. A detailed explanation of these tests can be found in Appendix B.



(a) Plexiglass window on the side of volute.

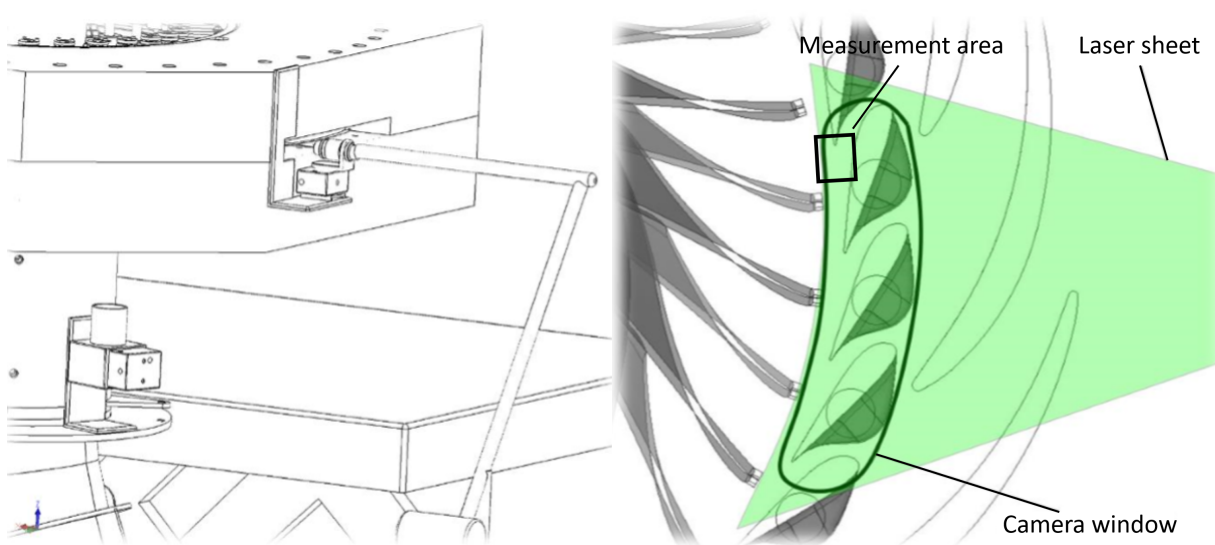


(b) Plexiglass window under volute.

Figure 3.5: Integrated plexiglass windows.

The measurement area in this thesis is the vaneless space, which is the narrow gap between the trailing edge of the guide vanes and the leading edge of the runner blades. In order to allow for PIV measurements of the flow in the vaneless space, some adjustments to the turbine have been made. Plexiglass windows had already been installed on the side and under the spiral casing to allow for the laser sheet and camera to illuminate and get optical access to the measurement area. Fig. 3.5 shows the integrated plexiglass windows in the spiral casing.

The camera was situated below the spiral casing and directed perpendicular to the laser sheet as depicted in Fig. 3.6a. In Fig. 3.6b, the measurement area and the laser sheet's path are shown. In order for the laser sheet to reach the measurement area, two of the stay vanes and three of the guide vanes were replaced with vanes partially made of plexiglass. The plexiglass guide vanes do not have the exact same shape as the original guide vanes made of steel. As the three guide vanes inside the camera window were made of plexiglass, the measurement area was located downstream of an original steel guide vane as shown in Fig. 3.6b. This prevented the different shape of the plexiglass guide vanes to have an impact on the velocity field in the measurement area.



(a) Camera and laser view from outside.

(b) Measurement region inside seen from above.

Figure 3.6: Close-up of measurement set-up. Reproduced and modified from [8].

The leading and trailing edges of the stay vanes and guide vanes acted as lenses spreading and concentrating the laser light. To limit this effect from happening in the FOV, the laser sheet was directed at an angle into the measurement area. As the aim was to measure in two dimensions, the laser sheet thickness needed to be as thin as possible. The focus length of the laser sheet was adjusted accordingly.

3.5 PIV calibration

Prior to the measurements, spatial calibration was performed by use of a calibration target. The calibration target contains a pattern of equispaced large dots, crosses, and small dots. The distances between two large dots, two crosses, and two small dots are 10 mm, 5 mm, and 2.5 mm, respectively. A picture of the calibration target is shown in Fig. 3.7.

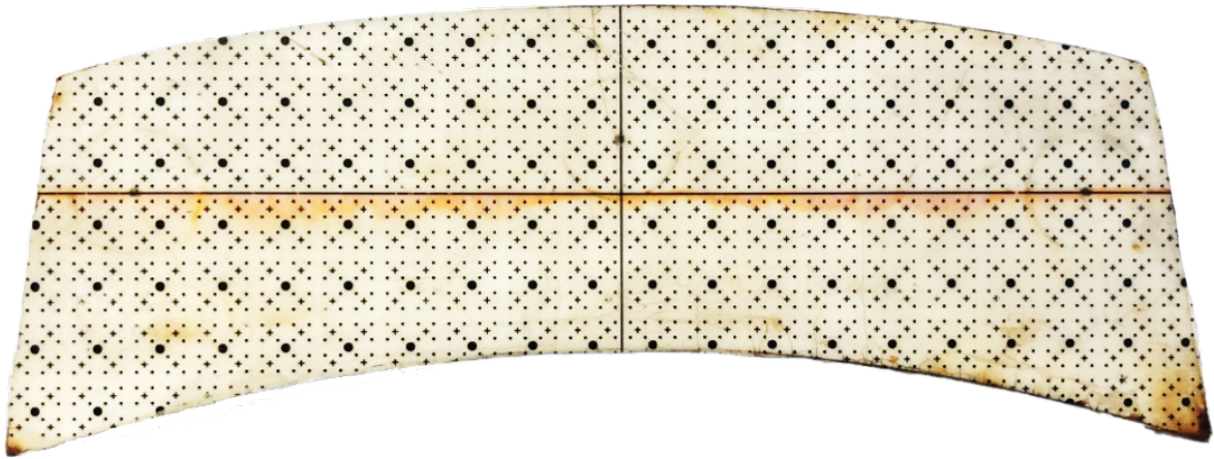


Figure 3.7: Calibration target.

In order for the calibration target to fit in the turbine, the three guide vanes inside the camera window previously shown in Fig. 3.6b had to be removed prior to calibration. The calibration target was located 28.3 mm above the bottom level of the guide vanes, which is in agreement with earlier measurements performed by Straume [8]. This is approximately at the mid-height of the guide vane, as shown in Fig. 3.3. The vertical height of the laser sheet was adjusted according to the bottom of the calibration plate.

To ascertain whether the position of the camera and laser sheet optics moved during measurements, two boxes with class 2 lasers were attached to both apparatuses. Each of the boxes contains four lasers pointing in different directions which this is illustrated in Fig. 3.8. The original position of the laser lights were marked on fixed surfaces and used as reference points. These marks were up to 3 m apart from the boxes, hence a small position change would be evident. Neither the camera nor the laser sheet optics noticeably changed positions during the measurements.

When the location of the calibration target was in compliance with earlier measurements, the test section was filled with water to best replicate the measurement conditions. The focus of the camera was adjusted with respect to the calibration target with the help of a functionality in DaVis 8.4 Software called focus quality.

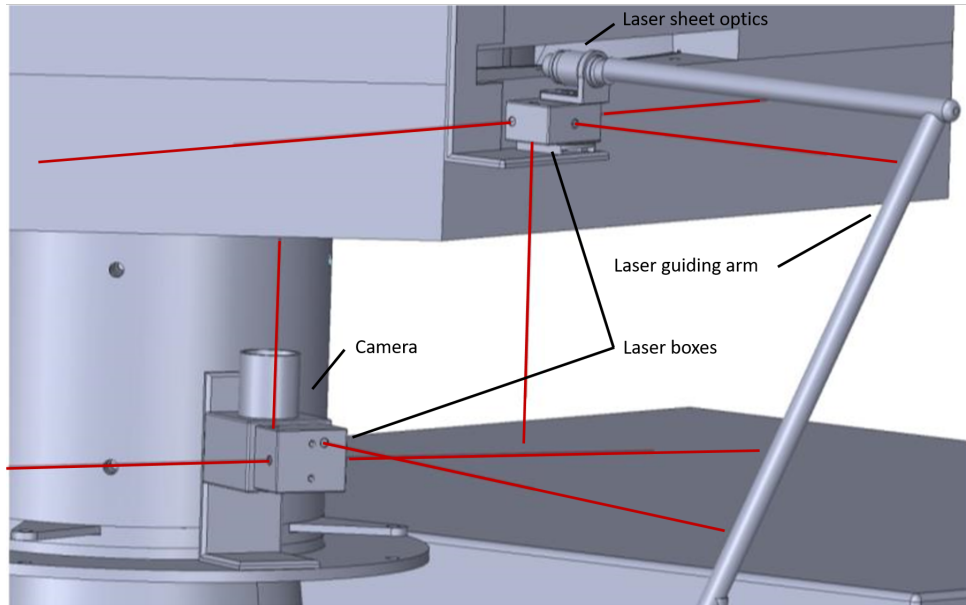


Figure 3.8: Laser boxes mounted on the camera and laser sheet optics. Reproduced and modified from [8].

The 100 mm objective was calibrated for two different resolutions, 1280 x 1024 pixels and 1280 x 600 pixels. The local coordinate system, and the sizes of the two different FOV are shown in Fig. 3.9. The reader is referred to Appendix A for an overview of the global coordinates of the 1280 x 1024 FOV.

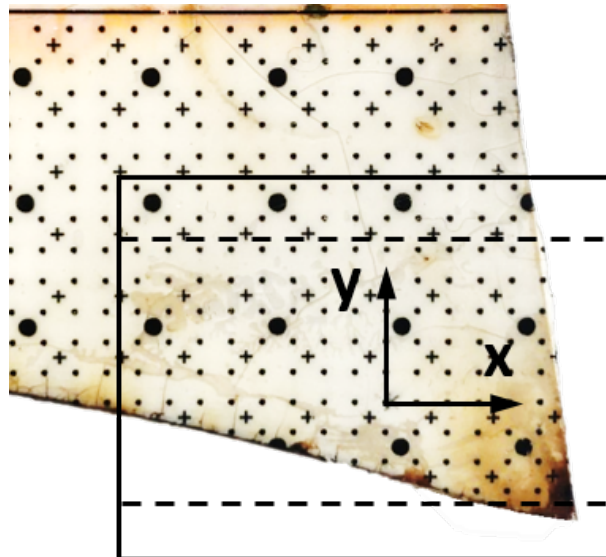


Figure 3.9: Coordinate system shown on the calibration target. The solid and dashed rectangles are the two different FOV sizes of 1280 x 1024 pixels and 1280 x 600 pixels, respectively.

The calibration procedure was performed in DaVis 8.4 Software. In the calibration the smaller dots were used, which satisfies the condition of having at least 20-30 marks in the FOV [57].

Three marks on the calibration target were defined by the user, followed by a mark search performed by the software. Then, 3rd order polynomial functions were fitted to the marks by the software to produce a corrected image. Fig. 3.10 shows the pre-calibrated image in unit pixels and the corrected image in unit millimetres.

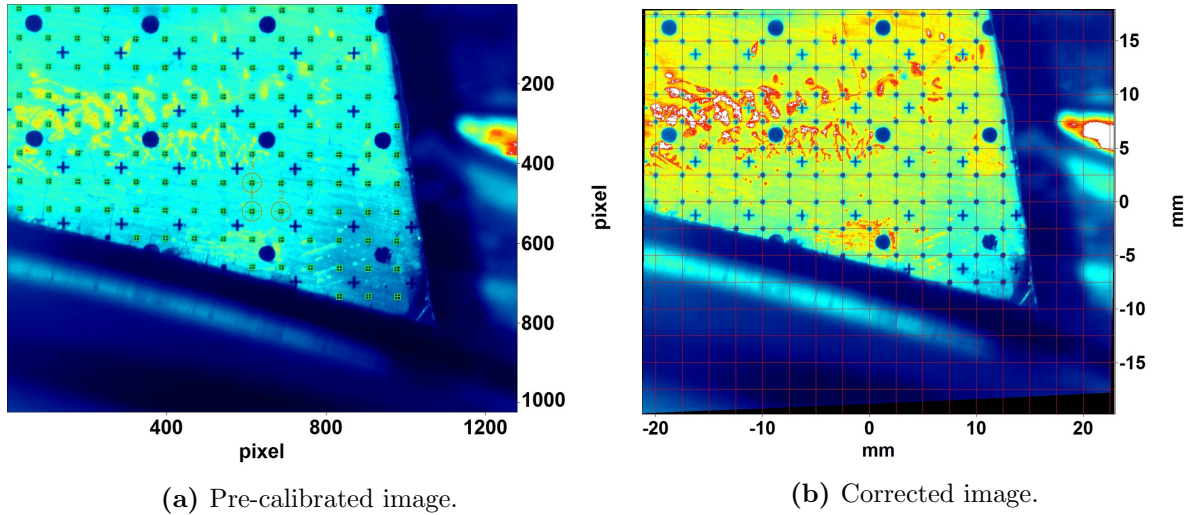


Figure 3.10: Calibration target with a 1280 x 1024 pixels resolution FOV.

As can be observed in the images in Fig. 3.10, the calibration target did not cover the entire FOV. As a result of this, there will be a higher uncertainty related to the vectors in the uncovered region. The image scaling calibration RMS error of the 3rd order polynomial fit was approximately 0.51 pixels for the calibration. This is considered good as it is small in comparison to the pixel resolution of the camera in use. If the value had been above 1 pixel, it would be considered questionable [57].

After the measurements, a post-calibration was executed. The scale factor from the pre-calibration was compared to the scale factor in the post-calibration. For the 1280 x 1024 pixels FOV, the scale factor in the pre-calibration was approximately 29.20 pixel/mm, while the scale factor in the post-calibration was 29.17 pixel/mm. This deviation may produce a small systematic error in the velocity field, but as it was so low this was neglected.

During post-calibration, an attempt to quantify the vertical height uncertainty of the measurement plane was made. By carefully adjusting the vertical height of the calibration plane according to the laser sheet and focus of the camera, the post-measurement vertical height could be measured. The resulting vertical height uncertainty of the measurement plane was estimated to be 28.3 ± 1 mm.

3.6 PIV recording parameters

Table 3.4: PIV recording parameters.

Resolution	1280 x 1024 pixels	1280 x 600 pixels
Field of view	43.8 mm x 35.1 mm	43.8 mm x 20.5 mm
Image rate	0.2 kHz	4.166 kHz
Duration of recordings	21.84 s	1.79 s
Sample size	4367	7453
Initial IA size	64 x 64 pixels with 50% overlap	
Final IA size	24 x 24 pixels with 50% overlap	
Time delay between pulses	15 μ s - 17 μ s	
Tracer particle type	Hollow glass spheres	
Mean tracer particle diameter	15.5 μ m	
Tracer particle density	1.1 g/cm ³	

The particles were injected into the water loop at the inlet pipe. A valve was opened for a selected time interval in order to add the particles into the closed loop of water. This was done repeatedly, and the seeding density was measured by recording images during this procedure until the seeding density was considered satisfactory. A combination of hollow glass spheres with diameters of 11 μ m and 20 μ m were injected into the water, making the average tracer particle diameter roughly 15.5 μ m. The tracer particle density was 1.1 g/cm³, nearly fulfilling the buoyancy criterion since the water had a density of approximately 1 g/cm³ [48, p. 33-51].

A final laser beam overlap test was performed in DaVis 8.4 after the tracer particles had been added to the flow. By recording an image pair with a small pulse separation of 6 μ s of a nearly still fluid, a beam overlap of 0.98 was achieved where a value of 1 indicates two identical images [53]. This was found acceptable.

Images were recorded at two different FOVs by the 100 mm objective. One at a high resolution of 1280 x 1024 pixels, and one at a lower resolution of 1280 x 600 pixels. An overview of the PIV recording parameters is presented in Table 3.4. With an obtained scale factor of 29.20 pixel/mm from the calibration, the resulting sizes of the areas were approximately 43.8 mm x 35.1 mm and 43.8 mm x 20.5 mm. Fig. 3.11 shows the different FOVs in the measurement plane.

The image rate for the high resolution recordings was 0.2 kHz, which was the lowest attainable image rate for that resolution in the software. In order to obtain an accurate steady state velocity field from the high resolution FOV, these recordings lasted as long as the equipment allowed. The image sampling lasted for about 21.84 seconds, giving 4367 images per recording. This time period corresponds to about 3600 runner blade passings or 120 runner rotations. Time-averaged

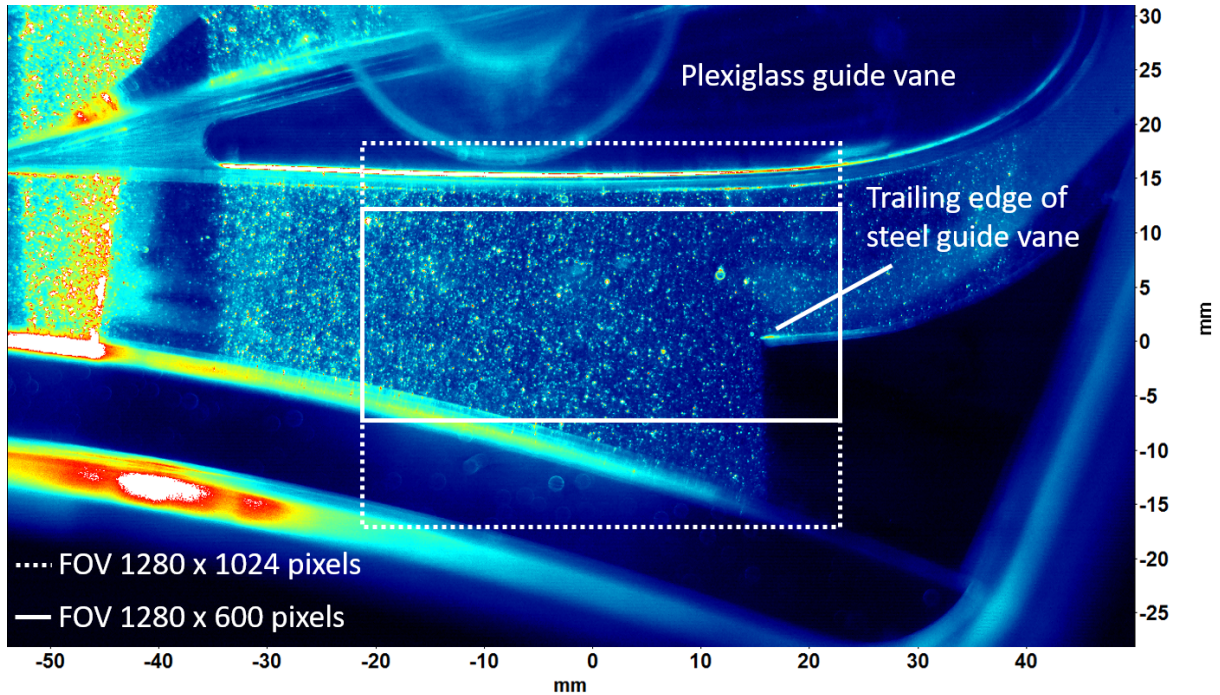


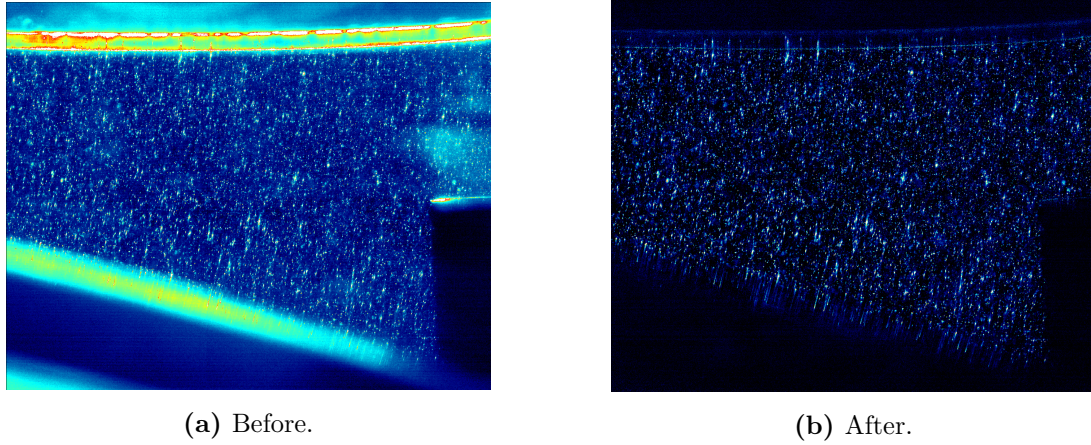
Figure 3.11: The 1280 x 1024 pixels FOV and 1280 x 600 pixels FOV in the measurement plane with the 50 mm objective.

vector fields were computed from the high resolution recordings. Velocity profiles were extracted from these fields with the aim of relating the velocity development to the theory. In addition, velocity profiles from two different measurements at the same operating point were compared in order to quantify the difference in the steady state field.

The low resolution recordings had an image rate of 4.166 kHz, and lasted for approximately 1.79 seconds. This corresponds to roughly 300 runner blade passings or 10 runner rotations. 7453 images were obtained from each of these recordings. This image rate was deemed necessary to capture the vortex shedding frequency according to Nyquist's sampling theorem [56]. The RSI and vortex shedding frequencies were analyzed through spectral analysis of the low resolution recordings. The vertical velocity component at points near the runner and in the wake were analyzed to obtain power spectra. The PL1 recordings for the low resolution FOV were not evaluated because of spurious measurement errors.

The time delay between the laser pulses was chosen with the aim of obtaining a particle movement of about 5-6 pixels between each image frame. It was varied between 15 μ s and 17 μ s depending on the operating points. The operating points with the smallest guide vane openings had the shortest time delays, and the largest guide vane openings had the longest time delays.

Prior to the processing, a time filter aiming to eliminate background noise was added to the recorded images in DaVis 8.4. The filter subtracts the minimum intensity from the source, with



(a) Before.

(b) After.

Figure 3.12: Images before and after applied time filter.

a filter length of 5 [57]. Fig. 3.12 shows the image prior to and after this filter was applied. To prevent intensity fluctuations in the background due to reflections, a high pass filter called subtraction of a sliding background was applied with a scale length of 12 pixels [53]. As the FOV contains areas without particles, a geometric mask was applied to the PIV algorithm. The geometric mask is illustrated by the white polygon shown in Fig. 3.13.

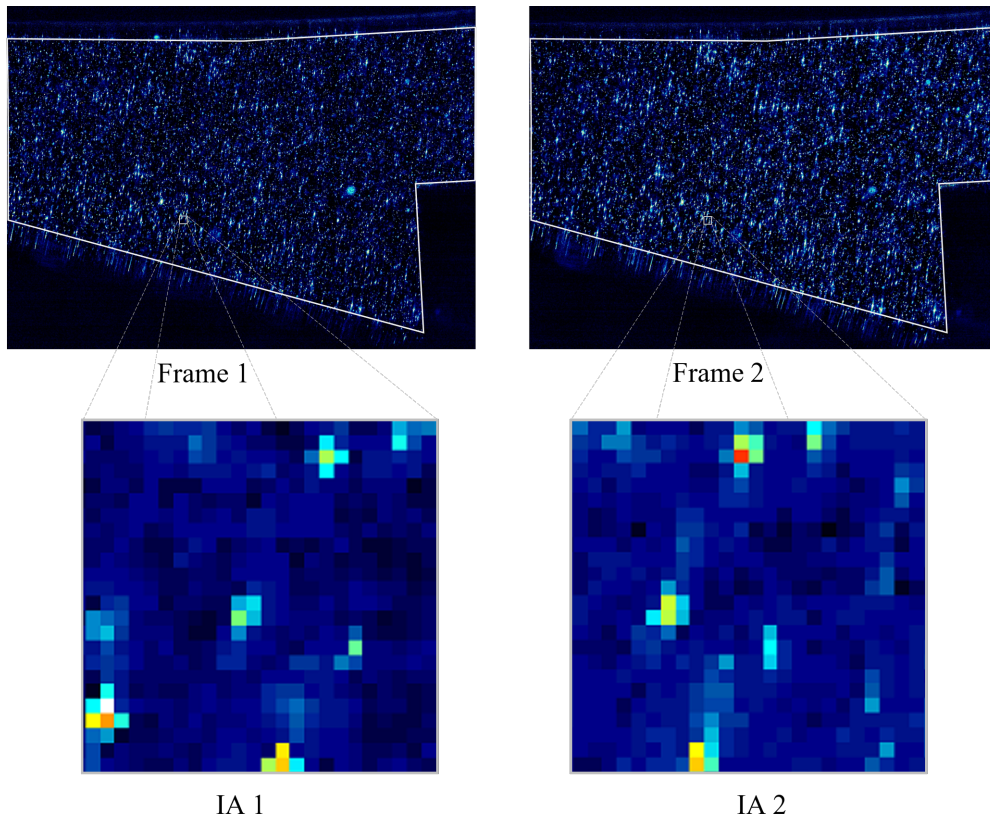


Figure 3.13: Illustration of two consecutive frames and final IAs of size 24 x 24 pixels.

Cross-correlation of the image frames was done with a multi-pass approach with a decreasing IA size. The initial and final IA sizes were 64 x 64 pixels and 24 x 24 pixels, respectively. Both with a 50 % overlap and 2 passes each. The initial IA size was chosen according to the one-quarter rule, and the rule stating it should be at least 10 particles in each initial IA [49, 55, 59, 60]. Several different final IA sizes were investigated, and are shown in Fig. 3.14. With the use of multi-pass evaluation, the final IA only needs a seeding density of at least 5 [48, p. 203-229]. Fig. 3.13 shows the seeding density for a 24 x 24 pixel IA. As can be concluded from this figure, the final interrogation size could not be smaller than 24 x 24 pixels. Because of this a final IA size of 24 x 24 pixels was chosen in order to obtain the highest possible resolution of the vector field.

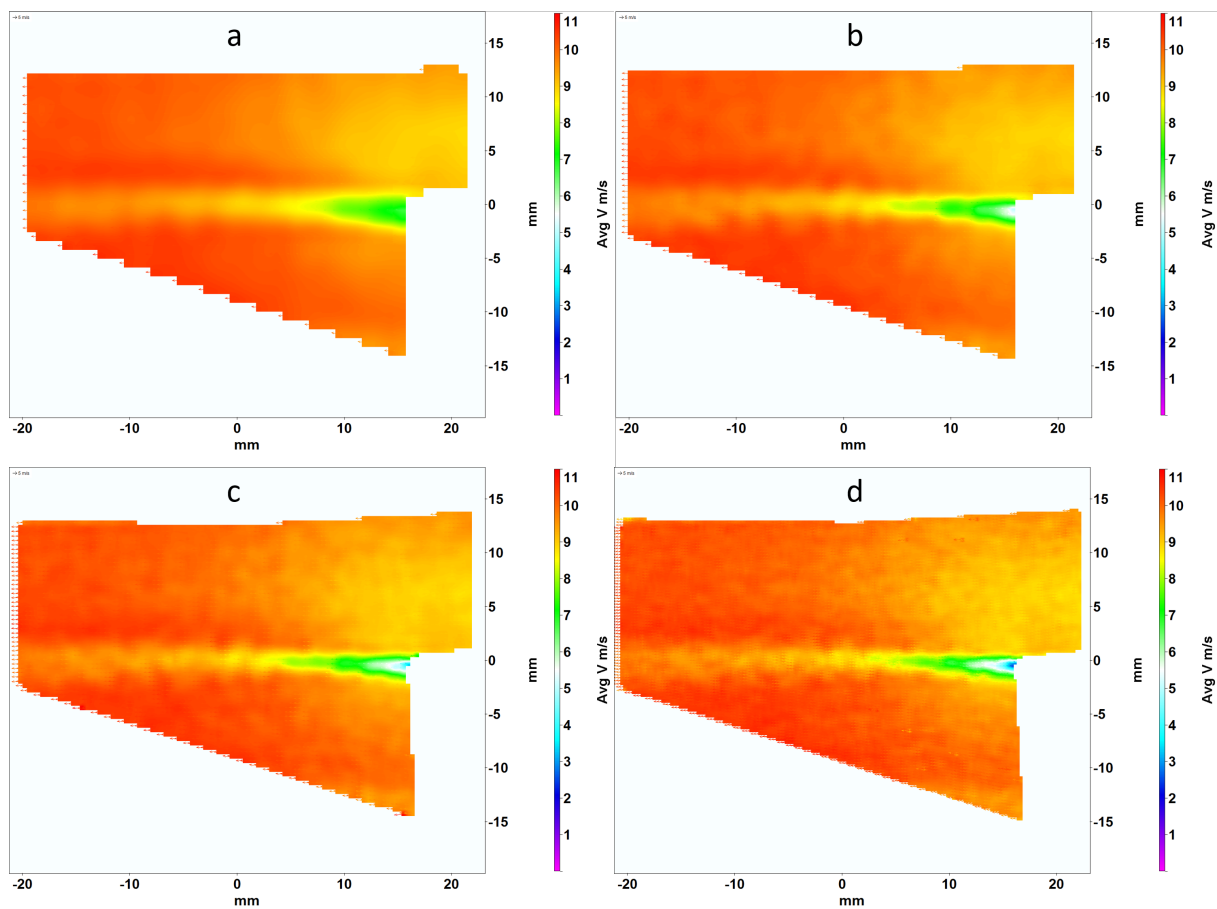


Figure 3.14: Average velocity field at BEP for final IA of size, a: 48 x 48 pixels, b: 32 x 32 pixels, c: 24 x 24 pixels, d: 16 x 16 pixels.

The amount of spurious vectors was found to be acceptable for the chosen interrogation area size. Different numbers of passes were tried during processing, but no observable difference was found by increasing the number of passes past 2. A round Gaussian weighting function was used on the final IA since this is shown to generally improve the accuracy in the vector field computation [53].

In the vector post-processing, a median filter was applied to the PIV algorithm. The method used was adopted from Westerweel [62] which is described in 2.3.6. The factor f in (2.16) and (2.17) was specified as 2, making the allowable range ± 2 times the standard deviation of the neighbours. If a vector is outside this range it is discarded. Another vector is reinserted if one of the other three highest correlation peaks fits into the range.

3.7 PIV measurement uncertainty

The uncertainty of the vector fields obtained from PIV measurements can be quantified by DaVis 8.4. In the software it is possible to obtain the probability density function of a vector field. DaVis 8.4 computes a histogram of the decimal places of the velocity components and a peak lock value. These calculations serve as an indicator of the peak locking effects. Fig. 3.15 shows a histogram representation of the probability density function of the integer modulus of the x- and y-velocity vectors from a sample vector field at BEP. No strong peak locking effect is observed in this histogram. The peak lock value for the other measurements was also inspected, and the maximum value found was 0.08. Hence the degree of peak locking was satisfying for all measurements [66], as expected as the average particle size is well above 1 pixel.

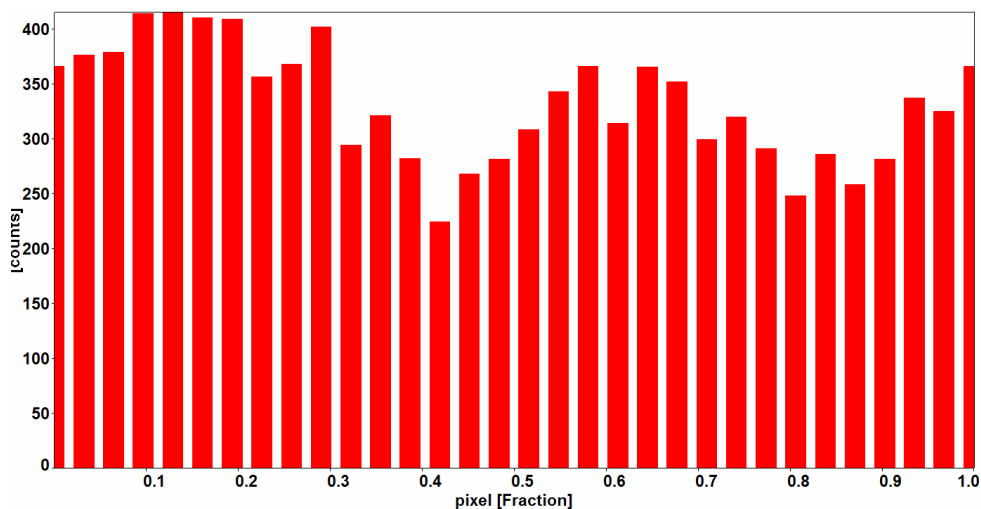


Figure 3.15: Histogram representation of the probability density function of an instantaneous velocity field.

DaVis 8.4 provides a method to quantify the systematic uncertainty from correlation statistics. Fig. 3.16 illustrates the uncertainty estimate of the absolute velocity for an instantaneous velocity field in accordance with the method of Wieneke [67]. The instantaneous velocity field is obtained from a ramp up measurement at BEP with an average absolute velocity of 9.8 m/s. The maximum uncertainty is in the order of 4.5% relative to the average velocity in the field, but it is generally less than 2%. The uncertainty of the other measurements with different guide vane angles, yielded an uncertainty of approximately the same order.

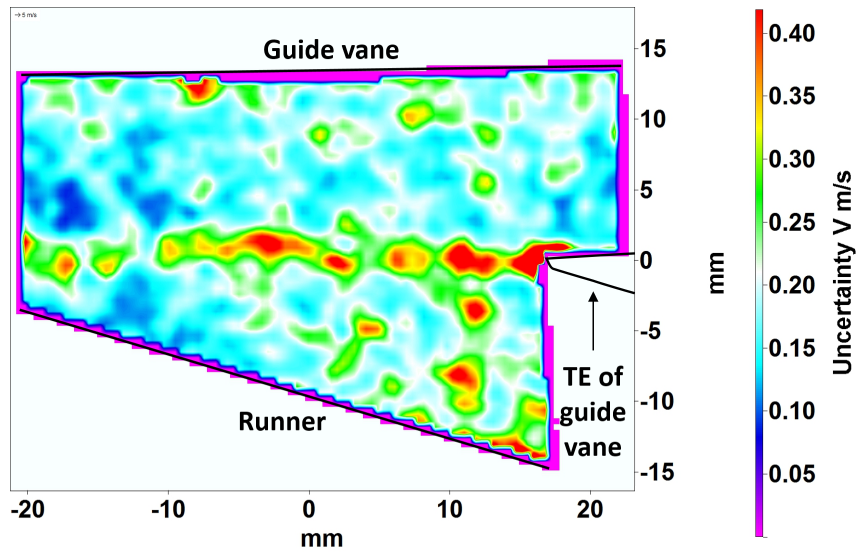


Figure 3.16: Cross correlation uncertainty of the absolute velocity for an instantaneous velocity field.

4 Results and discussion

In this section, results are presented and discussed starting with the time-averaged velocity fields and velocity profiles, followed by RSI frequency, and ending with vortex shedding frequency.

4.1 Time-averaged velocity fields

Time-averaged velocity fields are obtained from the 1280 x 1024 pixels recordings with an image rate of 0.2 kHz for a ramp up measurement. The recording sequence lasted for approximately 22 seconds giving 4367 samplings from which the average velocity field is calculated. The velocity component presented is the absolute velocity. The reader is referred to Fig. 3.11 for an illustration of the FOV location, which shows what the lines represent in the figures on the next page. The velocity is differently scaled by means of color for each operating point.

Fig. 4.1 presents time-averaged absolute velocity fields obtained from five different operating points. The pressure side is the upper side of the guide vane, and the suction side is the lower one. Downstream of the guide vane TE there is an elongated zone with lower velocity compared to the surroundings. This is the wake, and in line with wake theory the largest velocity deficit can be found right behind the guide vane TE. As expected from the wake theory presented in 2.2.2, the velocity in the wake is observed to increase with an increasing distance from the TE of the guide vane.

The wake path is dependent on the guide vane angle. At PL1, for which the velocity field is depicted in Fig. 4.1a, the wake is directed slightly upwards. Fig. 4.1b-4.1d show that the wakes propagate more and more downward with a larger guide vane angle. For the guide vane opening of 14 degrees, illustrated in Fig. 4.1e, the wake and the runner interaction point is located at about (-15, -5) in the FOV. In agreement with previously presented theory regarding RSI in 2.2.6, the interaction point changes with different guide vane openings. For the larger guide vane openings, such as 12.4° and 14°, the distance between the guide vane TE and runner interaction point is considerably smaller than for the 4° guide vane angle. This indicates that the wake effects are felt stronger in the runner for the larger guide vane openings.

By comparing the PIV results to the numerical simulations [10] presented in 1.3 Previous work, there are similar velocity ranges for all the different operating points. However, the simulation results seem to slightly underpredict the velocity deficit in the far-wake compared to the PIV measurements.

Regarding boundary layer separation, the width of the wake near the trailing edges might suggest a separation slightly upstream of the tip at the suction side for all operating points. The same separation trend has been illustrated both in experimental and numerical studies for the same Francis turbine performed by Straume [8] and Trivedi et al. [10]. As stated earlier in 2.2.2, the separation point will be dependent on the angle of attack. It is however difficult to determine

the exact position of the separation as the trailing edge of the guide vane made of steel obstructs the laser light, and no velocity field is computed below the trailing edge.

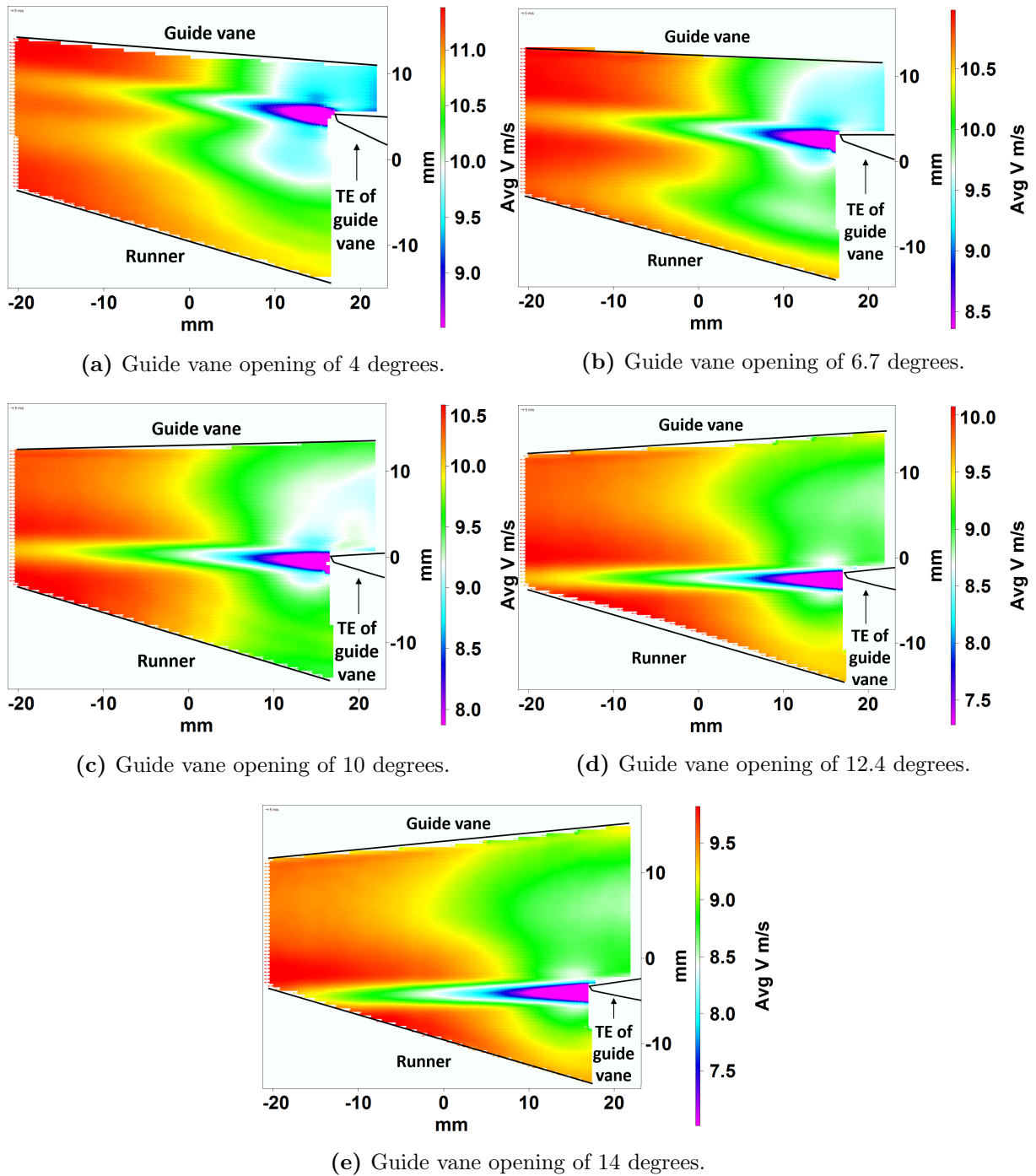


Figure 4.1: Time-averaged absolute velocity fields.

Computed from (2.20), the uncertainty of the time-averaged absolute velocity field in Fig. 4.1c is given in Fig. 4.2. As can be observed, the largest uncertainty is in the wake. This is expected as the velocity fluctuation is the largest in this area.

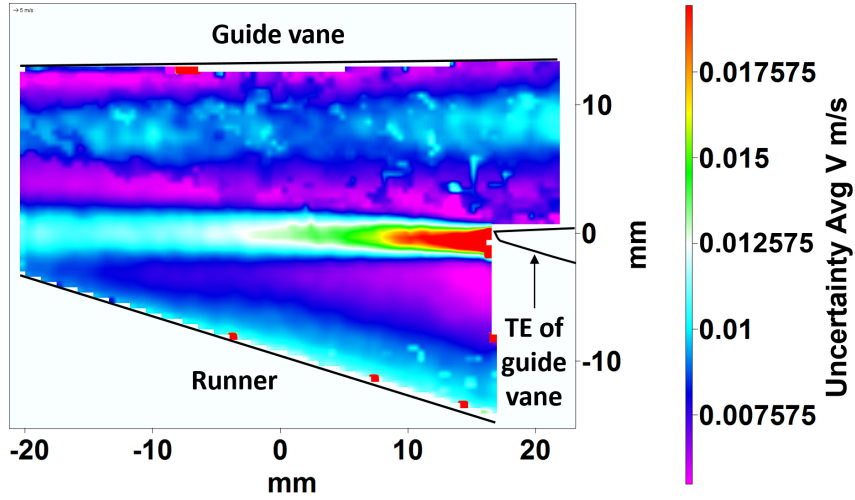


Figure 4.2: Uncertainty of the time-averaged absolute velocity field at BEP.

Table 4.1 shows the average absolute velocity component for each field in Fig. 4.1. The average velocities are calculated from four measurement series, two ramp up and two ramp down measurements. The discharge is the highest for the largest guide vane angles, hence the radial velocity upstream of the guide vane is the highest for these angles. However, the average velocity in the FOV and the guide vane angle are negatively correlated. This reveals that the flow has a higher acceleration through the guide vane passage for smaller guide vane angles than for larger ones. This is in agreement with the numerical simulation results from Trivedi et al. [10] previously presented in 1.3 Previous work.

Table 4.1: FOV average absolute velocity for each operating point.

Guide vane angle	Average velocity
4°	10.55 m/s
6.7°	10.25 m/s
10°	9.81 m/s
12.4°	9.42 m/s
14°	9.12 m/s

4.2 Time-averaged velocity profiles

Velocity profiles have been extracted at BEP from Fig. 4.1c, along the dashed lines visible in Fig. 4.3. The dashed lines correspond to x-locations 0, 5, 10 and 15.

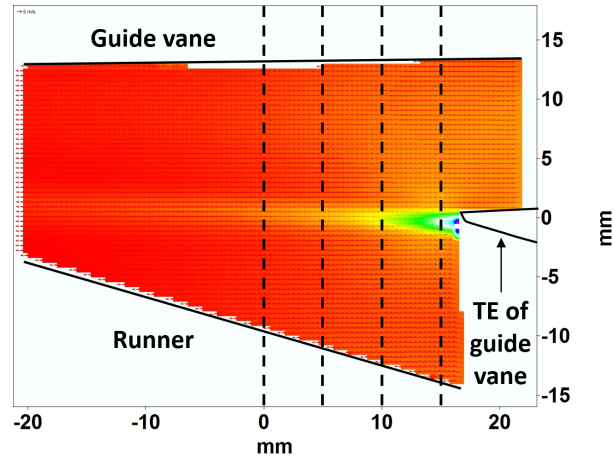


Figure 4.3: x-positions of velocity profiles indicated by dashed black lines.

The velocity profiles in Fig. 4.4 illustrate the expected trend of an increased velocity deficit near the trailing edge. Along $x = 15$, the largest velocity deficit is at a y-position of approximately 0. The wake centre shifts slightly upwards as the flow travels downstream. Regarding the wake width, it appears to have increased a bit from $x = 15$ to $x = 0$.

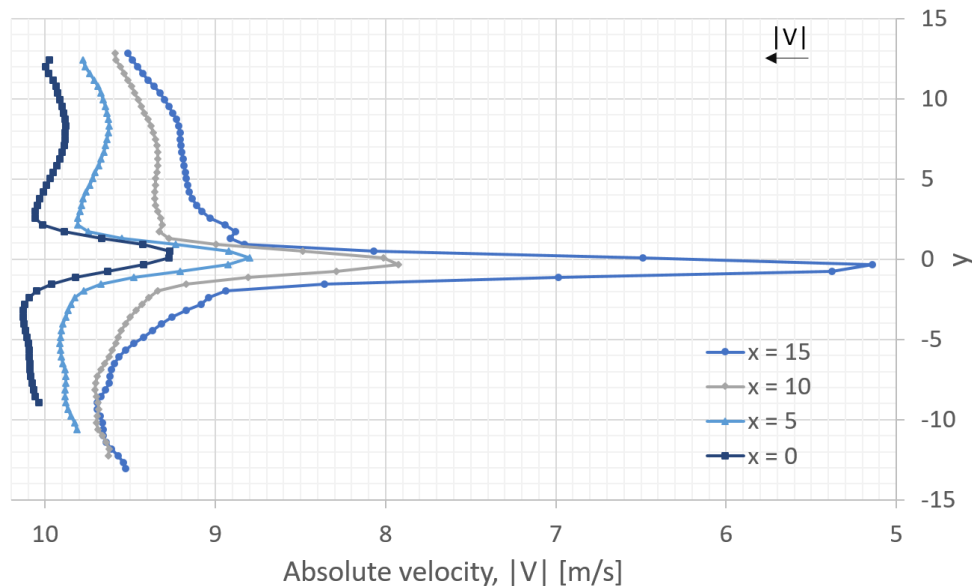


Figure 4.4: Velocity profiles along four lines in the wake for a ramp up measurement at BEP.

The velocity profiles at $x = 0$ and $x = 15$ have been plotted in Fig. 4.5 for two different ramp up measurements at BEP with the aim of observing the deviation between each field. The first measurement is denoted Set 1, and the second one is denoted Set 2. At $x = 15$, the velocity difference between the two sets is slightly higher than for one at $x = 0$. The maximum deviation between the two sets is 0.074 m/s, which gives a deviation of 0.81 % relative to the absolute velocity at that point. This gives an indication of how well the sampling with a duration of 22 seconds captures the steady state field. Further inspection of the deviation between different measurements could have been of interest, but due to time constraints this was not done.

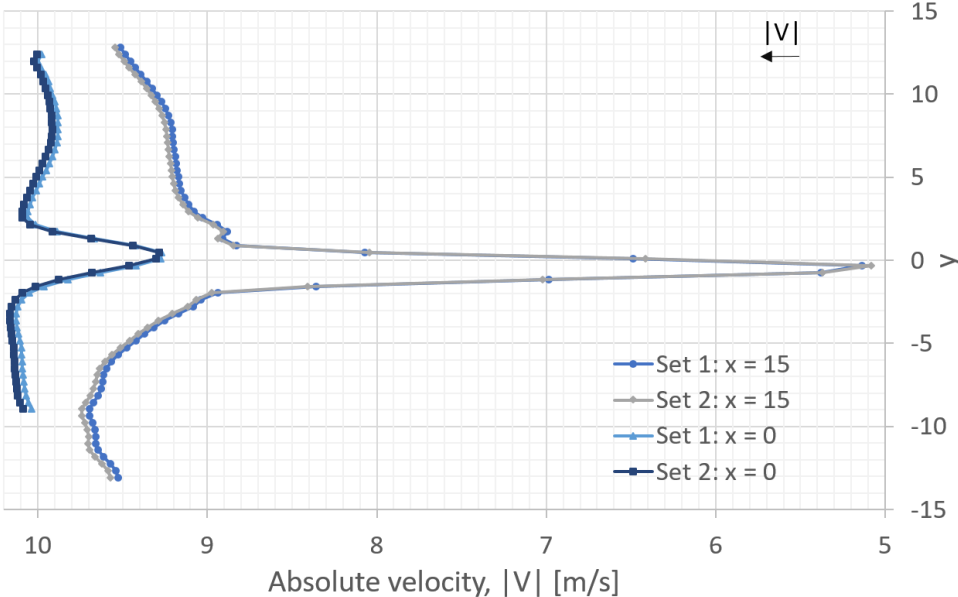


Figure 4.5: Velocity profiles along two lines in the wake for two ramp up measurements at BEP.

4.3 RSI

The following results are obtained from the 1280 x 600 pixels recordings with an image rate of 4.166 kHz. A power spectrum analysis was carried out on the cross flow velocity aiming to find the dominating frequencies. A power spectrum was obtained in the position indicated by Pos. 1 in Fig. 4.6.

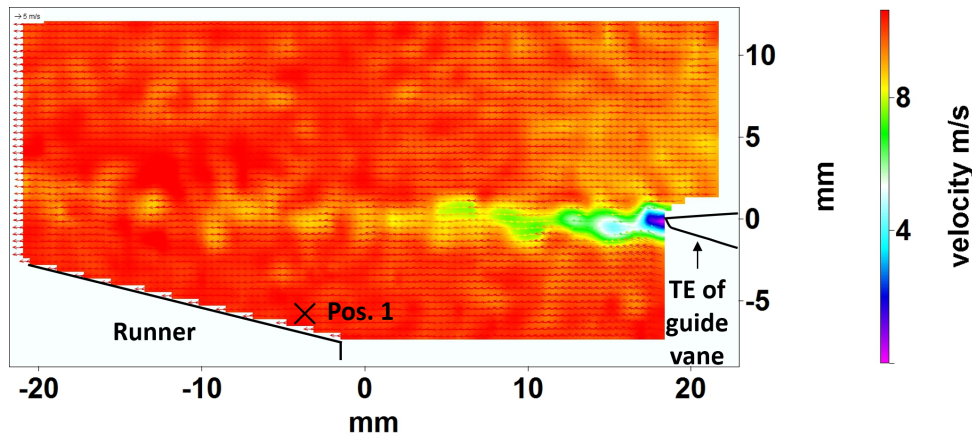


Figure 4.6: Pos. 1 indicated in the 1280 x 600 FOV.

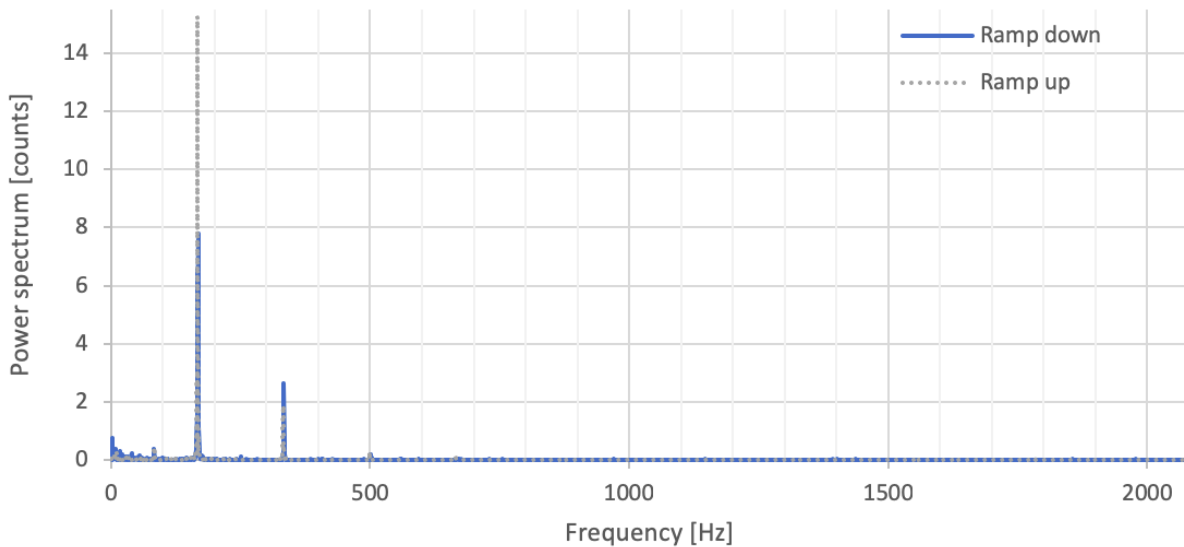


Figure 4.7: Power spectrum obtained for cross flow velocity component at Pos. 1 at BEP.

The power spectra for a ramp up and ramp down measurement at BEP are given in Fig. 4.7. The dominating frequency is about 166.5 Hz for both measurements, which coincides with the runner blade passing frequency calculated from (2.12) for a rotational speed of 333 rpm. The second harmonic frequency is also present as a peak in the figure at about 333 Hz. These findings are in line with the results of Straume [8]. Power spectra from other points in the FOV were also investigated. The runner blade passing frequency was dominating near the runner inlet,

but it gradually diminished with an increased distance from the runner inlet.

Although not presented, the power spectra from Pos. 1 for all the different guide vane openings were computed. Each operating point was measured four times, two in ramp up and two in ramp down, giving in total 20 measurement series. The maximum deviation from the theoretical runner blade passing frequency was 2 Hz. A small variation in the runner blade passing frequency was expected as the runner rotational speed varied slightly during each recording.

From the velocity fields in Fig. 4.1, the wake interaction part of the RSI appears to be the largest for the highest guide vane openings. This is in line with the theory presented in the 2.2.6 RSI.

4.4 Vortex shedding

The following results are obtained from the 1280 x 600 pixels recordings with an image rate of 4166 Hz. Each operating point except PL1, has been measured four times, giving in total 16 measurement sets. Each measurement set contains 7453 images.

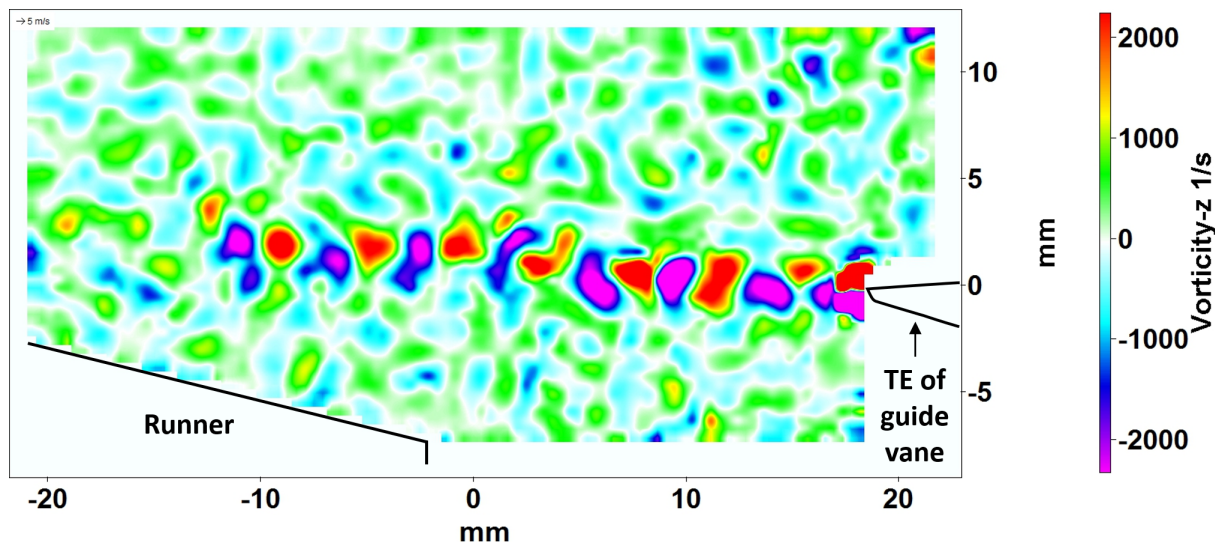


Figure 4.8: Instantaneous vector field coloured according to vorticity at BEP.

Fig. 4.8 shows an instantaneous vector field coloured according to vorticity for a guide vane opening of 10° . The vorticity is calculated from (2.4) in the xy -plane. A distinct von Kármán vortex street behind the guide vane trailing edge can be observed in the vorticity field. Though turbulent, vortices of opposite rotation are clearly formed. Also observable is the two opposite re-circulation zones right downstream of the trailing edge, indicating a dead water zone [17, 19, 20]. Over the course of the recordings, the vortex street appears not to be regular, but rather with deforming vortices. In the instantaneous field at BEP depicted in Fig. 4.8, the dead water zone seems to end at a x -location of about 18.

It is important to note that the water flows from right to left which results in negative horizontal velocity components in the defined axis system. The figure shows that the vortices initiated from the upper surface have positive vorticity values, and the vortices originating from the lower surface have negative values. This is in agreement with vorticity theory presented earlier in 2.2.3 as $-\frac{\partial v_x}{\partial y}$ yields a positive value adjacent to the upper surface, and a negative value close to the lower surface.

To capture the vortex shedding frequency, the vertical velocity component at a point in the wake can be used to compute a power spectrum. Careful considerations regarding the positions of the points are important. The chosen position should experience fluctuations in the vertical component of the velocity. As a result, the vorticity field for each guide vane angle should be

separately assessed when deciding the location of the point.

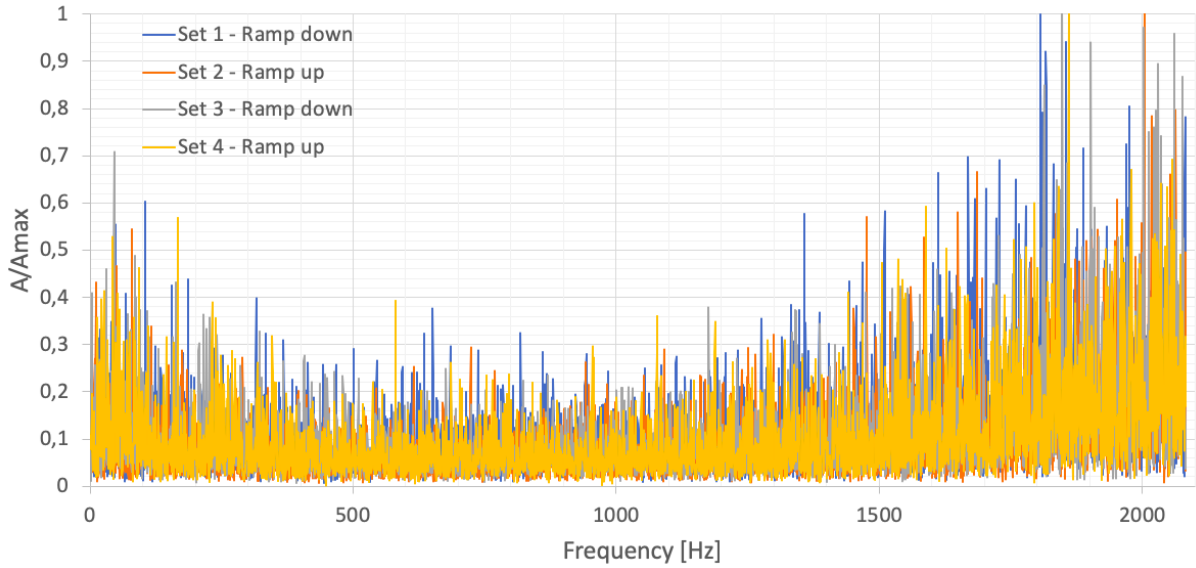


Figure 4.9: Power spectrum obtained from cross flow velocity component at position (15, 0) at BEP.

Fig. 4.9 shows the power spectrum obtained from the vertical velocity component at position (15, 0) at BEP from four measurement series. Amplitudes are normalized with respect to each power spectrum's maximum amplitude for the four different measurement sets. As the vortex street in the FOV is observed to be disorganized and change during the sampling time, the power spectrum is expected to show a range of peaks [35–37]. The spectrum for Set 1 shows a distribution similar to a normal distribution of frequency peaks. This is in agreement with earlier measurements for an isolated hydrofoil in lock-off condition performed by Sagmo et al. [38]. Thus, the broad range of frequency peaks indicates that there are no present lock-in effects. For Set 2 and 3, high peaks can be observed in the order of 2000 Hz. This demonstrates that a higher image rate, which allows for higher frequencies to be captured according to the Nyquist theorem, could be beneficial for this case.

The dominating frequencies for sets 1, 2, 3 and 4 are 1807 Hz, 2004 Hz, 1848 Hz and 1860 Hz respectively. In order to quantify the vortex shedding frequency, the mean is calculated from the dominating peak in each of the four measurement sets. In the case of BEP shown in Fig. 4.9, the calculated mean vortex shedding frequency is 1880 Hz. This frequency is within the range of 1800-2000 Hz found by Straume at BEP [8]. In an in-house measurement report by Sagmo [9], the vortex shedding frequency at BEP was estimated to 1850 Hz, which is relatively close to the mean vortex shedding frequency calculated here. However, it is important to stress that several other methods to quantify the vortex shedding could give more accurate shedding frequencies.

The aforementioned procedure for quantifying the vortex shedding frequency has been carried out for all the operating points, and the resulting shedding frequencies are shown in Table 4.2. The power spectra for the other guide vane openings can be found in Appendix D. As can be seen from the table, the vortex shedding frequency tends to decrease for higher guide vane openings. This indicates that the vortex shedding frequency and the guide vane downstream velocity are positively correlated.

Table 4.2: Mean vortex shedding frequency for different operating points.

Operating point	Vortex shedding frequency
PL2	1977 Hz
BEP	1880 Hz
HL	1818 Hz
FL	1803 Hz

The vortex shedding frequencies for the different guide vane openings have been estimated by Brekke’s formula (2.11) and are shown in Table 4.3. The assumed free stream velocity is the average absolute velocity along the line $x = 15$, which is the velocity downstream of the guide vane, U_{ds} . The trailing edge thickness was chosen as 0.64 mm corresponding to the earlier indicated length in Fig. 3.3. A geometry constant of 131 was chosen from Fig. 2.13, and a Strouhal number of 0.19 was assumed in accordance with Gongwer and Brekke [31, 34].

Table 4.3: Estimated vortex shedding frequency.

Operating point	U_{ds}	Brekke f_s
PL1	9.9 m/s	2053 Hz
PL2	9.5 m/s	1970 Hz
BEP	9.1 m/s	1887 Hz
HL	8.9 m/s	1846 Hz
FL	8.7 m/s	1804 Hz

By comparing the measured shedding frequencies with the corresponding ones estimated by Brekke’s formula, there is a strong agreement between the two. The maximum deviation between the estimated and measured frequency is at the HL operating point, with a discrepancy of 1.5% relative to the measured vortex shedding frequency. However, it is important to stress that several assumptions regarding the free stream velocity, trailing edge thickness, and geometry constant have been made in the empirical estimation of the vortex shedding frequency.

There is especially large uncertainty related to the value of the free stream velocity for foils in a cascade. For an isolated foil, the free stream velocity is equal to the velocity upstream of the foil. However, for foils in a cascade such as guide vanes, the fluid flow will accelerate through the guide vane passage. This makes the determination of the free stream velocity more difficult. In Brekke's formula, the vortex shedding frequency is proportional to the free stream velocity. The velocity upstream of the guide vane increases with a larger guide vane opening. By using the velocity upstream of the guide vane as the free stream velocity in Brekke's formula, it would have resulted in higher vortex shedding frequencies for the larger guide vane openings. However, the measured vortex shedding frequencies tend to decrease for larger guide vane openings. To use U_{ds} as the free stream velocity instead of using the upstream velocity in Brekke's formula seems to better predict the aforementioned trend of the vortex shedding frequency. This may indicate that a velocity near the guide vane trailing edge gives a more accurate estimate of the vortex shedding frequency, though further investigation is needed.

5 Conclusion

PIV measurements at five different operating points in a Francis turbine have been successfully conducted in the vaneless space. The PIV measurement system is a valuable asset for flow investigation in turbomachinery, and gives access to steady values of velocity as well as their periodic fluctuations. Consequently, a wide range of flow phenomena can be examined, such as vortex detection, wake propagation and rotor-stator interaction.

Rigorous considerations regarding the optical configuration, calibration set-up and recording parameters are the ingredients of a successful PIV experiment. The PIV set-up and PIV recording parameters have been presented, and may aid future PIV measurements in the vaneless space.

The time-averaged vector fields show close resemblance to previously conducted measurements in the vaneless space [8]. The geometry of the Francis turbine used in the measurements is open to the public. Accordingly, the measurement results can serve as a comparative basis for numerical simulations and flow measurements in the vaneless space.

The runner blade passing frequency was dominating near the runner inlet, and the vortex shedding frequencies were in the range of 1803-1977 Hz. The vortex shedding frequency increased with a decreasing guide vane angle and was found to be positively correlated with the absolute velocity downstream of the guide vane. The velocity field and vortex shedding frequency for the guide vane geometry at hand can be used as a baseline for further investigation on the trailing edge geometry of guide vanes.

6 Further work

PIV recordings were performed for two different lens objectives, 100 mm and 50 mm. In this thesis only the 100 mm recording were processed and presented. In the future it is of interest to process the 50 mm recordings and compare the results with the evaluated 100 mm recordings. In addition, the 50 mm recordings have an enlarged FOV which contains both the pressure and suction side of a plexiglass guide vane. This FOV might be better for a further assessment of the flow separation near the trailing edge since the area below the plexiglass guide vane suction side is illuminated. This could have given a clearer indication of the boundary layer separation points for the different guide vane openings.

Several vortex shedding frequency peaks in the range 1900-2080 Hz were present in the power spectra. This indicates that an image rate of 4166 Hz may not be sufficient in detecting the vortex shedding frequency. To allow for a higher image rate, a smaller FOV with a lower resolution than 1280 x 600 pixels is necessary. In order to satisfy the Nyquist theorem in the evaluation of the vortex shedding frequency, an image rate of at least 5000 Hz is suggested in future measurements. In addition, it is recommended with a higher seeding density allowing for a smaller interrogation area size is in future measurements. It could have been of interest to observe if this would result in different power spectra, and the vortex shedding frequencies would appear more dominant.

As the resolution of 1280 x 1024 pixels includes relatively large areas not containing any particles, a smaller FOV could have been used without the risk of losing any vector field. To investigate the rotor-stator interaction in further depth, a time-correlation for the PIV data with the runner blade position would be favourable. This could have shown how each runner blade passing impacts the instantaneous velocity fields in the vaneless space. Pressure measurements in combination with velocity measurements from PIV could have been very interesting in order to relate the two parameters with each other.

The hydraulic turbines are required to start and stop more frequently in order to sustain the stability of the grid. To investigate the influence such operation will have on the hydraulic turbines, PIV measurements under transient operating conditions would be a natural continuation of this work.

References

- [1] Commission, European Union: European (2018). Communication from the commission to the European Parliament, the European Council, the Council, the European Economic and Social Committee, the Committee of the Regions and the European Investment Bank: A Clean Planet for all. A European strategic long-term vision for a prosperous, modern, competitive and climate neutral economy. COM(2018) 773 final. URL: https://ec.europa.eu/clima/sites/clima/files/docs/pages/com_2018_733_en.pdf.
- [2] Hirth, L. (2015). The optimal share of variable renewables: How the variability of wind and solar power affects their welfare-optimal deployment. In: *The Energy Journal*, pp. 149–184. URL: <https://www.jstor.org/stable/pdf/24695016.pdf?refreqid=excelsior%3A1f3ae520586e3e39ef732451fa515dc>.
- [3] Goyal, Rahul and Gandhi, Bhupendra K (2018). Review of hydrodynamics instabilities in Francis turbine during off-design and transient operations. In: *Renewable energy* 116, pp. 697–709. URL: <https://www.sciencedirect.com/science/article/pii/S0960148117309734>.
- [4] Castillo, A. and Gayme, D.F. (2014). Grid-scale energy storage applications in renewable energy integration: A survey. In: *Energy Conversion and Management* 87, pp. 885–894. URL: <https://www.sciencedirect.com/science/article/pii/S0196890414007018>.
- [5] Ellabban, O., Abu-Rub, H., and Blaabjerg, F. (2014). Renewable energy resources: Current status, future prospects and their enabling technology. In: *Renewable and Sustainable Energy Reviews* 39, pp. 748–764. URL: <https://www.sciencedirect.com/science/article/pii/S1364032114005656>.
- [6] Guangjie, Peng, Zhengwei, Wang, Yexiang, Xiao, and Yongyao, Luo (2013). Abrasion predictions for Francis turbines based on liquid–solid two-phase fluid simulations. In: *Engineering Failure Analysis* 33, pp. 327–335. URL: <https://www.sciencedirect.com/science/article/pii/S1350630713002021>.
- [7] Haas, R., Hiebert, M., and Hoatson, E. (2014). Francis Turbines - Fundamentals and Everything Else You Didn't Know That You Wanted To Know. In: *Colorado State University, CIVE 401*. URL: https://www.engr.colostate.edu/~pierre/ce_old/classes/CIVE%20401/Team%20reports/6%20-%20Francis%20Turbines%20-%20Haas%20Hiebert%20Hoatson.pdf.
- [8] Straume, S.G. (2018). PIV measurement of the flow in the vaneless space of a Francis Turbine. MA thesis. Trondheim: Norwegian University of Science, Technology, Faculty of Engineering Science & Technology, Department of Energy, and Process Engineering. URL: <http://hdl.handle.net/11250/2568081>.
- [9] Sagmo, K. (2018). Measurement report 2018 WP2.1, NTNU. Classification: Restricted.
- [10] Trivedi, C., Cervantes, M.J., Gandhi, B.K., and Dahlhaug, O.G. (2013). Experimental and numerical studies for a high head Francis turbine at several operating points. In: *Journal of Fluids Engineering* 135.11, p. 111102. URL: <https://fluidsengineering.asmedigitalcollection.asme.org/article.aspx?articleid=1725580>.
- [11] Brekke, H. (2000). Grunnkurs i hydrauliske Strømningsmaskiner. Norwegian.

- [12] Zobeiri, A. (2009). Investigations of time dependent flow phenomena in a turbine and a pump-turbine of Francis type: rotor-stator interactions and precessing vortex rope. PhD thesis. URL: <https://infoscience.epfl.ch/record/128887>.
- [13] Dixon, S.L. (2014). *Fluid mechanics and thermodynamics of turbomachinery*. 7th ed. Amsterdam: Elsevier Science : Butterworth-Heinemann, pp. 363–384. ISBN: 9780124159549. URL: <https://www.sciencedirect.com/book/9781856177931/fluid-mechanics-and-thermodynamics-of-turbomachinery>.
- [14] Drtina, P. and Sallaberger, M. (1999). Hydraulic turbines—basic principles and state-of-the-art computational fluid dynamics applications. In: *Proceedings of the Institution of Mechanical Engineers, Part C: Journal of Mechanical Engineering Science* 213.1, pp. 85–102.
- [15] Çengel, Y.A. and Cimbala, J.M. (2014). *Fluid mechanics: fundamentals and applications*. 3rd ed. in SI units. Boston: McGraw-Hill. ISBN: 9781259011221.
- [16] Iliev, I., Trivedi, C., Agnalt, E., and Dahlhaug, O.G. (2019). Variable-speed operation and pressure pulsations in a Francis turbine and a pump-turbine. In: *IOP Conference Series: Earth and Environmental Science*. Vol. 240. 7. IOP Publishing, p. 072034. URL: <https://iopscience.iop.org/article/10.1088/1755-1315/240/7/072034/pdf>.
- [17] Schlichting, H. and Gersten, K. (2017). *Boundary-Layer Theory*. 9th ed. 2017. Berlin, Heidelberg: Springer Berlin Heidelberg, pp. 6–14. ISBN: 9783662529171. URL: <https://link.springer.com/content/pdf/10.1007%2F978-3-662-52919-5.pdf>.
- [18] Blake, W.K. (2017). *Mechanics of Flow-Induced Sound and Vibration, Volume 2: Complex Flow-Structure Interactions Volume 2, Complex flow-structure interactions*. eng. Second edition. Vol. 2. Academic Press. URL: <https://www.sciencedirect.com/book/9780128092743/mechanics-of-flow-induced-sound-and-vibration-volume-2>.
- [19] Antonsen, Ø. (2007). Unsteady flow in wicket gate and runner with focus on static and dynamic load on runner. PhD thesis. Norwegian University of Science, Technology, Faculty of Engineering Science & Technology, Department of Energy, and Process Engineering. ISBN: 978-82-471-3408-5. URL: <http://hdl.handle.net/11250/233347>.
- [20] Wu, Y.T. (1972). Cavity and wake flows. In: *Annual Review of Fluid Mechanics* 4.1, pp. 243–284.
- [21] Bolstad, M.T. (2017). Experimental investigation and mitigation of vortex shedding. MA thesis. Trondheim: Norwegian University of Science, Technology, Faculty of Engineering Science & Technology, Department of Energy, and Process Engineering.
- [22] Tech, Virginia (n.d.). Flow Separation. Retrieved: April 30, 2019. URL: <http://www.dept.aoe.vt.edu/~cdhall/courses/aoe2104/AircraftFlight.pdf>.
- [23] Strouhal, V. (1878). Über eine besondere Art der Tonerregung. Translated from German. In: *Annalen der Physik* 241.10.
- [24] Flow around objects (n.d.). Retrieved: November 18, 2018. URL: http://www.et4u.org/Toy_information/Cylinder_flow.html.
- [25] Shames, I.H. (1962). *Mechanics of fluids*. New York: McGraw-Hill.

- [26] Wu, Y. (2013a). *Vibration of Hydraulic Machinery*. Vol. 11. Mechanisms and Machine Science. Dordrecht, pp. 160–164. ISBN: 94-007-6422-7.
- [27] Wagner, J. (2014). File: Karmansche Wirbelstr kleine Re.JPG. Retrieved: November 27, 2018. URL: https://commons.wikimedia.org/wiki/File:Karmansche_Wirbelstr_kleine_Re.JPG.
- [28] Heskestad, G. and Olberts, D.R. (1960). Influence of Trailing-Edge Geometry on Hydraulic-Turbine-Blade Vibration Resulting From Vortex Excitation. In: *Journal of Engineering for Power* 82.2. ISSN: 00220825. URL: <http://gasturbinespower.asmedigitalcollection.asme.org/article.aspx?articleid=1415768>.
- [29] White, F.M. and Corfield, I. (2006). *Viscous fluid flow*. Vol. 3. McGraw-Hill New York.
- [30] Gopalkrishnan, R. (1993). Vortex-Induced Forces on Oscillating Bluff Cylinders. PhD thesis. Department of Ocean Engineering, MIT, Department of Applied Ocean Physics, and Engineering, WHOI. URL: <http://handle.dtic.mil/100.2/ADA265056>.
- [31] Gongwer, C. A. (1952). A study of vanes singing in water. In: *Journal of applied mechanics- transactions of the ASME* 19.4, pp. 432–438.
- [32] Donaldson, R.M. (1956). Hydraulic turbine runner vibration. In: *ASME J. Eng. Power* 78, pp. 1141–1147.
- [33] Brekke, H. (2003). Pumper & Turbiner. Translated from Norwegian.
- [34] Brekke, H. (2010). A Review on Oscillatory Problems in Francis Turbine. In: *New Trends in Technologies: Devices, Computer, Communication and Industrial Systems, Sciyo*, pp. 217–232. URL: <http://cdn.intechweb.org/pdfs/12284.pdf>.
- [35] Blevins, R.D. (1985). The effect of sound on vortex shedding from cylinders. In: *Journal of Fluid Mechanics* 161, pp. 217–237. URL: https://www.cambridge.org/core/services/aop-cambridge-core/content/view/6E52A93A4C5624412C23BCA3FBA1F413/S0022112085002890a.pdf/effect_of_sound_on_vortex_shedding_from_cylinders.pdf.
- [36] Lienhard, J.H. et al. (1966). *Synopsis of lift, drag, and vortex frequency data for rigid circular cylinders*. Vol. 300. Technical Extension Service, Washington State University. URL: <http://www.uh.edu/engines/vortexcylinders.pdf>.
- [37] Marris, A.W. (1964). A review on vortex streets, periodic wakes, and induced vibration phenomena. In: *Journal of Basic Engineering* 86.2, pp. 185–193. URL: <https://fluidsengineering.asmedigitalcollection.asme.org/article.aspx?articleid=1431610>.
- [38] Sagmo, K.F., Tengs, E.O., Bergan, C.W., and Storli, P.T. (2019). PIV measurements and CFD simulations of a hydrofoil at lock-in. In: *IOP Conference Series: Earth and Environmental Science*. Vol. 240. 6. IOP Publishing, p. 062006. URL: <https://iopscience.iop.org/article/10.1088/1755-1315/240/6/062006/meta>.
- [39] Dörfler, P (2013). *Flow-induced pulsation and vibration in hydroelectric machinery - Engineer's Guidebook for Planning, Design and Troubleshooting*. London: Springer, pp. 111–113. ISBN: 1-283-62217-3.
- [40] Trivedi, C. and Cervantes, M.J. (2017). Fluid-structure interactions in Francis turbines: A perspective review. In: *Renewable and Sustainable Energy Reviews* 68.P1, pp. 87–101. ISSN: 1364-0321. URL: <https://www.sciencedirect.com/science/article/pii/S1364032116306335>.

- [41] Leonhardsen, S. (2017). Numerical Investigation of Flow Field subject to Vibrating Structure. MA thesis, p. 15. URL: <http://hdl.handle.net/11250/2457140>.
- [42] Wu, Y. (2013b). *Vibration of Hydraulic Machinery*. Vol. 11. Mechanisms and Machine Science. Dordrecht, pp. 194–207. ISBN: 94-007-6422-7.
- [43] Zobeiri, A., Kueny, J.L., Farhat, M., and Avellan, F. (2006). Pump-turbine rotor-stator interactions in generating mode: pressure fluctuation in distributor channel. In: *23rd IAHR symposium on hydraulic machinery and systems*. LMH-CONF-2006-008. URL: <https://infoscience.epfl.ch/record/90765>.
- [44] Nicolet, C., Ruchonnet, N., and Avellan, F. (2006). One-dimensional modeling of rotor stator interaction in Francis pump-turbine. In: *Proceedings of the 23rd IAHR Symposium on Hydraulic Machinery and Systems, Yokohama, Japan*. Vol. 1. CONF. International Association For Hydraulic Research, pp. 1–15. URL: <https://infoscience.epfl.ch/record/104110>.
- [45] Agnalt, E. (2018). Measurement report 2017. HiFrancis WP 1.3, NTNU. Classification: Restricted.
- [46] Goyal, R., Gandhi, B.K., and Cervantes, M.J. (2018). PIV measurements in Francis turbine – A review and application to transient operations. In: *Renewable and Sustainable Energy Reviews* 81.P2, pp. 2976–2991. ISSN: 1364-0321. URL: <https://www.sciencedirect.com/science/article/pii/S136403211731047X>.
- [47] Su, W.T., Li, X.B., Li, F.C., Wei, X.Z., Han, W.F., and Liu, S.H. (2014). Experimental investigation on the characteristics of hydrodynamic stabilities in Francis hydroturbine models. In: *Advances in Mechanical Engineering*. ISSN: 1687-8132. URL: <https://journals.sagepub.com/doi/abs/10.1155/2014/486821>.
- [48] Raffel, M., Willert, C.E., Scarano, F., Kähler, C.J., Wereley, S.T., and Kompenhans, J. (2018a). *Particle Image Velocimetry - A Practical Guide*. 3rd ed. Cham, Switzerland: Springer International Publishing AG. ISBN: 978-3-319-68851-0.
- [49] Dabiri, D. (2006). Cross-correlation digital particle image velocimetry—a review. In: *Turbul. ABCM Curitiba* 155, p. 199. URL: <https://www.aa.washington.edu/sites/aa/files/faculty/dabiri/pubs/piV.Review.Paper.final.pdf>.
- [50] Raffel, M., Willert, C.E., Scarano, F., Kähler, C.J., Wereley, S.T., and Kompenhans, J. (2018b). *Particle Image Velocimetry - A Practical Guide*. 3rd ed. Cham, Switzerland: Springer International Publishing AG, pp. 33–51. ISBN: 978-3-319-68851-0.
- [51] Melling, A. (1997). Tracer particles and seeding for particle image velocimetry. In: *Measurement Science and Technology* 8.12, p. 1406. URL: <https://iopscience.iop.org/article/10.1088/0957-0233/8/12/005/pdf>.
- [52] GmbH, LaVision (2017a). Laser Guiding Arm Product-Manual. Item-numbers: 1108453, 1108375. Document name: 1004089_LaserGuidingArm.D84.pdf.
- [53] GmbH, LaVision (2017b). FlowMaster Product-Manual. Item-numbers: 1105011-4. Document name: 1003005_FlowMaster_D84.pdf.

- [54] Qian, R., Deschênes, C., and Fraser, R. (2018). Flow Field Measurement at the Distributor of Francis Turbines. In: URL: https://www.researchgate.net/publication/242155329_Flow_Field_Measurement_at_the_Distributor_of_Francis_Turbines.
- [55] Thapa, B.S., Dahlhaug, O.G., and Thapa, B. (2018). Flow measurements around guide vanes of Francis turbine: A PIV approach. In: *Renewable Energy* 126, pp. 177–188. ISSN: 0960-1481. URL: <https://www.sciencedirect.com/science/article/pii/S0960148118303537>.
- [56] King, M. (2017). Fourier Transform. eng. In: *Statistics for Process Control Engineers*. Chichester, UK: John Wiley Sons, Ltd, pp. 305–313. ISBN: 9781119383505.
- [57] GmbH, LaVision (2017c). Imaging Tools - Product-Manual. Item-number: 1005xxx. Document name: 1003012_ImagingTools_D84.pdf.
- [58] Tornblom, O. (2004). Introduction course in particle image velocimetry. In: *Course Introductory Material: STEM Project, KTH, Department of Mechanics, Stockholm Sweden*. URL: <https://www.mech.kth.se/~olle/pivkurs/Intro.to.PIV.pdf>.
- [59] Raffel, M., Willert, C.E., Scarano, F., Kähler, C.J., Wereley, S.T., and Kompenhans, J. (2018c). *Particle Image Velocimetry - A Practical Guide*. 3rd ed. Cham, Switzerland: Springer International Publishing AG, p. 452. ISBN: 978-3-319-68851-0.
- [60] Keane, R.D. and Adrian, R.J. (1991). Optimization of particle image velocimeters: II. Multiple pulsed systems. In: *Measurement Science and Technology* 2.10, p. 963. URL: <https://iopscience.iop.org/article/10.1088/0957-0233/2/10/013/meta>.
- [61] Raffel, M., Willert, C.E., Scarano, F., Kähler, C.J., Wereley, S.T., and Kompenhans, J. (2018d). *Particle Image Velocimetry - A Practical Guide*. 3rd ed. Cham, Switzerland: Springer International Publishing AG, pp. 203–229. ISBN: 978-3-319-68851-0.
- [62] Westerweel, J. (1994). Efficient detection of spurious vectors in particle image velocimetry data. In: *Experiments in Fluids* 16.3-4, pp. 236–247. URL: <https://link.springer.com/article/10.1007/BF00206543>.
- [63] Barbosa, L.V. (2013). Fourier transform time and frequency domains. Retrieved: April 3, 2019. URL: https://commons.wikimedia.org/wiki/File:Fourier_transform_time_and_frequency_domains.gif.
- [64] JCGM (2008). Evaluation of measurement data — Guide to the expression of uncertainty in measurement. In: *Int. Organ. Stand. Geneva ISBN* 50. URL: https://www.bipm.org/utils/common/documents/jcgm/JCGM_100_2008_E.pdf.
- [65] Mays, L.W. (2004). Hydraulic design handbook. New York.
- [66] GmbH, LaVision (2017d). DaVis 8.4 Software Product-Manual. Item-number: 1105xxx. Document name: 1003001_DaVis_D84.pdf.
- [67] Wieneke, B. (2015). PIV uncertainty quantification from correlation statistics. In: *Measurement Science and Technology* 26.7, p. 074002. URL: <https://iopscience.iop.org/article/10.1088/0957-0233/26/7/074002>.
- [68] Ramdal, J. and Dahlhaug, O.G. (2006a). FD-4624-4 Calibration of discharge measurement system in the Francis Turbine Test Rig. Classification: Open.
- [69] Ramdal, J. and Dahlhaug, O.G. (2006b). LC-4536 Calibration of differential pressure transducers. Classification: Open.

- [70] Trivedi, C. (2018). Investigations of compressible turbulent flow in a high-head francis turbine. In: *Journal of Fluids Engineering* 140.1, p. 011101. URL: <https://fluidsengineering.asmedigitalcollection.asme.org/article.aspx?articleid=2648173>.
- [71] Commission, International Electrotechnical et al. (1999). Hydraulic turbines, storage pumps and pump-turbines—model acceptance tests. In: *Standard No. IEC 60193*.

Appendices

A Coordinate systems

Below, in Fig. A.1, is presented the local coordinate system of the measurement area and the global coordinate system of the Francis turbine. Note that the turbine is seen from below and the z-axis is directed perpendicular to the xy-plane in the depth.



Figure A.1: An overview of the local coordinate system of the FOV and the global coordinate system of the turbine.

Table A.1 presents the local and global coordinates that the 1280 x 1024 pixel FOV is bounded by.

Table A.1: Local coordinates that bound the 1280 x 1024 FOV converted into to global coordinates.

Local coordinates (x, y)	Global coordinates (x, y)
(22.566, 17.961)	(347.137, -8.453)
(22.566, -17.076)	(313.908, 2.658)
(-21.239, -17.076)	(300.017, -38.886)
(-21.239, 17.961)	(333.245, 49.997)

B Laser subsystem, laser overlap test and PTU synchronization test

The laser subsystem consists of a laser head, mounting block, laser guiding arm, and sheet optics. Inside the laser head there are two lasers, and two respective cavities with the purpose of aligning the lasers. The mounting block contains a mirror that changes the direction of the incoming lasers 90 degrees. On the mounting block, the laser guiding arm is mounted. On the outlet of the laser guiding arm, sheet optics are placed with the purpose of transforming the laser light into a laser sheet [52].

It is crucial that the two laser beams perfectly coincide with each other and the FOV. Several tests have been performed to assure that the two lasers illuminate the exact same plane. The first tests were performed on the laser head. To check if the two laser beams were aligning inside the laser head, one test over a short distance and one over a longer distance were performed. Inside the laser head there are located several angled mirrors that can become misaligned due to for example shipment or movement of the equipment. Laser 1 and laser 2 do not originate from the same location, but need to come out perpendicular from the laser head and overlap over a short and long distance. The short distance test were performed by mounting a beam adjustment tool directly to the laser head. In order to assure that the lasers are coming out perpendicular to the laser head, the laser beams have to point through the orange apertures inside the laser beam adjustment tool. Both lasers were repeatedly turned on and off to assure that both were perpendicular to the laser head and coinciding. Next, a long distance test was performed by using a pipe with a length of about 2 metres. On the outlet of the pipe there was placed a grid paper to determine if the lasers were coinciding over a long distance.

After the laser head alignment was shown sufficient, the adjustment of the mounting block were to be performed. This was executed by mounting the mounting block to the laser head, and mount the outlet of the mounting block to the beam adjustment tool. Vertical and horizontal adjustments of the mirror inside the mounting block were done in order to have the beams to point through the orange apertures. Then a test of the laser guiding arm were to be done. Now the laser guiding arm were mounted to the mounting block, while the beam adjustment tool were mounted to the outlet of the laser guiding arm. The same procedure as with the mounting block was performed.

It is important that the laser pulses are properly synchronized with the camera by the PTU. The synchronization between the laser and camera have been checked according to the following routine. At first, the first pulse was deactivated while the camera recorded two successive frames. Here, only the first image should be illuminated. Then the second pulse was deactivated while the camera recorded two successive frames. Now, only the second frame should be illuminated. At last, both pulses were activated while recording two frames. Here both frames should be illuminated.

C Sensor uncertainty

Prior to the measurements, calibrations of the flow meter, and inlet and differential pressure cells were performed in accordance with calibration procedures at the Waterpower Laboratory at NTNU [68, 69]. By following GUM 2008 [64], the combined relative uncertainties of the head and discharge in each operating point were calculated, and are presented in Table C.1. The uncertainties are presented relative to the head and discharge value for the considered operating point.

Table C.1: Combined relative uncertainties at different operating points.

Operating point	Relative uncertainty, H	Relative uncertainty, Q
PL1	0.024%	0.052%
PL2	0.024%	0.064%
BEP	0.024%	0.132%
OL	0.024%	0.096%
FL	0.023%	0.030%

The uncertainties of the rotational speed and guide vane angle were not quantified by the author. Trivedi [70] has in 2018 quantified the uncertainty of the runner rotational speed to be $\pm 0.035\%$ and the uncertainty of the guide vane angular position to be $\pm 0.7\%$ at BEP. This was quantified in accordance with IEC 60193 [71].

D Power spectra for different operating points

Below are presented power spectra obtained from the cross velocity flow component for operating points: PL2, OL and FL. Amplitudes in Fig. D.1, Fig. D.2 and Fig. D.2 are normalized with respect to each set's maximum amplitude. Since the RSI frequency is the most dominant frequency for Set 2 and Set 3 in Fig. D.3, the amplitudes in these sets are normalized with respect to the second most dominating frequency.

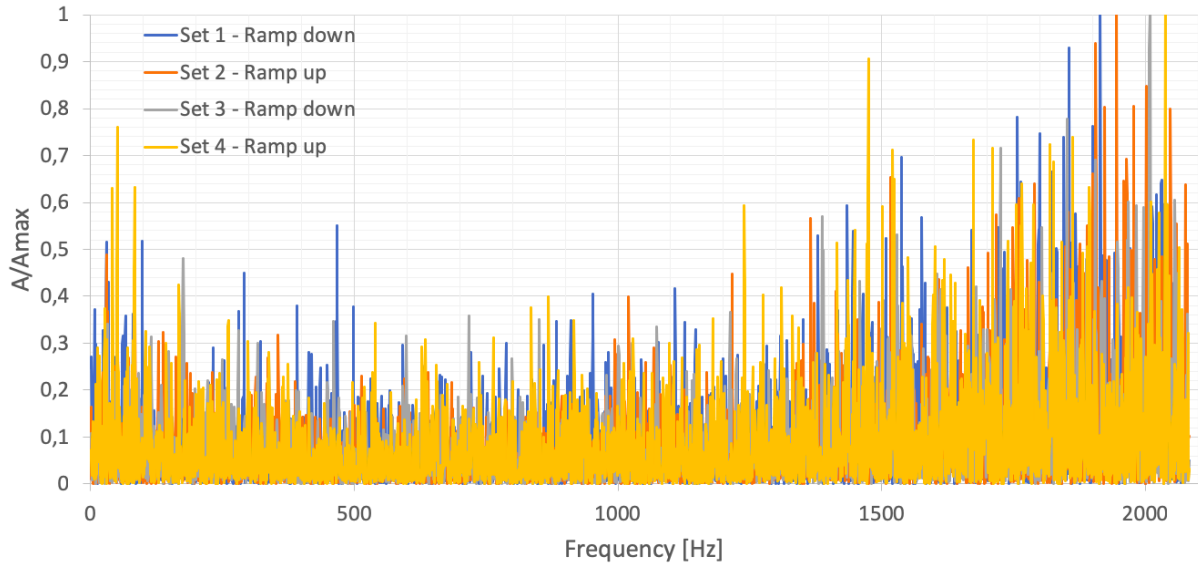


Figure D.1: Power spectrum obtained from cross flow velocity component at position (15, 3) for a guide vane opening of 6.7 degrees.

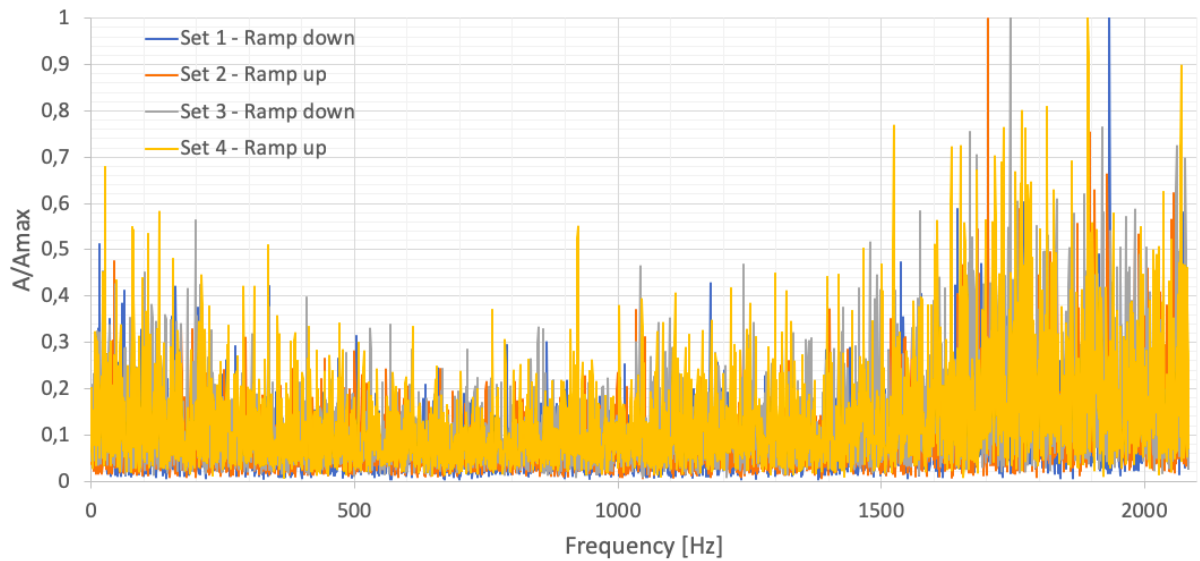


Figure D.2: Power spectrum obtained from cross flow velocity component at position (15, -2) for a guide vane opening of 12.4 degrees.

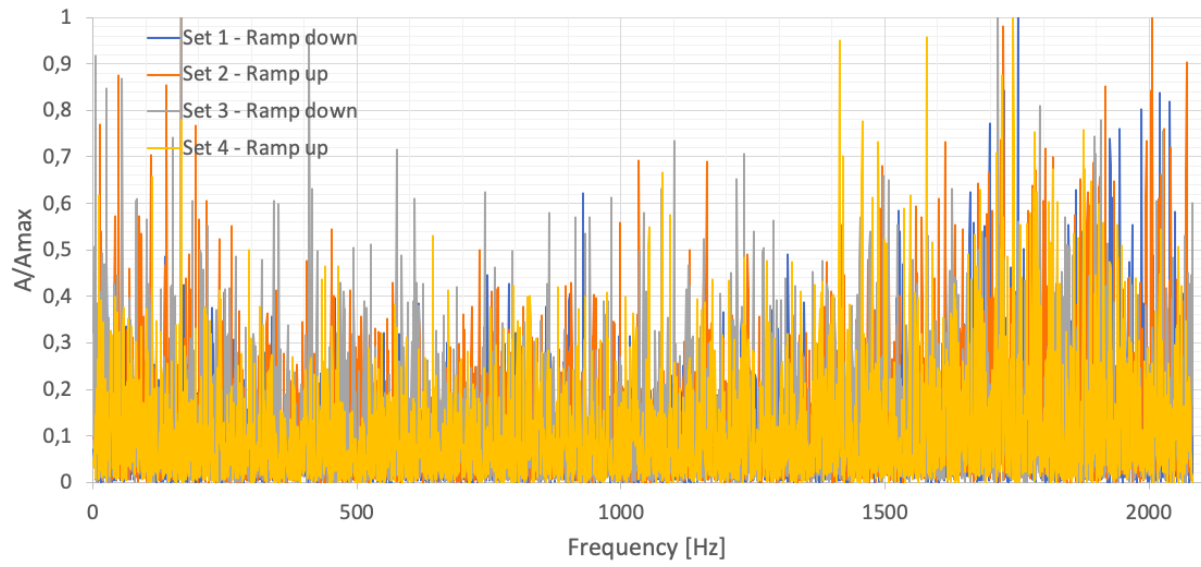


Figure D.3: Power spectrum obtained from cross flow velocity component at position (15, -4) for a guide vane opening of 14 degrees.

E Risk Assessment Report and Attachment to Risk Assessment Report

Risk Assessment Report

Francis turbine

Project name	PIV measurement in the vaneless space of Francis turbine
Apparatus	Double-Cavity High speed laser, 2*10Mj, 1000Hz, 527nm
Unit	EPT
Equipment manager	Bård Brandåstrø
Project leader	Pål Tore Storli
HSE coordinator	Morten Grønli
HSE responsible (linjeleder)	Therese Løvås
Location	Waterpower Laboratory
Room number	11
Risk assessment performed by	Magne Tveit Bolstad

Approval:

Apparatur kort (UNIT CARD) valid for:	12 months
Forsøk pågår kort (EXPERIMENT IN PROGRESS) valid for:	12 months


Rolle	Navn	Dato	Signatur
Project leader	Pål-Tore Storli	7/2-19	
HSE coordinator	Morten Grønli		
HSE responsible (linjeleder)	Therese Løvås		

TABLE OF CONTENTS

1	INTRODUCTION	1
2	CONCLUSION	ERROR! BOOKMARK NOT DEFINED.
3	ORGANISATION	1
4	RISK MANAGEMENT IN THE PROJECT	1
5	DESCRIPTIONS OF EXPERIMENTAL SETUP	2
6	EVACUATION FROM THE EXPERIMENTAL AREA.....	2
7	WARNING	2
7.1	Before experiments.....	2
7.2	Non-conformance	2
8	ASSESSMENT OF TECHNICAL SAFETY	3
8.1	HAZOP	3
8.2	Flammable, reactive and pressurized substances and gas	3
8.3	Pressurized equipment.....	4
8.4	Effects on the environment (emissions, noise, temperature, vibration, smell)	4
8.5	Radiation	4
8.6	Chemicals	4
8.7	Electricity safety (deviations from the norms/standards).....	4
9	ASSESSMENT OF OPERATIONAL SAFETY	4
9.1	Procedure HAZOP.....	4
9.2	Operation and emergency shutdown procedure.....	4
9.3	Training of operators.....	5
9.4	Technical modifications.....	5
9.5	Personal protective equipment.....	5
	9.5.1 General Safety	5
9.6	Safety equipment	5
9.7	Special predations	5
10	QUANTIFYING OF RISK - RISK MATRIX.....	5
11	REGULATIONS AND GUIDELINES	6
12	DOCUMENTATION.....	6
13	GUIDANCE TO RISK ASSESSMENT TEMPLATE.....	7

1 INTRODUCTION

PIV measurements will be performed on a Site Acceptance Test-rig in accordance with the new PIV equipment at the Waterpower Laboratory. Measurements will be performed in February-April, 2019.

2 ORGANISATION

Role	
Project leader	Pål Tore Storli
Equipment manager	Bård Brandåstrø
Room manager	Bård Brandåstrø
HSE coordinator	Morten Grønli
HSE responsible (linjeleder)	Therese Løvås

3 RISK MANAGEMENT IN THE PROJECT

Hovedaktiviteter risikostyring	Nødvendige tiltak, dokumentasjon	DATE
Prosjekt initiering Project initiation	Prosjekt initiering mal	
Veiledningsmøte Guidance Meeting	Skjema for Veiledningsmøte med pre-risikovurdering	
Innledende risikovurdering Initial Assessment	Fareidentifikasjon – HAZID Skjema grovanalyse	
Vurdering av teknisk sikkerhet Evaluation of technical security	Prosess-HAZOP Tekniske dokumentasjoner	
Vurdering av operasjonell sikkerhet Evaluation of operational safety	Prosedyre-HAZOP Opplæringsplan for operatører	
Sluttvurdering, kvalitetssikring Final assessment, quality assurance	Uavhengig kontroll Utstedelse av apparaturkort Utstedelse av forsøk pågår kort	

4 DESCRIPTIONS OF EXPERIMENTAL SETUP

- Drawings and photos describing the setup.
- Process and Instrumentation Diagram (PID) with list of components
- Location of the operator, gas bottles, shutdown valves for water / air.

5 EVACUATION FROM THE EXPERIMENTAL AREA

Evacuate at signal from the alarm system or local gas alarms with its own local alert with sound and light outside the room in question, see 6.2

Evacuation from the rigging area takes place through the marked emergency exits to the assembly point, (corner of Old Chemistry Kjelhuset or parking 1a-b.)

Action on rig before evacuation:

Describe in which condition the rig should be left in case of evacuation (emergency shutdown procedure, water, gas, electric supply, etc.)

6 WARNING

6.1 Before experiments

Send an e-mail with information about the planned experiment to:
iept-experiments@ivt.ntnu.no

The e-mail must include the following information:

- Name of responsible person:
- Experimental setup/rig:
- Start Experiments: (date and time)
- Stop Experiments: (date and time)

You must get the approval back from the laboratory management before start up. All running experiments are notified in the activity calendar for the lab to be sure they are coordinated with other activity.

6.2 Non-conformance

FIRE

If you are NOT able to extinguish the fire, activate the nearest fire alarm and evacuate area. Be then available for fire brigade and building caretaker to detect fire place. If possible, notify:

NTNU	SINTEF
Morten Grønli, Mob: 918 97 515	Harald Mæhlum, Mob: 930 14 986
Therese Løvås, Mob: 91897007	Anne Karin T. Hemmingsen Mob: 930 19 669
NTNU – SINTEF Beredskapstelefon	800 80 388

GAS ALARM

If a gas alarm occurs, close gas bottles immediately and ventilate the area. If the level of the gas concentration does not decrease within a reasonable time, activate the fire alarm and evacuate the lab. Designated personnel or fire department checks the leak to determine whether it is possible to seal the leak and ventilate the area in a responsible manner.

PERSONAL INJURY

- First aid kit in the fire / first aid stations
- Shout for help
- Start life-saving first aid
- **CALL 113** if there is any doubt whether there is a serious injury

OTHER NON-CONFORMANCE (AVVIK)

NTNU:

You will find the reporting form for non-conformance on:
<https://innsida.ntnu.no/wiki/-/wiki/Norsk/Melde+avvik>

SINTEF:

Synergi

7 ASSESSMENT OF TECHNICAL SAFETY

7.1 HAZOP

See Chapter 13 "Guide to the report template".

The experiment set up is divided into the following nodes:

Node 1	Blade cascade
Node 2	Laser class IV
Node 3	Tent/enclosure

Attachments, Form: Hazop_mal

Conclusion

Node 1:

- Pressure is supervised during operation

Node 2:

- Radiation area shielded
- Appropriate signalling and lights in place, light active during operation

Node 3:

- Appropriate signalling and lights in place, light active during operation

7.2 Flammable, reactive and pressurized substances and gas

See Chapter 13 "Guide to the report template".

NO	
----	--

7.3 Pressurized equipment

See Chapter 13 "Guide to the report template".

YES	
-----	--

7.4 Effects on the environment (emissions, noise, temperature, vibration, smell)

See Chapter 13 "Guide to the report template".

NO	
----	--

7.5 Radiation

See Chapter 13 "Guide to the report template".

YES	Radiation Sources need to have an own risk assessment
-----	---

Attachments: Radiation risk assessment

Conclusion:

7.6 Chemicals

See Chapter 13 "Guide to the report template".

NO	
----	--

7.7 Electricity safety (deviations from the norms/standards)

See Chapter 13 "Guide to the report template".

NO	
----	--

8 ASSESSMENT OF OPERATIONAL SAFETY

Ensure that the procedures cover all identified risk factors that must be taken care of. Ensure that the operators and technical performance have sufficient expertise.

8.1 Procedure HAZOP

See Chapter 13 "Guide to the report template".

The method is a procedure to identify causes and sources of danger to operational problems.

Attachments:: HAZOP_MAL_Prosegyre

8.2 Operation procedure and emergency shutdown procedure

See Chapter 13 "Guide to the report template".

The operating procedure is a checklist that must be filled out for each experiment.

Emergency procedure should attempt to set the experiment set up in a harmless state by unforeseen events.

Attachments: Procedure for running experiments

Emergency shutdown procedure:

8.3 Training of operators

8.4 Technical modifications

8.5 Personal protective equipment

- *It is mandatory use of appropriate eye protection in the rig zone*

8.6 General Safety

- *The area around the staging attempts shielded.*
- *Operator has to be present during experiments.*

8.7 Safety equipment

- *Warning signs and warning light, see the Regulations on Safety signs and signalling in the workplace*

8.8 Special predations

9 QUANTIFYING OF RISK - RISK MATRIX

See Chapter 13 "Guide to the report template".

The risk matrix will provide visualization and an overview of activity risks so that management and users get the most complete picture of risk factors.

IDnr	Aktivitet-hendelse	Frekv-Sans	Kons	RV
1	<i>Unintentional refraction/reflection of laser beam</i>	1	A	LA
2	<i>People without protective goggles entering radiation area</i>	1	C	1C
3	<i>Damaging lab equipment</i>	2	B	2B
4	<i>Water-damage on lab equipment</i>	3	B	3C
5	<i>Structural failure due to high pressure</i>	1	C	1C

Conclusion: There is little remaining risk. The most prominent risk is that people unintentionally wander into the radiation area without protective goggles, but proper signalling and blocking should prevent this. The risk is therefore acceptable.

10 REGULATIONS AND GUIDELINES

Se <http://www.arbeidstilsynet.no/regelverk/index.html>

- Lov om tilsyn med elektriske anlegg og elektrisk utstyr (1929)
- Arbeidsmiljøloven
- Forskrift om systematisk helse-, miljø- og sikkerhetsarbeid (HMS Internkontrollforskrift)
- Forskrift om sikkerhet ved arbeid og drift av elektriske anlegg (FSE 2006)
- Forskrift om elektriske forsyningsanlegg (FEF 2006)
- Forskrift om utstyr og sikkerhetssystem til bruk i eksplosjonsfarlig område NEK 420
- Forskrift om håndtering av brannfarlig, reaksjonsfarlig og trykksatt stoff samt utstyr og anlegg som benyttes ved håndteringen
- Forskrift om Håndtering av eksplosjonsfarlig stoff
- Forskrift om bruk av arbeidsutstyr.
- Forskrift om Arbeidsplasser og arbeidslokaler
- Forskrift om Bruk av personlig verneutstyr på arbeidsplassen
- Forskrift om Helse og sikkerhet i eksplosjonsfarlige atmosfærer
- Forskrift om Høytrykksspyling
- Forskrift om Maskiner
- Forskrift om Sikkerhetsskilting og signalgivning på arbeidsplassen
- Forskrift om Stillaser, stiger og arbeid på tak m.m.
- Forskrift om Sveising, termisk skjæring, termisk sprøyting, kullbuemeisling, lodding og sliping (varmt arbeid)
- Forskrift om Tekniske innretninger
- Forskrift om Tungt og ensformig arbeid
- Forskrift om Vern mot eksponering for kjemikalier på arbeidsplassen (Kjemikalieforskriften)
- Forskrift om Vern mot kunstig optisk stråling på arbeidsplassen
- Forskrift om Vern mot mekaniske vibrasjoner
- Forskrift om Vern mot støy på arbeidsplassen

Veiledninger fra arbeidstilsynet

se: <http://www.arbeidstilsynet.no/regelverk/veiledninger.html>

11 DOCUMENTATION

- Tegninger, foto, beskrivelser av forsøksoppsetningen
- Hazop_mal
- Sikker bruk av LASERE, retningslinje
- HAZOP_MAL_Proseedyre
- Forsøksproseedyre
- Opplæringsplan for operatører
- Skjema for sikker jobb analyse, (SJA)
- Apparatorkortet
- Forsøk pågår kort

12 GUIDANCE TO RISK ASSESSMENT TEMPLATE

Chapter 7 Assessment of technical safety.

Ensure that the design of the experiment set up is optimized in terms of technical safety.

Identifying risk factors related to the selected design, and possibly to initiate re-design to ensure that risk is eliminated as much as possible through technical security.

This should describe what the experimental setup actually are able to manage and acceptance for emission.

7.1 HAZOP

The experimental set up is divided into nodes (eg motor unit, pump unit, cooling unit.). By using guidewords to identify causes, consequences and safeguards, recommendations and conclusions are made according to if necessary safety is obtained. When actions are performed the HAZOP is completed.

(e.g. "No flow", cause: the pipe is deformed, consequence: pump runs hot, precaution: measurement of flow with a link to the emergency or if the consequence is not critical used manual monitoring and are written into the operational procedure.)

7.2 Flammable, reactive and pressurized substances and gas.

According to the Regulations for handling of flammable, reactive and pressurized substances and equipment and facilities used for this:

Flammable material: Solid, liquid or gaseous substance, preparation, and substance with occurrence or combination of these conditions, by its flash point, contact with other substances, pressure, temperature or other chemical properties represent a danger of fire.

Reactive substances: Solid, liquid, or gaseous substances, preparations and substances that occur in combinations of these conditions, which on contact with water, by its pressure, temperature or chemical conditions, represents a potentially dangerous reaction, explosion or release of hazardous gas, steam, dust or fog.

Pressurized : Other solid, liquid or gaseous substance or mixes having fire or hazardous material response, when under pressure, and thus may represent a risk of uncontrolled emissions

Further criteria for the classification of flammable, reactive and pressurized substances are set out in Annex 1 of the Guide to the Regulations "Flammable, reactive and pressurized substances"

<http://www.dsb.no/Global/Publikasjoner/2009/Veiledning/Generell%20veiledning.pdf>

http://www.dsb.no/Global/Publikasjoner/2010/Tema/Temaveiledning_bruk_av_farlig_stoff_Del_1.pdf

Experiment setup area should be reviewed with respect to the assessment of Ex zone

- Zone 0: Always explosive atmosphere, such as inside the tank with gas, flammable liquid.
- Zone 1: Primary zone, sometimes explosive atmosphere such as a complete drain point
- Zone 2: secondary discharge could cause an explosive atmosphere by accident, such as flanges, valves and connection points

7.4 Effects on the environment

With pollution means: bringing solids, liquid or gas to air, water or ground, noise and vibrations, influence of temperature that may cause damage or inconvenience effect to the environment.

Regulations: <http://www.lovddata.no/all/hl-19810313-006.html#6>

NTNU guidance to handling of waste: <http://www.ntnu.no/hms/retningslinjer/HMSR18B.pdf>

7.5 Radiation

Definition of radiation

Ionizing radiation: Electromagnetic radiation (in radiation issues with wavelength <100 nm) or rapid atomic particles (e.g. alpha and beta particles) with the ability to stream ionized atoms or molecules.

Non ionizing radiation: Electromagnetic radiation (wavelength >100 nm), og ultrasound₁ with small or no capability to ionize.

Radiation sources: All ionizing and powerful non-ionizing radiation sources.

Ionizing radiation sources: Sources giving ionizing radiation e.g. all types of radiation sources, x-ray, and electron microscopes.

Powerful non ionizing radiation sources: Sources giving powerful non ionizing radiation which can harm health and/or environment, e.g. class 3B and 4. MR₂ systems, UVC₃ sources, powerful IR sources₄.

₁Ultrasound is an acoustic radiation ("sound") over the audible frequency range (> 20 kHz). In radiation protection regulations are referred to ultrasound with electromagnetic non-ionizing radiation.

₂MR (e.g. NMR) - nuclear magnetic resonance method that is used to "depict" inner structures of different materials.

₃UVC is electromagnetic radiation in the wavelength range 100-280 nm.

₄IR is electromagnetic radiation in the wavelength range 700 nm - 1 mm.

For each laser there should be an information binder (HMSRV3404B) which shall include:

- General information
- Name of the instrument manager, deputy, and local radiation protection coordinator
- Key data on the apparatus
- Instrument-specific documentation
- References to (or copies of) data sheets, radiation protection regulations, etc.
- Assessments of risk factors
- Instructions for users
- Instructions for practical use, startup, operation, shutdown, safety precautions, logging, locking, or use of radiation sensor, etc.
- Emergency procedures
- See NTNU for laser: <http://www.ntnu.no/hms/retningslinjer/HMSR34B.pdf>

7.6 The use and handling of chemicals.

In the meaning chemicals, a element that can pose a danger to employee safety and health

See: <http://www.lovddata.no/cgi-wift/ldles?doc=/sf/sf/sf-20010430-0443.html>

Safety datasheet is to be kept in the HSE binder for the experiment set up and registered in the database for chemicals.

Chapter 8 Assessment of operational procedures.

Ensures that established procedures meet all identified risk factors that must be taken care of through operational barriers and that the operators and technical performance have sufficient expertise.

8.1 Procedure Hazop

Procedural HAZOP is a systematic review of the current procedure, using the fixed HAZOP methodology and defined guidewords. The procedure is broken into individual operations (nodes) and analyzed using guidewords to identify possible nonconformity, confusion or sources of inadequate performance and failure.

8.2 Procedure for running experiments and emergency shutdown.

Have to be prepared for all experiment setups.

The operating procedure has to describe stepwise preparation, startup, during and ending conditions of an experiment. The procedure should describe the assumptions and conditions for starting, operating parameters with the deviation allowed before aborting the experiment and the condition of the rig to be abandoned.

Emergency procedure describes how an emergency shutdown have to be done, (conducted by the uninitiated),

what happens when emergency shutdown, is activated. (electricity / gas supply) and which events will activate the emergency shutdown (fire, leakage).

Chapter 9 Quantifying of RISK

Quantifying of the residue hazards, Risk matrix

To illustrate the overall risk, compared to the risk assessment, each activity is plotted with values for the probability and consequence into the matrix. Use task IDnr.

Example: If activity IDnr. 1 has been given a probability 3 and D for consequence the risk value become D3, red. This is done for all activities giving them risk values.

In the matrix are different degrees of risk highlighted in red, yellow or green. When an activity ends up on a red risk (= unacceptable risk), risk reducing action has to be taken

CONSEQUENCES	Catastrophic	E1	E2	E3	E4	E5
	Major	D1	D2	D3	D4	D5
	Moderate	C1	C2	C3	C4	C5
	Minor	B1	B2	B3	B4	B5
	Insignificant	A1	A2	A3	A4	A5
		Rare	Unlikely	Possible	Likely	Almost
		PROBABILITY				

Table 8. Risk's Matrix

Table 9. The principle of the acceptance criterion. Explanation of the colors used in the matrix

COLOUR	DESCRIPTION
Red	Unacceptable risk Action has to be taken to reduce risk
Yellow	Assessment area. Actions has to be considered
Green	Acceptable risk. Action can be taken based on other criteria

Attachment to Risk Assessment report

Francis turbine

Project name	PIV measurement in the vaneless space of Francis turbine
Apparatus	Double-Cavity High speed laser, 2*10Mj, 1000Hz, 527nm
Unit	EPT
Equipment manager	Bård Brandåstrø
Project leader	Pål Tore Storli
HSE coordinator	Morten Grønli
HSE responsible (linjeleder)	Therese Løvås
Location	Waterpower Laboratory
Room number	11
Risk assessment performed by	Magne Tveit Bolstad

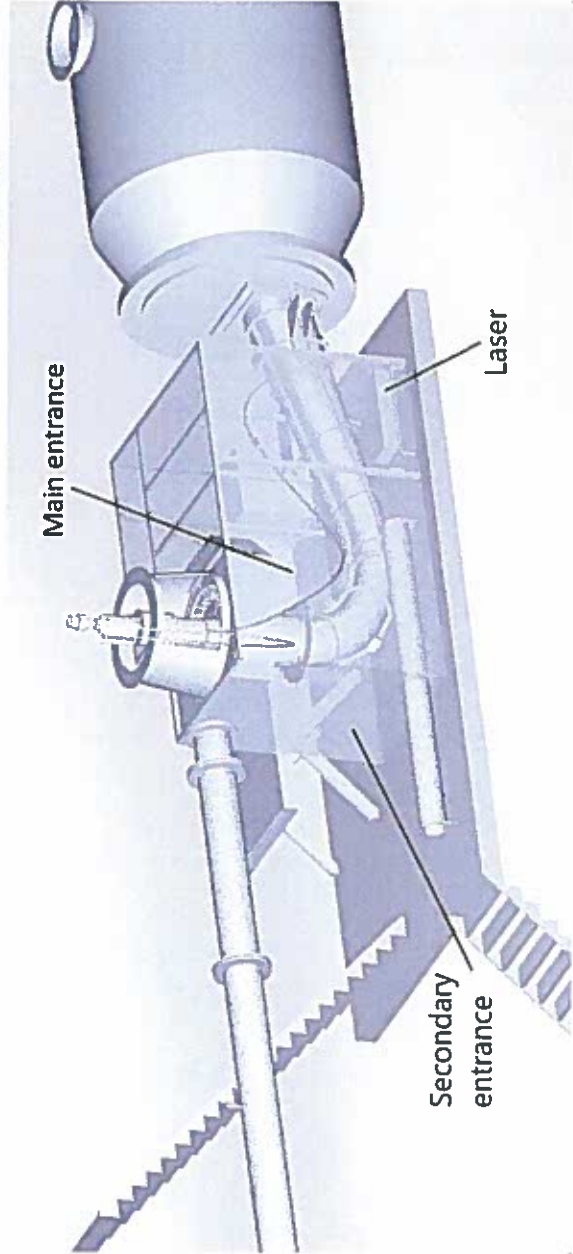
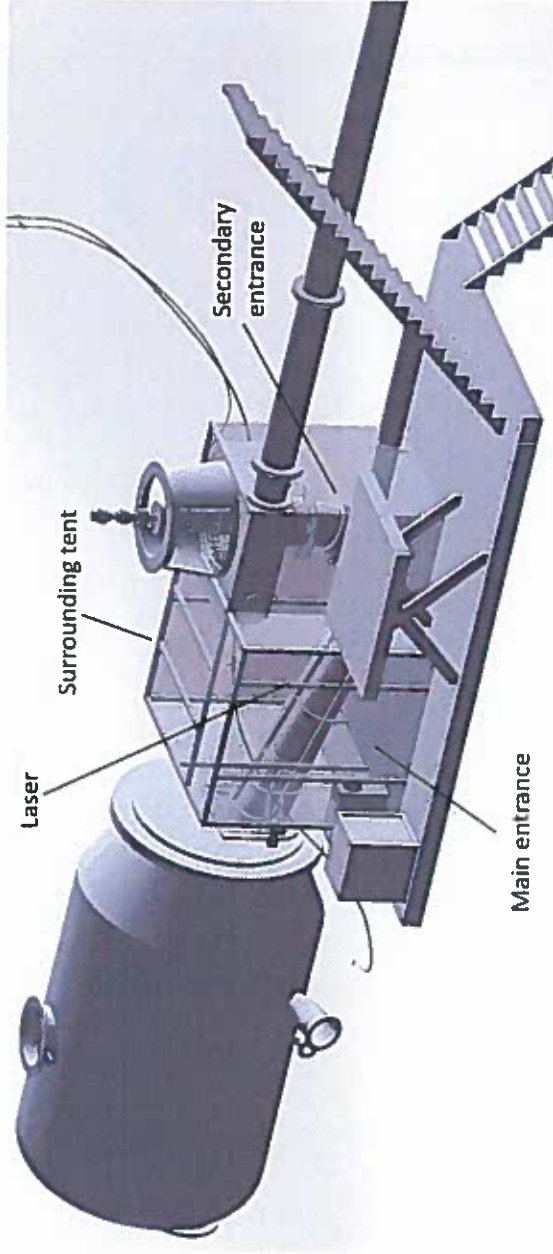
TABLE OF CONTENTS

- ATTACHMENT A: PROCESS AND INSTRUMENTATION DIAGRAM1
- ATTACHMENT B: HAZOP TEMPLATE2
- ATTACHMENT C: TEST CERTIFICATE FOR LOCAL PRESSURE TESTING3
- ATTACHMENT D: HAZOP PROCEDURE (TEMPLATE)4
- ATTACHMENT E: PROCEDURE OF RUNNING EXPERIMENTS5
- ATTACHMENT F: TRAINING OF OPERATORS7
- ATTACHMENT G: FORM FOR SAFE JOB ANALYSIS8
- APPARATURKORT / UNITCARD10
- FORSØK PÅGÅR / EXPERIMENT IN PROGRESS11

ATTACHMENT A: PROCESS AND INSTRUMENTATION DIAGRAM

Radiation area is blocked on all sides by light-blocking fabric (this includes a roof), working as a sealed tent. The entrance is overlapping fabric.

A warning light by the entrance will activate when the laser is on.



ATTACHMENT B: HAZOP TEMPLATE

Project: Node: Laser		Page					
Ref	Guideword	Causes	Consequences	Safeguards	Recommendations	Action	Date/Sign
	Unintentional rarefaction of beam	Poor alignment of laser beam, unintentional beam obstruction	Damage to personnel, damage to equipment	Laser emitter latched in place, radiation area enclosed	Careful instrument handling		
	Laser generation unit temperature rise	Cooling system failure	Equipment will overheat and break	-	Be aware of equipment condition		
	Unprotected personnel entering radiation area	Insufficient signalling, radiation area too accessible	Possibility of severe damage to personnel	Signalling and warning light in place, radiation area enclosed with physical obstruction	Always run experiments with warning light on		
	Electrical failures in apparatuses	Wear, poor construction	Equipment failure				
	Fire hazard	Laser beam hitting flammable material	Fire	Enclosing fabric approved for shielding laser experiments.	Make sure a fire extinguisher is easily available		
	Beam interception by operator	Careless equipment handling, obstructed work area	Damage to personnel, severe if lacking protective gear	Goggles approved for laser in use worn by operator	Careful instrument handling		

ATTACHMENT C: TEST CERTIFICATE FOR LOCAL PRESSURE TESTING

Trykkpåkjent utstyr:	Rør
Benyttes i rigg:	
Design trykk for utstyr (bara):	10bar
Maksimum tillatt trykk (bara): (i.e. burst pressure om kjent)	10bar
Maksimum driftstrykk i denne rigg:	10bar

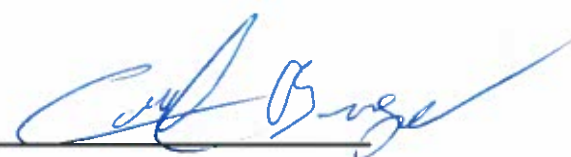
Prøvetrykket skal fastlegges i følge standarden og med hensyn til maksimum tillatt trykk.

Prøvetrykk (bara):	10bar		
X maksimum driftstrykk: I følge standard			
Test medium:	Vann		
Temperatur (°C)			
Start tid:	Fall 2016	Trykk (bara):	
Slutt tid:	Fall 2016	Trykk (bara):	
Maksimum driftstrykk i denne rigg:			

Eventuelle repetisjoner fra atm. trykk til maksimum prøvetrykk:.....

Test trykket, dato for testing og maksimum tillatt driftstrykk skal markers på (skilt eller innslått)


Trondheim 29.05.2017
Sted og dato


Signatur

ATTACHMENT D: HAZOP PROCEDURE (TEMPLATE)

Project: Node: 1							Page
Ref#	Guideword	Causes	Consequences	Safeguards	Recommendations	Action	Date/Sign
	Not clear procedure	Procedure is to ambitious, or confusingly					
	Step in the wrong place	The procedure can lead to actions done in the wrong pattern or sequence					
	Wrong actions	Procedure improperly specified					
	Incorrect information	Information provided in advance of the specified action is wrong					
	Step missing	Missing step, or step requires too much of operator					
	Step unsuccessful	Step has a high probability of failure					
	Influence and effects from other	Procedure's performance can be affected by other sources					

ATTACHMENT E: PROCEDURE FOR RUNNING EXPERIMENTS

PIV measurements in the vaneless space of a Francis turbine	Dato	Signatur
Apparatur Double-Cavity High speed laser, 2*10mJ, 1000Hz, 527nm		
Prosjektleder Pål Tore Storli	7/2-19	

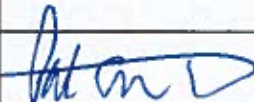
Conditions for the experiment:	Completed
Experiments should be run in normal working hours, 08:00-16:00 during winter time and 08.00-15.00 during summer time. Experiments outside normal working hours shall be approved.	
One person must always be present while running experiments, and should be approved as an experimental leader.	
An early warning is given according to the lab rules, and accepted by authorized personnel.	
Be sure that everyone taking part of the experiment is wearing the necessary protecting equipment and is aware of the shut down procedure and escape routes.	
Preparations	Carried out
1. Make sure the tent is closed.	
2. Post the "Experiment in progress" sign.	
3. Rotate emergency button so that it clicks in the out position.	
4. Turn the system key to "on".	
5. Turn the pump on in either internal or external mode.	
6. Turn on the warning light to open this laser interlock.	
7. Put on laser goggles.	
8. Block the entrance to the experimental area using warning chains.	
9. Turn the laser on in either internal or external mode.	
10. Open the shutter when ready to operate safely.	
During the experiment	
<i>Keep unauthorized personnel out of radiation area</i>	
<i>Avoid wearing jewellery and/or shiny objects</i>	
End of experiment	
<i>Close the shutter.</i>	

Turn the LASER OFF.	
Turn the warning light off.	
Allow the pump to run for approximately 2 minutes to avoid excess heat to damage the equipment.	
Turn the pump off	
Turn the system off	
Press the emergency button	
To reflect on before the next experiment and experience useful for others	
Was the experiment completed as planned and on scheduled in professional terms?	
Was the competence which was needed for security and completion of the experiment available to you?	
Do you have any information/ knowledge from the experiment that you should document and share with fellow colleagues?	

Operator(s):

Name	Date	Signature
Magne Tveit Bolstad	21.08.17	<i>Magne Tveit Bolstad</i>
Kristian Sagmo	21.08.17	<i>Kristian Sagmo</i>
Anja Mærleie	05.02.19	<i>Anja Mærleie</i>



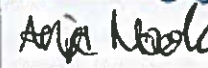
ATTACHMENT F: TRAINING OF OPERATORS

Project	Date	Signature
PIV measurements in the vaneless space of a Francis turbine		
Apparatus Double-Cavity High speed laser, 2*10mJ, 1000Hz, 527nm		
Project Leader Pål Tore Storli	7/2-19	

Knowledge about EPT LAB in general	
Lab	
<ul style="list-style-type: none"> • Access • routines and rules • working hour 	
Knowledge about the evacuation procedures.	
Activity calendar for the Lab	
Early warning, lept-experiments@ivt.ntnu.no	
Knowledge about the experiments	
Procedures for the experiments	
Emergency shutdown.	
Nearest fire and first aid station.	

I hereby declare that I have read and understood the regulatory requirements has received appropriate training to run this experiment and are aware of my personal responsibility by working in EPT laboratories.

Operator(s):

Name	Date	Signature
Magne Tveit Bolstad	21.08.17	
Kristian Sagmo	21.08.17	
Anja Mærleie	05.02.19	

ATTACHMENT G: FORM FOR SAFE JOB ANALYSIS

SJA name:	
Date:	Location:
Mark for completed checklist:	

Participators:		
SJA-responsible:		

Specification of work (What and how?):
Risks associated with the work:
Safeguards: (plan for actions, see next page):
Conclusions/comments:

Recommended/approved	Date/Signature:	Recommended/approved	Date/Signature:
SJA-responsible:		HSE responsible:	
Responsible for work:		Other, (position):	

HSE aspect	Yes	No	NA	Comments / actions	Resp.
Documentation, experience, qualifications					
Known operation or work?	X				
Knowledge of experiences / incidents from similar operations?		X			
Necessary personnel?	X				
Communication and coordinating					
Potential conflicts with other operations?		X			
Handling of an eventually incident (alarm, evacuation)?		X			
Need for extra assistance / watch?		X			
Working area					
Unusual working position		X			
Work in tanks, manhole?		X			
Work in ditch, shaft or pit?		X			
Clean and tidy?	X				
Protective equipment beyond the personal?		X			
Weather, wind, visibility, lighting, ventilation?	X				
Usage of scaffolding/lifts/belts/ straps, anti-falling device?		X			
Work at heights?		X			
Ionizing radiation?		X			
Influence of escape routes?		X			
Chemical hazards					
Usage of hazardous/toxic/corrosive chemicals?		X			
Usage of flammable or explosive chemicals?		X			
Risk assessment of usage?	X				
Biological materials/substances?		X			
Dust/asbestos/dust from insulation?		X			
Mechanical hazards					
Stability/strength/tension?		X			
Crush/clamp/cut/hit?		X			
Dust/pressure/temperature?		X			
Handling of waste disposal?		X			
Need of special tools?		X			
Electrical hazards					
Current/Voltage/over 1000V?		X			
Current surge, short circuit?		X			
Loss of current supply?		X			
Area					
Need for inspection?	X				
Marking/system of signs/rope off?	X				
Environmental consequences?		X			
Key physical security systems					
Work on or demounting of safety systems?		X			
Other					

APPARATURKORT

Enhet (unit) og bygg/romnr. (building/room no.):

NTNU-E 324

11

1. etg

Laboratorium

Dette kortet SKAL henges godt synlig ved maskinen!
This card MUST be posted on a visible place on the unit!

Apparatur (Unit) Double-Cavity High speed laser, 2*10mJ, 10	Dato Godkjent (Date Approved) torsdag 7. februar 2019
Prosjektleder (Project Leader) Pål Tore Selbo Storli	Telefon mobil/privat (Phone no. mobile/private) 97782146
Apparaturansvarlig (Unit Responsible) Bård Aslak Brandåstrø	Telefon mobil/privat (Phone no. mobile/private) 91897257
Sikkerhetsrisikoer (Safety hazards) Use of PIV laser (class IV). Related hazards: Ocular damage (cataract and retinal burn) and/or skin burn.	
Sikkerhetsregler (Safety rules) - Wear appropriate safety goggles for laser wavelength - No shiny objects (eg. Jewellery) worn	
Nødstopprosedyre (Emergency shutdown) Press the red "EMERGENCY STOP" button on the laser power supply	
Her finner du (Here you will find): Prosedyrer (Procedures) Bruksanvisning (User manual)	Apparaturperm ved laser Apparaturperm ved laser
Brannslukningsapparat (Fire extinguisher) Førsthjelpsskap (First aid cabinet)	1. etasje lab (syd) 1. etasje lab (syd)

NTNU

Institutt for energi og prosessteknikk

Dato

7/2-2019

Signert

 NTNU

 SINTEF

FORSØK PÅGÅR

Enhet (unit) og bygg/romnr. (building/room no.):

NTNU-E 324

11

1. etg

Laboratorium

Dette kortet SKAL henges opp før forsøk kan starte!

This card MUST be posted on the unit before the experiment startup!

Apparatur (Unit) Double-Cavity High speed laser, 2*10mJ, 1000Hz. 527nm	Dato godkjent (Date Approved) torsdag 7. februar 2019
Prosjektleder (Project Leader) Pål Tore Selbo Storli	Telefon mobil/privat (Phone no. mobile/private) 97782146
Apparaturansvarlig (Unit Responsible) Bård Aslak Brandåstrø	Telefon mobil/privat (Phone no. mobile/private) 91897257
Godkjente operatører (Approved Operators)	
Navn/Name	Telefon/Phone Mobil
Sagmo, Kristian	452 44 270
Bolstad, Magne Tveit	
Mærlie, Anja	
Prosjekt (Project) PIV measurements on blade cascade for HiFrancis project	
Forsøkestid / Experimental time (start - stop) 07.02.2019 - 07.02.2020	
Kort beskrivelse av forsøket og relaterte farer (Short description of the experiment and related hazards) Laser measurements with class IV laser on a blade cascade test section. Danger of eye injury and skin injury. Radiation area clearly marked. The flashing laser light can in some cases trigger epilepsy if proper goggles are not worn.	

NTNU

Institutt for energi og prosessteknikk

Dato

7/2 - 2019

Signert

NTNU

SINTEF